Final Draft
of the original manuscript:

Winzer, N.; Atrens, A.; Dietzel, W.; Song, G.; Kainer, K.U.:

Fractography of Stress Corrosion Cracking of Mg-Al Alloys

In: Metallurgical and Materials Transactions A (2008) TMS

DOI: 10.1007/s11661-008-9475-8

The Fractography of Stress Corrosion Cracking (SCC) of Mg-Al Alloys

N. Winzer[a], A. Atrens[a,c], W. Dietzel[b], G. Song[a], K.U. Kainer[b]

[a] Materials Engineering, The University of Queensland, Brisbane 4072, Australia
Email: n.winzer@minmet.uq.edu.au
Phone: +61 (0)7 3365 4183
[b] Institute for Materials Research, GKSS-Forschungszentrum Geesthacht GmbH, D-21502, Geesthacht, Germany
[c] Swiss Federal Laboratories for Materials Science and Technology, EMPA, Dept 136, Überlandstrasse 129, CH-8600 Dubendorf, Switzerland

Abstract

The mechanisms for SCC of Mg-Al alloys have been investigated by scanning electron microscopy of the fracture surfaces for the binary alloy AZ91 and for the single-phase alloys AZ31 and AM30 in distilled water. The mechanism for crack initiation in AZ31 and AM30 involves localised dissolution. The mechanisms for crack propagation in AZ31 and AM30 involve microvoid coalescence and cleavage respectively. The mechanism for crack initiation in AZ91 is uncertain, but may involve fracture of β-particles near the surface. The mechanism for crack propagation at moderate strain rates in AZ91 is similar to that in AZ31, with β-particles acting as sources of H for mobile dislocations. The fracture surface for AZ91 tested at the strain rate 3×10^{-8} s^{-1} was similar to that for specimens pre-charged in gaseous H_2. This fracture surface is the result of: (i) nucleation and growth of MgH_2 particles; (ii) sudden fracture through the MgH_2 particles at some critical stress; and (iii) decomposition of the MgH_2 particles after fracture.

Keywords: fractography, stress corrosion cracking, hydrogen embrittlement, magnesium alloys

1 Introduction

Our review [1] of Stress Corrosion Cracking (SCC) of Mg alloys showed that there exists a considerable amount of research outlining the phenomenology of Transgranular Stress Corrosion Cracking (TGSCC) of Mg alloys. TGSCC is the inherent mode of SCC of Mg alloys [1]. It is generally accepted that the mechanism for TGSCC of Mg alloys is a form of Hydrogen Embrittlement (HE); however, the specific nature of the HE mechanism remains equivocal. The HE models that may be applicable for Mg alloys are: Hydrogen Enhanced Decohesion (HEDE); Hydrogen Enhanced Localised Plasticity (HELP); Adsorption Induced Dislocation Emission (AIDE); and Delayed Hydride Cracking (DHC). AIDE [2] and DHC [3, 4, 5, 6] have been proposed for TGSCC of Mg alloys; however, the evidence for both mechanisms is limited. HEDE and HELP also remain possible mechanisms. Detailed reviews of these mechanisms are provided in Birnbaum [7], Lynch [8] and Gangloff [9]. A brief review of these mechanisms with respect to experimentally measurable characteristics of SCC in Mg alloys is given in Winzer et al [10]. Fractographic aspects of these mechanisms are reviewed below.

1.1 The Fractography of HE

HEDE involves reduction of the electron charge density between metal atoms in the region ahead of the crack tip, where H accumulates by stress-assisted diffusion. This causes weakening of the bonds between and eventually tensile separation of adjacent metal atoms. Fracture may be intergranular or transgranular. In the case of transgranular HEDE, fracture is expected to occur by cleavage resulting in river markings (as per conventional cleavage) [7, 8, 9].

DHC involves repeated stages of: (i) stress-assisted diffusion of H to the region ahead of the crack tip; (ii) hydride precipitation as the local H concentration exceeds the local solvus; and (iii) brittle fracture through the hydride. Previous proposals for DHC in Mg alloys [3, 4, 5, 6] have been based primarily on fractographic evidence. Bursle and Pugh [5] observed a crazed layer, interpreted as being MgH_2, on the fracture surface of Mg-7.5Al specimens tested in a NaCl + K_2CrO_4 solution. For the same alloy and environment, Chakrapani and Pugh [4] correlated fine parallel markings within cleavage facets, believed to be indicative of crack arrest at the hydride-matrix boundary, with acoustic signals, believed to be energy released by crack advance through the hydride. Meletis and Hochman [3] suggested that the cleavage plane for pure Mg in NaCl + K_2CrO_4 solution may be the habit plane for MgH_2 (hydrides in group 4 metals occupy a habit plane close to (0001) [11]).

Previous workers [12, 13, 14, 15, 16] have investigated the morphology of DHC in Zr alloys, particularly Zr-2.5%Nb. DHC models [17, 18, 19, 20] are generally based on the formation of a single hydride platelet oriented parallel to the crack plane, as observed by Shek et al [15] for a Zr-Nb alloy. However, since hydride orientation is dependent on stress distribution [11], the single hydride platelet model may be overly simplistic for inhomogeneous service alloys in which the stress distribution may be highly irregular. Fracture surfaces for DHC are characterised by regions of cleavage-like markings separated by relatively narrow dimpled striations, with the striations perpendicular to the crack direction. These features are associated with alternating stages of crack advance, which is continuous along the entire length of the hydride platelet, followed by crack tip blunting and arrest in the ductile matrix. Nuttall and Rogowski [14] and Simpson [16] observed shear cliffs and ridges that were attributed to ductile failure of metal ligaments between adjacent hydride platelets, with the number of cliffs and ridges increasing with the applied stress intensity factor. Cox [12] reported that the edges of cleavage facets were stepped, rather than cusped as per non-DHC environments. This contrast was attributed to the difference in crystal structure (tetragonal rather than hexagonal) of the hydride relative to α-Zr.

Winzer et al [21] proposed that hydride precipitation in Mg alloys is accompanied by plastic deformation due to the volumetric misfit between the hydride and the substituted metal matrix. However, it is unclear how the plastic deformation affects the fracture surface morphology.

The fractography for HELP and AIDE may be similar since both mechanisms involve microvoid nucleation. HELP is attributed to the decrease in resistance to dislocation motion and increase in dislocation velocity due to the interaction between H atmospheres at mobile dislocations with stress fields and H atmospheres at microstructural features [7, 8, 9]. Since HELP is associated with dislocation emission from the plastic zone ahead of the crack tip, the resulting fracture surfaces are characteristically ductile. In contrast, AIDE is attributed to dislocation emission due to weakening of metal-metal bonds by H atoms adsorbed at the crack tip and trapped within the first few atomic layers of metal [8, 22]. Since dislocations are emitted from the crack tip during AIDE, rather than from the plastic zone (as per HELP), crack growth occurs by alternating slip on specific planes. The resulting fracture surfaces consist of low-index cleavage-like facets containing small, shallow dimples.

Lynch [8] suggested that HELP, HEDE and AIDE can occur simultaneously, resulting in unique fracture surface morphologies. These HE mechanisms are associated with different stress corrosion crack velocities [7, 8, 9]. Thus, the coincidence of two HE mechanisms would occur only at specific stress corrosion crack velocities.

1.2 Scope of Present Research

Our review [1] identified a need for a mechanistic understanding of the influences of environment, microstructure and mechanical loading on SCC of Mg alloys to support the growing use of Mg alloys for stressed components in service such as for automotive applications. The present research focuses on developing this mechanistic understanding by evaluating the SCC behaviour of three Mg-Al alloys with contrasting microstructures: (i) AZ91, which consists of an α-matrix with extensive β-particles; (ii) AZ31, which consists of an α-matrix with Al-concentration similar to the AZ91 α-matrix; and (iii) AM30, which consists of an α-matrix with similar composition to AZ31, but with lower Zn-concentration. The alloys were tested under Constant Extension Rate Test (CERT) and Linearly Increasing Stress Test (LIST) conditions in distilled water and after pre-charging in H_2 gas.

In our previous publication [10], new mechanisms were identified for SCC initiation in AZ31, AM30 and AZ91 and SCC propagation in AZ91. SCC initiation in AZ31 and AM30 involves localised dissolution, whereas SCC initiation in AZ91 involves H-assisted fracture of β-particles close to the surface, with H ingress facilitated by mechanical rupture of the surface film. SCC propagation in AZ91 involves crack nucleation within β-particles ahead of the primary crack tip. It was also shown that the stress corrosion crack velocity for AM30 is much slower than for AZ91 and AZ31, indicating different crack propagation mechanisms. These results provided new insights into the influence of alloying and microstructure on the SCC characteristics of Mg-Al alloys. This paper further evaluates the possible HE mechanisms by examining the SCC fracture surfaces for these three alloys.

2 Experimental Method

The test materials were the Mg alloys AZ91, AZ31 and AM30. AZ91 specimens were machined from as-cast ingots, whereas AZ31 and AM30 specimens were machined from large extrusions such that their tensile axis was parallel with the extrusion direction. The microstructure of AZ91 consisted of an α matrix with an extensive Mg-Al-Zn interdentritic phase (β-particles), fine Mg-Al-Mn plate-like crystals within the β-particles and small Al-Mn intragranular precipitates. AZ31 and AM30 microstructures were relatively homogeneous and consisted of an α matrix with small Al-Mn quadrilateral crystals (which were larger and more numerous for AZ31), small Mg-Si particles and elongated Al-Mn plate-like crystals that were aligned collinearly in the extrusion direction. The alloys were machined into cylindrical tensile specimens with a 5 mm diameter waisted gauge section. The gauge surfaces were polished with 1,200-grade emery paper and cleaned using ethanol immediately before testing.

The specimens were tested under linearly increasing stress test (LIST) [23] or constant extension rate test (CERT) conditions in double-distilled H_2O or after pre-charging in gaseous H_2 at 30 bar and 300 °C for 15 h, with control tests carried out in laboratory air. SCC initiation was detected using the DC potential drop (DCPD) method as per Dietzel et al [24] and Atrens et al [23, 25, 26, 27, 28]. The fracture surfaces were cleaned using ethanol immediately following cessation of the test, and in 180 g/L chromic acid immediately before SEM examination.

3 SCC Characteristics

The SCC characteristics of AZ91, AZ31 and AM30 in distilled water under LIST and CERT conditions are discussed with respect to the possible mechanisms in Winzer et al [10]. It is sufficient to show here the engineering stress versus apparent strain curves for the alloys under CERT conditions in distilled water and laboratory air (Figures 1 – 3). The apparent plastic deformation in these curves is largely attributed to stress corrosion cracking. For all alloys in distilled water, there was a decrease in SCC susceptibility with increasing strain rate. The decreasing SCC susceptibility was characterised by: (i) an increasing difference between σ_{SCC} and the UTS; (ii) an increasing apparent ductility; (iii) an increasing σ_{SCC} (for AZ91 and AZ31 only); and (iv) an increased stress corrosion crack velocity (for AZ91 only).

Figure 1 - Stress versus apparent strain curves for AZ91 in distilled water and air under CERT conditions [10].

Figure 2 - Stress versus apparent strain curves for AZ31 in distilled water and air under CERT conditions [10].

Figure 3 - Stress versus apparent strain curves for AM30 in distilled water and air under CERT conditions [10].

4 Fracture Surface Morphology

4.1 Fracture in Air

The fracture surfaces for AZ91, AZ31 and AM30 in laboratory air are shown in Figures 4 to 6. The fracture surface for AZ91 in laboratory air consisted of broken, jagged features interspersed with small dimpled regions (Figure 4). The fracture surfaces for AZ31 and AM30 in laboratory air consisted of coarse, irregular dimple-like features (Figures 5 and 6). The contrast between these fracture surfaces and those for AZ91, AZ31 and AM30 in distilled water (see below) indicates that laboratory air does not promote SCC.

Figure 4 – Fracture surface for AZ91 specimen tested in laboratory air, with arrows indicating broken, jagged features (i) and dimpled regions (ii).

Figure 5 – Fracture surface for AZ31 specimen tested in laboratory air.

Figure 6 – Fracture surface for AM30 specimen tested in laboratory air.

4.2 SCC of AZ91

The fracture surface morphology for AZ91 in distilled water was presented in Winzer et al [29]. The fracture surfaces typically contained multiple thumbnail-shaped SCC zones with the remaining fracture surface comprised of broken, jagged features consistent with fracture in laboratory air. The SCC zones were generally characterised by: (i) parallel facets ~5 μm wide (the 'vertical' features indicated in Figure 7B); (ii) jogging at the edges of each facet (Figure 7D); (iii) extensive crack branching; and (iv) cleavage through β-particles (Figures 8 – 9). Examination at high magnification revealed that the parallel facets contained fine parallel markings (<0.5 μm apart) or ellipsoidal micro-dimples (Figures 8 – 9); however, the morphology of these features was difficult to determine using SEM. The orientation of the parallel facets and fine parallel markings was influenced by β-particles (Figures 8 – 9). The fracture surfaces also contained pyramidal crevices (Figure 10) that have since been observed on fatigue fracture surfaces for AZ91 compact tensile specimens [30] and are consequently attributed to an inert fracture process.

Figure 7 – Fracture surface for AZ91 specimen tested in distilled water under CERT conditions showing jogging (Detail A) and parallel markings (indicated in Detail B) [29].

Figure 8 – Fracture surface for AZ91 specimen tested in distilled water under CERT conditions showing fine parallel markings (i) and cleavage through β particles [29].

Figure 9 – Fracture surface for AZ91 specimen tested in distilled water under CERT conditions showing the influence of β precipitates on the direction of parallel markings (i) [29].

Figure 10 – SEM micrographs of AZ91 specimen fractured in distilled water under CERT conditions showing pyramidal crevices [29].

In Winzer et al [29], the fracture surface morphology for SCC initiation in AZ91 under CERT conditions was evaluated by removing specimens from the environment at stresses slightly greater than σ_{SCC}. The fracture surfaces were generally consistent with those produced by fracture in air, but also contained small (<100 μm across) rounded regions adjacent to the gauge surface, were attributed to SCC. The SCC initiation zones consisted of fine parallel markings or micro-dimples (Figure 11), similar to those observed within parallel facets for ongoing crack propagation under CERT conditions (Figures 8 – 9). This indicating similar mechanisms for SCC initiation and propagation.

Figure 11 – Morphology of SCC initiation for AZ91 in distilled water under CERT conditions showing fine parallel markings or elongated dimples.

Our previous publication [10] evaluated the morphology of secondary cracks in AZ91 specimens tested in distilled water under CERT conditions using optical micrography. The secondary cracks were nucleated within β-particles ahead of the principle crack tip (Figure 12D) and propagated transgranularly, with perpendicular cliffs forming between converging consecutive cracks (Figure 12B). The formation of perpendicular cliffs between consecutive cracks may have contributed to the faceted appearance of the fracture surface. Undercutting of the cliffs by converging cracks may have contributed to the appearance of crack branches on the fracture surface.

Figure 12 – Optical microscopy of secondary crack for AZ91 in distilled water under CERT conditions, with arrows indicating undercutting (i) and β-particles (ii) [10].

4.3 SCC of AZ91 at the Very Slow Strain Rate

The fracture surface morphology for AZ91 specimens tested in distilled water under CERT conditions at the slowest strain rate ($3x10^{-8}$ s^{-1}) contained features in stark contrast with those for AZ91 specimens tested at faster strain rates. The fracture surface consisted of multiple thumbnail-shaped SCC zones (Figure 13A) characterised by parallel facets, jogging and secondary cracking as per AZ91 specimens tested in distilled water at higher strain rates. The remaining fracture surface consisted of smooth, rounded features (somewhat comparable to casting porosity) interspersed with small (< 50 μm across) regions comprised of broken, jagged facets consistent with fracture in laboratory air (Figure 13C). Whilst there is a similarity to casting porosity, this fracture morphology was attributed to a HE mechanism (see Section 4.6).

Figure 13 – Quasi-porous fracture surface for AZ91 specimen fractured in distilled water at $3x10^{-8}$ s^{-1}, with arrows indicating smooth, rounded features (i) and regions containing broken, jagged features (ii).

4.4 SCC of AZ31 and AM30

The fracture surfaces for AZ31 and AM30 specimens tested in distilled water consisted of three separate morphologies: (i) a 100 to 200 μm wide region at the gauge surface consistent with severe localised dissolution (probably strain assisted); (ii) a SCC zone; and (iii) a final overload fracture region consistent with fracture in an inert environment (Figure 14). The width and morphology of the localised dissolution regions corresponded with the depth and morphology of secondary cracks in AZ31 and AM30 specimens tested in distilled water under CERT conditions, as shown in Figure 15 [10].

Figure 14 – Fracture surface for AM30 in distilled water under CERT conditions showing zones corresponding to localised dissolution, SCC and inert fracture. Fracture surfaces for AZ31 in distilled water were similarly composed.

Figure 15 – Optical microscopy of secondary crack for AZ31 in distilled water under CERT conditions [10].

The SCC zone for AZ31 consisted of discrete, macroscopically flat regions on multiple parallel planes (Figure 16A). The macroscopically flat regions were joined by cliffs containing features consistent with the inert fracture mode. Examination of the macroscopically flat regions at higher magnification revealed quasi-crystallographic markings containing small (<0.5 μm across) specifically oriented ellipsoidal dimples, which were sometimes only visible by tilting the fracture surface by 45° (Figures 16D and 16G). The dimples were similar to those observed within parallel facets (Figure 8), and within regions corresponding to SCC initiation (Figure 11), for AZ91 in distilled water. The SCC zone also contained some features that were consistent with the inert fracture mode. The proportion of the SCC zone corresponding to the inert fracture mode increased with increasing strain rate. The final-fracture region consisted of coarse, irregular dimples consistent with the fracture surface topography for laboratory air.

Figure 16 – Fracture surface for AZ31 specimen tested in distilled water under CERT conditions, with arrows indicating macroscopically flat regions on parallel planes.

The SCC zone for AM30 consisted of macroscopically flat regions on multiple parallel planes (Figure 17A). On each plane there was a narrow band of uniform width (Figure 17B) containing cleavage-like markings (Figures 17E and 17G). These SCC regions extended along the entire circumference of the fracture surface. The cleavage facets contained coarse, pit-like features and tunnels (attributed to highly localised corrosion on the crack surface) that diminished in size and density with increasing distance from the gauge surface (Figure 17D). The SCC zone also contained some dimple-like features consistent with the inert fracture mode that increased in density with increasing strain rate (Figures 17C and 17F). The final-fracture region consisted of highly irregular dimple-like markings similar to those observed for fracture in air.

Figure 17 – Fracture surface for AM30 specimen tested in distilled water under CERT conditions, with arrow indicating macroscopically flat regions on parallel planes (i) and tunnelling due to localised corrosion on the crack surface (ii).

4.5 LIST versus CERT Fractography

Winzer et al [29] compared the fracture surfaces for AZ91 in distilled water under LIST and CERT conditions. Under LIST conditions, complete fracture ensues shortly after σ_{SCC} is reached, resulting in a small SCC zone relative to that formed under CERT conditions. In the present study, the fracture surfaces for AZ31 and AM30 in distilled water under LIST and CERT conditions were compared. The morphologies of the SCC zones for AZ31 and AM30 under LIST conditions were consistent with those formed under CERT conditions: quasi-crystallographic markings containing ellipsoidal dimples for AZ31 (Figure 18) and cleavage-like markings for AM30 (Figure 19). As per AZ91 [29], the SCC zones formed under LIST conditions were smaller than those formed under CERT conditions. In addition, under LIST conditions there was no SCC initiation region for AZ31 and AM30 by localised (strain assisted) dissolution as there was under CERT conditions (Figure 14). This can only be due to subtle differences in mechanical loading under LIST conditions compared to those under CERT conditions.

Figure 18 – Early-stage fracture surface morphology for AZ31 specimen tested in distilled water under LIST conditions.

Figure 19 – Early-stage fracture surface morphology for AM30 specimen tested in distilled water under LIST conditions.

4.6 H_2 Gas Pre-charged AZ91

The fracture surfaces for AZ91 specimens pre-charged in H_2 gas at 300 °C and 30 bar for 15 h and then fractured rapidly in air were similar to those for AZ91 tested in distilled water at 3×10^{-8} s^{-1}. However, in the case of the H_2 gas pre-charged specimens, the quasi-porous morphology (Figure 20) was distributed across the entire fracture surface, with no part of the fracture surface corresponding to a SCC zone as was shown in Figure 13.

Figure 20 – Quasi-porous fracture surface for AZ91 pre-charged in H_2 gas at 30 bar and 300 °C.

The smooth, quasi-porous fracture surface morphology is difficult to reconcile with any existing HE mechanism. Moreover, because it occurs for AZ91 specimens pre-charged in H_2 gas, it cannot be due to any aqueous dissolution process. The quasi-porous features are somewhat similar to those associated with the evolution of H_2 gas bubbles during the solidification of castings. This indicates a mechanism involving separation and removal of a transient phase, with the separated phase having the form of a continuous network of smooth, rounded particles, such that quasi-porous voids remain after decomposition of the transient phase. Since H is present during gas pre-charging and testing in distilled water at 3×10^{-8} s^{-1}, and hydride formation ahead of the crack tip is possible for very low crack velocities (as proposed by Winzer et al [21]), then it seems likely that the mechanism involves: (i) nucleation and growth of MgH_2 particles as the H concentration exceeds the solvus concentration; (ii) fast fracture of the MgH_2 particles at some critical stress; and (iii) decomposition of the MgH_2 particles after removal of the external stress (Figure 21). Alternatively, fracture at the hydride/magnesium interface may occur; however, this seems less likely than fracture through the MgH_2 particles.

Figure 21 – Formation of the quasi-porous fracture surface for AZ91 pre-charged in H_2 gas at 300 ºC and 30Bar showing (A) nucleation and (B) growth of hydride particles in the bulk matrix, followed by (C) fracture and redissolution of the particles.

It should be noted that precipitation of MgH_2 is accompanied by significant plastic deformation in the surrounding matrix [21]. However, it is uncertain at this stage how this may contribute to the fracture surface morphology.

5 Hydride Formation in H_2-charged Specimens

The SCC mechanism for AZ91 specimens pre-charged in H_2 gas at 300 °C and 30 bar for 15 h and then fractured rapidly in air is intrinsically dependent on the H concentration imparted during the gas charging stage, and the change in solvus concentration due to cooling and stress application. These factors are evaluated below.

5.1 H_2-charging

The analysis assumes that under charging conditions the concentration of H dissolved in the specimen is at equilibrium with the charging medium (H_2 gas) and that the distribution of H in the specimen is uniform and equal to the concentration just inside the surface. Nishimura et al [31] showed that the solubility of H in pure Mg in the temperature range 200 – 220 °C and the pressure range 0.1 – 10 kPa obeys Sieverts' Law. Thus, assuming that the hydrogen pressure is equal to the hydrogen fugacity, and that under charging conditions H absorption is unimpaired by surface films or formation of a hydride layer, the equilibrium concentration in the specimen is:

$$C = K\sqrt{P} \qquad \text{Equation 1}$$

where P is pressure and K is the solubility constant. Nishimura et al [31] measured the solubility constant (in units of mol H_2 m^{-3} $Pa^{-1/2}$) to be:

$$K = 1.8 \times 10^{-1} \exp\left(\frac{-1.16 \times 10^4}{RT}\right) \qquad \text{Equation 2}$$

where R is the ideal gas constant and T is temperature in Kelvin. Equations 1 and 2 give C = 54.6 mol H/m^3 (or 7.6×10^{-2} at%) at 300 °C and 30 bar. This is consistent with H concentration measurements made using a LECO hydrogen analyser for AZ91 specimens charged at 300 °C and 30 bar for 15 h; however, the measured values (6.9×10^{-2} – 1.9×10^{-1} at%) exaggerated the actual H concentration in the bulk matrix by also measuring H contained in the corrosion products at the surface. The concentration predicted using Equations 1 and 2 is close to values given by previous workers [32, 33, 34, 35, 36, 37] for the solvus concentration ($6\text{x}10^{-2}$ – $7\text{x}10^{-2}$ at%) of H in pure Mg at ~1 bar in the temperature range 196 – 775 °C. Thus, it is possible that the solvus concentration is > $7.6\text{x}10^{-2}$ at% at 300 °C and 30 bar. In this case, the H concentration imparted by gaseous charging would be slightly less than the solvus concentration under charging conditions, such that MgH_2 is not precipitated during H_2 gas charging.

5.2 Cooling

After charging, the gas pressure was maintained whilst the specimen was cooled to room temperature. There is no empirical data for the solvus concentration, C_S, at ambient temperatures; however, an approximate value can be extrapolated from values measured at higher temperatures. Based on experimental data given by other workers, Zeng et al [38] modelled the Gibb's free energy of formation for MgH_2 in the temperature range 298 – 6000 K as:

$$\begin{aligned} G &= -108422.153 + 495.654655T - 75T\ln(T) \\ &-3.6920685\times10^{-16}T^2 + 5.93903667\times10^{-20}T^3 \qquad \text{Equation 3} \\ &-1.7334725\times10^{-8}T^{-1} \end{aligned}$$

which gives G = -97,341 J/mol at 573 K and G = -8,8047 J/mol at 298 K. G is related to the solvus concentration according to the equation [39]:

$$C_S = A\exp\left(\frac{G}{RT}\right) \qquad \text{Equation 4}$$

where A is some constant, which was calculated for C_S = $7\text{x}10^{-2}$ at% and T = 573 K. Equations 3 and 4 give C_S = $1.9\text{x}10^{-7}$ at% at T = 298 K. The validity of Equations 3 and 4 over this temperature range is uncertain; however, this analysis shows that C_S decreases by several orders of magnitude when the temperature is reduced from 573 K to 298 K. Thus, if C is only slightly lower than C_S after charging, and if H egress between charging and testing is minimal, MgH_2 is formed upon cooling of the specimen.

5.3 Stress Application

The solvus concentration would be further reduced during testing. C_S is influenced by hydrostatic stress, σ_{kk}, according to the equation [40, 41]:

$$C_S^{\sigma} = C_S\exp\left(\frac{\overline{W}_{\text{int}}}{2RT}\right)\exp\left(\frac{\sigma_{kk}\overline{V}_H}{RT}\right) \qquad \text{Equation 5}$$

where C_S is the solvus concentration in the absence of external stress, $\overline{W}_{\text{int}}$ is the interaction between the external stress field and strain resulting from the phase transformation and $\overline{V}_H$ is the partial molar volume of H in solid solution. $\overline{W}_{\text{int}}$ is furnished by [42]:

$$\overline{W}_{\text{int}} = -\frac{\sigma_{kk}}{3(1-b)}\left(V_{hr} - \left(\overline{V}_M + b\overline{V}_H\right)\right) \qquad \text{Equation 6}$$

where b is the ratio of hydrogen to metal atoms in solid solution, V_{hr} is the molar volume of the hydride and $\overline{V}_H$ is the partial molar volume of the metal in solid solution respectively. Using $b \approx 7.6\text{x}10^{-4}$ (from Equations 1 and 2), $\overline{V}_H$ = $7\text{x}10^{-7}$ m^3/mol (as per Zr [43]) and V_{hr} = $18.56\text{x}10^{-6}$ m^3/mol [44] and assuming $\sigma_{kk} = \sigma$, Equations 3 and 4 give

$C_S^{\sigma} = 0.95\ C_S$ at the measured UTS after gaseous H_2 charging (90 MPa) and $T = 298$ K. Thus, the reduction in C_S by the application of stress is small relative to the reduction in C_S due to cooling.

6 Discussion

6.1 LIST vs CERT Fractography

For AZ31 and AM30 specimens tested under LIST conditions, complete fracture occurred shortly after σ_{SCC} was reached, resulting in SCC zones that were smaller than those formed under CERT conditions. Mechanisms for HE in Mg alloys are generally dependent on strain rate, such that, as the strain rate increases, there is less time available for H ingress and embrittlement. Consequently, there exists some critical strain rate at which HE cannot occur and the inert fracture mode predominates. Under LIST conditions, the strain rate, $\delta\varepsilon/\delta t$, is inversely proportional to $\delta\varepsilon/\delta\sigma$. Consequently, specimens are subjected to very high strain rates during plastic deformation or SCC (when $\delta\varepsilon/\delta\sigma$ is relatively low), and there exists a critical crack length (corresponding to the critical strain rate for HE) at which there is a transition from SCC to the inert fracture mode. This is evidenced in the fractography by the narrow SCC zone formed under LIST conditions (Figures 18 and 19). The critical crack length, a_c, is related to the stress in the remaining cross section, σ□, and the fracture toughness of the metal in the absence of H, K_{IC}, by means of the fracture mechanics equation [45]:

$$K_{IC} = Y\sigma_n\sqrt{\pi a_c} \qquad \text{Equation 7}$$

where Y is a constant dependent on the crack geometry. Fast fracture occurs at a_c, which is defined by σ_n and K_{IC}.

6.2 The Influence of Strain Rate on Fracture Surface Morphology

For SCC of AZ91, AZ31 and AM30 in distilled water under CERT conditions there was a decrease in SCC susceptibility with increasing strain rate [10]. The decrease in SCC susceptibility was characterised by: (i) an increasing difference between σ_{SCC} and the UTS; (ii) an increasing apparent ductility; (iii) an increasing σ_{SCC} (for AZ91 and AZ31 only); and (iv) an increased stress corrosion crack velocity (for AZ91 only). In the fractography, the decrease in SCC susceptibility with increasing strain rate was characterised by the increase in the proportion of the SCC fracture surface corresponding to the inert fracture mode. In the case of AZ91, this is related to the increase in stress corrosion crack velocity with increasing strain rate. This implies that the measured stress corrosion crack velocity for AZ91 is dependent on the loading conditions. Moreover, the intrinsic corrosion crack velocity is relatively slow, and measured velocities higher than the intrinsic velocity are due to the contribution of the inert fracture mode.

6.3 Comparison of Fractography for AZ31 and AM30

The fracture surfaces for AZ31 and AM30 in distilled water under CERT conditions are indicative of stress corrosion crack propagation on multiple parallel planes, with cliffs forming between consecutive planes by inert fracture (Figures 16A and 17A). For both alloys, the mechanism for SCC initiation is severe localised dissolution (Figures 14 and 15), with a transition to the SCC propagation mechanism at some critical crack length [10]. This implies that there exists some critical stress or stress intensity factor for SCC propagation, below which SCC propagation cannot occur. The mechanism for SCC initiation in AZ31 and AM30 (severe localised dissolution) was different to that in AZ91, despite the similar compositions of AZ31 and AM30 and the α-phase of AZ91. Consequently, the different initiation mechanism for AZ91 is attributed to the presence of the β-phase, which is present in AZ91 due to its higher Al content.

Winzer et al [10] showed that the stress corrosion crack velocities for AM30 are much slower than those for AZ31. This is indicative of different crack propagation mechanisms. In most cases, the propensity for a particular mechanism is related to the quantity of H arriving at potential crack initiation sites, which is defined by the rate of H transport in the matrix, and the local H concentration required for fracture. This is not true for AIDE, for which H is only transported within the first few atomic layers ahead of the crack tip. Differences in the rates of H transport for AZ31 and AM30 may be related to the strength and distribution of H trap sites (particularly Al-Mn particles, which are larger and more numerous in AZ31) or the influence of Zn (contained in AZ31) on H diffusivity in the α matrix.

The comparison between the SCC fracture surfaces for AZ31 and AM30 specimens also indicates different crack propagation mechanisms. The small, elongated micro-dimples on AZ31 fracture surfaces (Figure 16D and 16G) are consistent with a mechanism involving microvoid coalescence (HELP or AIDE). The micro-dimples occur within macroscopically flat, quasi-crystallographic facets. Observations of dimples within cleavage-like facets on SCC fracture surfaces have previously been ascribed to crack propagation by alternating slip, as per AIDE [8, 22]. In this case, the orientation (if any) of the dimpled facets has not been determined. Thus, it is uncertain whether AIDE occurs. In contrast, the cleavage-like fracture surfaces for AM30 specimens (Figures 17E and 17G) are consistent with HEDE [8, 9, 11].

6.4 Fractography for AZ91

The fracture surfaces for AZ91 specimens fractured in distilled water under CERT conditions appear to be the result of a combination of mechanisms. The micrographs given in Winzer et al [10] and summarised in Figure 12 show that stress corrosion cracks are nucleated within β-particles ahead of the primary crack tip. Figures 8 and 9 show that the fracture of β-particles occurs by cleavage, which is characteristic of HEDE or DHC. There are no markings within the fractured β-particles to indicate crack arrest or plastic deformation, which usually accompany DHC, although plastic deformation might be considered unlikely for the relatively brittle β-phase. Moreover, there were no features within the fractured β-particles that could be interpreted as magnesium hydride. Thus, it is more likely that the mechanism for the fracture of β-particles is HEDE.

It was previously proposed that β-particles initially behave as H sinks, which fracture upon reaching some critical combination of internal H concentration and stress [10]. The influence of β-particles on the orientation of the fine parallel markings and ellipsoidal micro-dimples (Figures 8 and 9) in the α matrix indicates that β-particles subsequently act as sources of H for embrittlement of the surrounding matrix.

The mechanism for HE in the α matrix surrounding β-particles is uncertain. The contrast between the quasi-porous fracture surface morphology for AZ91 specimens pre-charged in gaseous H_2 and tested in distilled water at $3x10^{-8}$ s^{-1} (attributed to hydride precipitation and fracture) and those specimens tested in distilled water at higher strain rates indicates that the mechanism at higher strain rates does not involve hydride precipitation. The ellipsoidal micro-dimples observed within parallel facets on AZ91 fracture surfaces (Figure 8) resemble those observed within quasi-crystallographic facets on AZ31 fracture surfaces (Figures 16D and 16G) and are indicative of a mechanism involving microvoid coalescence (HELP or AIDE). If the fracture of β particles is accompanied by a reduction in their internal stress, then those particles may subsequently behave as sources of H for mobile dislocations. This would promote HELP in the surrounding matrix. Whether the fractured β particles act as sources of dislocations (as per AIDE) is unclear. In contrast, the coarse parallel markings, secondary cracking and jogging observed on AZ91 fracture surfaces [29] are consistent with the fractography given by Stampella et al [46] for pure Mg in Na_2SO_4 solution, Meletis and Hochman [3] for pure Mg in $NaCl\text{-}K_2CrO_4$ solution and Chakrapani and Pugh [47] and Wearmouth et al [48] for Mg-7.5Al in $NaCl\text{-}K_2CrO_4$ solutions. Meletis and Hochman proposed that such features were due to cleavage on $\{2\bar{2}03\}$ planes parallel to the direction of crack propagation. Since there are six $\{2\bar{2}03\}$ planes in the HCP crystal lattice, cleavage results in crystallographic 3-dimensional interlocking fracture surfaces. The previous workers did not observe micro-dimples between these coarse parallel markings. It may be important to note that they used alloys that did not contain Zn. Thus, the appearance of micro-dimples in AZ91 may be related to the influence of Zn on the diffusivity of H in the matrix. The coarse parallel markings may also be ascribed to the formation of steps between cracks between fractured β-particles and the primary crack tip (Figure 12B).

SCC initiation in AZ91 specimens was characterised by small, rounded fracture surface regions adjacent to the gauge surface. These regions contained fine parallel markings or micro-dimples similar to those observed within parallel facets on AZ91 fracture surfaces (for ongoing crack propagation) and within quasi-crystallographic facets on AZ31 fracture surfaces. It was previously speculated that these regions were formed subsequent to crack nucleation in β-phase particles (facilitated by H ingress at mechanically-induced film rupture sites) close to or at the gauge surface [10]; however, it is also conceivable that these regions correspond to crack initiation by AIDE.

6.5 Fractography for H_2 Pre-Charged Specimens

The similarity between the fracture surfaces for AZ91 specimens pre-charged in gaseous H_2 and those tested in distilled water at $3x10^{-8}$ s^{-1} indicates that the same HE mechanism occurs under both conditions. It is proposed that this mechanism involves: (i) nucleation and growth of MgH_2 particles; (ii) sudden fracture of the MgH_2 particles at some critical stress; and (iii) decomposition of the MgH_2 particles after fracture. The resulting fracture surface morphology is in stark contrast with the fractography for DHC in Zr alloys, which is characterised by cleavage-like markings with crack arrest markings perpendicular to the crack direction [12, 13, 14, 15, 16]. This contrast may be resolved in terms of differences in the plastic deformation associated with hydride precipitation in Mg and Zr alloys. The morphology also contradicts previous associations between cleavage-like SCC fracture surfaces for Mg alloys with the DHC mechanism [3, 4, 5, 6].

The contrast between the fracture surfaces for specimens tested in distilled water at $3x10^{-8}$ s^{-1} and those tested at higher strain rates indicates a change in HE mechanism. Fracture surfaces for specimens tested in distilled water at $3x10^{-8}$ s^{-1} contain an SCC zone (consisting of parallel facets, jogging and secondary cracking) adjacent to the surface, with the remaining fracture surface consisting of quasi-porous features (Figure 10). This suggests that there is some critical crack length at which H concentration in the remaining metal exceeds the solvus concentration. H is transported ahead of the crack tip by stress-assisted diffusion or with mobile dislocations. Consequently, the H concentration in the remaining metal increases with crack length. The solvus concentration in the remaining metal is reduced by the applied tensile stress and the hydrostatic component of the crack tip stress field. Thus, at low strain rates more time is available for the H concentration in the remaining matrix to exceed the solvus concentration.

The analysis in Section 5 shows that the H concentration imparted by charging in gaseous H_2 is close to the solvus concentration, and that the solvus concentration decreases by several orders of magnitude upon cooling. Under certain conditions H entry in Mg is inhibited by formation of a thin hydride layer at the surface [49, 50, 51, 52, 53]. That the quasi-porous morphology is spread uniformly across the entire fracture surface for H_2-charged specimens suggests that H entry was not limited by hydride precipitation at the surface and that H had diffused throughout the specimen. This supports the key assumptions: that H solubility obeys Sieverts' Law; that the concentration distribution reaches equilibrium during charging in gaseous H_2; that the H concentration does not exceed the solvus concentration under charging conditions; and that hydrides are precipitated during cooling.

It is uncertain why MgH_2 is not apparent on the final fracture surface. One possibility is that fracture of each MgH_2 particle is accompanied by a sudden release of hydrostatic stress, resulting in decomposition of the particle; however, this aspect of the mechanism has not yet been investigated. Nevertheless, the smooth nature of the fracture surface is consistent with a plastically deformed Mg surface at the metal/hydride interface.

6.6 Summary of Mechanisms

Table 1 summarises the proposed mechanisms for SCC/HE of AZ91, AZ31 and AM30 in distilled water and after pre-charging in H_2 gas based on fractographic evidence.

Alloy	**Environment**	**Strain Rate**	**SCC Initiation Mechanism**	**SCC Propagation Mechanism**
AZ91	Distilled water	10^{-7} s^{-1} – $5x10^{-7}$ s^{-1}	HEDE in β-particles or AIDE (uncertain)	HEDE in β-particles, HELP and/or AIDE in bulk matrix
AZ91	Distilled water	$3x10^{-8}$ s^{-1}	HEDE in β-particles or AIDE (uncertain)	HEDE in β-particles, HELP and/or AIDE in bulk matrix, MgH_2 formation, HEDE in MgH_2 particles, dissolution of MgH_2.
AZ91	H_2 gas (pre-charged)	10^{-4} s^{-1}	-	MgH_2 formation, HEDE in MgH_2 particles, dissolution of MgH_2.
AZ31	Distilled water	$5x10^{-8}$ s^{-1} –	Localised	HELP and/or AIDE

		$8x10^{-7}$ s^{-1}	Dissolution	
AM30	Distilled water	10^{-7} s^{-1} – $5x10^{-7}$ s^{-1}	Localised Dissolution	HEDE

Table 1 – Summary of proposed mechanisms for SCC/HE of Mg-Al alloys based on fractographic evidence

7 Conclusions

- The mechanisms for stress corrosion crack initiation for AZ31 and AM30 involve localised dissolution.
- The fractography indicates that the mechanisms for stress corrosion crack propagation in AZ31 and AM30 are different.
- The fractography for SCC propagation in AZ31 is characterised by elongated micro-dimples within quasi-crystallographic facets, indicative of a mechanism involving microvoid coalescence (HELP and/or AIDE). The occurrence of dimples within cleavage-like facets is a characteristic of AIDE [8, 22]; however, it is uncertain whether the facets observed on AZ31 fracture surfaces correspond to specific planes.
- The fractography for SCC propagation in AM30 is characterised by cleavage-like features, indicative of HEDE.
- The mechanism for SCC propagation in AZ91 involves crack nucleation within β–particles ahead of the primary crack tip. The fracture morphology for the β-particles is indicative of HEDE.
- The fracture surfaces for SCC propagation in AZ91 under strain rates of 10^{-7} s^{-1} to $5x10^{-7}$ s^{-1} contain fine parallel markings and ellipsoidal micro-dimples indicative of AIDE and/or HELP. The orientation of these markings is influenced by β particles. This is consistent with a mechanism involving crack nucleation within β particles (as shown in Winzer et al [10]), with β particles subsequently acting sources of H for embrittlement of the surrounding matrix.
- AZ91 specimens pre-charged in gaseous H_2 and AZ91 specimens fractured in distilled water at $3x10^{-8}$ s^{-1} have similar fracture surfaces, indicating that the same HE mechanism occurs under both conditions. This mechanism involves: (i) nucleation and growth of MgH_2 particles; (ii) sudden fracture of the MgH_2 particles at some critical stress; and (iii) decomposition of the MgH_2 particles after fracture.
- An analysis of the H concentration imparted by charging in gaseous H_2 and the influence of cooling and stress application on the solvus concentration showed that this mechanism is viable.

Acknowledgements

The authors wish to thank the GM Technical Centre at Warren MI, the Australian Research Council (ARC) and the Australian Research Network for Advanced Materials (ARNAM) for research support. N. Winzer and A. Atrens wish to thank GKSS-Forschungszentrum Geesthacht GmbH for allowing them to visit between 2005 and 2007. V. Heitmann, U. Burmeister and V. Kree of GKSS are thanked for their assistance with experiments, fractography and metallography.

References

[1] N. Winzer, A. Atrens, G. Song, E. Ghali, W. Dietzel, K.U. Kainer, N. Hort and C. Blawert, Adv. Eng. Mater., 2005, vol. 8, pp. 659-693

[2] S.P. Lynch, P. Trevena, Corrosion, 1988, vol. 44, pp. 113-124

[3] E.I. Meletis, R.F. Hochman, Corrosion, 1984, vol. 40, pp. 39-45

[4] D.G. Chakrapani, E.N. Pugh, Metall. Trans. A, 1976, vol. 7, pp. 173-178

[5] A.J. Bursle, E.N. Pugh, in: P.R. Swann, F.P. Ford, A.R.C. Westwood (Eds.), Mechanisms of Environment Sensitive Cracking of Materials, Materials Society, London, 1977, pp. 471-481

[6] G.L. Makar, J. Kruger, K. Sieradzki, Corros. Sci., 1993, vol. 34, pp. 1311-1342

[7] H.K. Birnbaum, in: N.R. Moody, A.W. Thompson (Eds.), Hydrogen Effects on Material Behavior, TMS, Warrendale, 1990, pp. 639-660

[8] S.P. Lynch, in: N.R. Moody, A.W. Thompson, R.E. Ricker, G.W. Was, R.H. Jones (Eds.), Hydrogen Effects on Material Behavior and Corrosion Deformation Interactions, TMS, Warrendale, 2003, pp. 449-466

[9] R.P. Gangloff, in: I. Milne, R.O. Ritchie, B. Karihaloo (Eds.), Comprehensive Structural Integrity, Elsevier, Oxford, 2003, 6.02, pp. 31-101

[10] N. Winzer, A. Atrens, W. Dietzel, V.S. Raja, G. Song, K.U. Kainer, Mat. Sci. Eng. A, article under review

[11] C.E. Coleman, in: I. Milne, R.O. Ritchie, B. Karihaloo (Eds.), Comprehensive Structural Integrity, Elsevier, Oxford, 2003, 6.03, pp. 103-161

[12] B. Cox, in: Proc. Metallography and Corrosion Symp., IMS Annual Conf., Calgary, NACE, 1986, pp. 153-174

[13] B. Cox, J. Nucl. Mater., 1990, vol. 170, pp. 1-23

[14] K. Nuttall, A.J. Rogowski, J. Nucl. Mater., 1979, vol. 80, pp. 279-290

[15] G.K. Shek, M.T. Jovanovic, H. Seahra, Y. Ma, D. Li, R.L. Eadie, J. Nucl. Mater., 1996, vol. 231, pp. 221-230

[16] L.A. Simpson, Mechanical Behaviour of Materials, 1979, vol. 2, pp. 445-455

[17] S.Q. Shi, M.P. Puls, J. Nucl. Mater., 1994, vol. 208, pp. 232-242

[18] S.Q. Shi, M.P. Puls, S. Sagat, J. Nucl. Mater., 1994, vol. 208, pp. 243-250

[19] R. Dutton, K. Nuttall, M.P. Puls, L.A. Simpson, Metall. Trans. A, 1977, vol. 8, pp. 1553-1562

[20] H.P. Van Leeuwen, Eng. Fract. Mech., 1974, vol. 6, pp. 141-161

[21] N. Winzer, A. Atrens, W. Dietzel, G. Song, K.U. Kainer, Mat. Sci. Eng. A, 2007, vol. 466, pp. 18–31

[22] S.P. Lynch, Acta. Metall., 1988, vol. 34, pp. 2639-2661

[23] A. Atrens, C.C. Brosnan, S. Ramamurthy, A. Oehlert, I.O. Smith, Meas. Sci. Technol., 1993, vol. 4, pp. 1281-1292

[24] W. Dietzel, K.H. Schwalbe, Z. Materialprüfung, 1986, vol. 28, pp. 368-372

[25] A. Oehlert, A. Atrens, J Mater. Sci., 1998, vol. 33, pp. 775-781

[26] A. Oehlert, A. Atrens, J Mater. Sci., 1997, vol. 32, pp. 6519-6523

[27] A. Oehlert, A. Atrens, Corros. Sci., 1996, vol. 38, pp. 1159-1170

[28] A. Oehlert, A. Atrens, Acta Metall. Mater., 1994, vol. 42, pp. 1493-1508

[29] N. Winzer, A. Atrens, W. Dietzel, G. Song, K.U. Kainer, Mat. Sci. Eng. A, 2007, doi:10.1016/j.msea.2007.03.021 (article in press)

[30] N. Winzer, A. Atrens, W. Dietzel, G. Song, K.U. Kainer, Mat. Sci. Eng. A, article to be submitted

[31] C. Nishimura, M. Komaki, M. Amano, J. Alloy. Compd., 1999, vol. 293-295, pp. 329-333.
[32] V.I. Shapalov, A.P. Semik, A.G. Timchenko, Metally/Ross Akad Nauk (Russ Metall), 1993, vol. 3, pp. 25-28
[33] V.I Shapalov, N.P. Serdyuk, O.P. Semik, Dop Akad Nauk Ukr RSR, Ser A, Fiz-Mat Tekh Nauki, 1981, vol. 6, pp. 99-101
[34] J. Koeneman, A.G. Metcalfe, Trans. Am. Soc. Met., 1959, vol. 51, pp. 1072-1082
[35] Y.C. Huang, T. Watanabe, R. Komatsu, in: Proc 4th Inter Conf Vacuum Metallurgy, Tokyo, 1973, pp. 176-179
[36] Z.D. Popovic, G.R. Piercy, Metall. Trans A, 1975, vol. 6, pp. 1915-1917
[37] T. Watanabe, Y.C. Huang, R. Komatsu, J Jpn Inst Light Met, 1975, vol. 26, pp. 76-81
[38] K. Zeng, T. Klassen, W. Oelerich, R. Bormann, Int. J. Hydrogen Energ., 1999, vol. 24, pp. 989-1004
[39] S.Q. Shi, J. Nucl. Mater., 1999, vol. 275, pp. 318-323
[40] N. Winzer, A. Atrens, W. Dietzel, G. Song, K.U. Kainer, Mat. Sci. Eng. A, 2007, vol. 466, pp. 18–31
[41] M.P. Puls, Acta Metall. Mater., 1981, vol. 29, pp. 1961-1968
[42] J. Lufrano, P. Sofronis, H.K. Birnbaum, J. Mech. Phys. Solids, 1996, vol. 44, pp. 179-205
[43] A.G. Varias, A.R. Massih, J. Mech. Phys. Solids, 2002, vol. 50, pp. 1469-1510
[44] F.H. Ellinger, C.E. Holley, Jr., B.B. McInteer, D. Pavone, R.M. Potter, E. Staritzky, W.H. Zachariasen, J. Am. Chem. Soc., 1955, vol. 77, pp. 2647-2648
[45] T.L. Anderson, Fracture Mechanics: Fundamentals and Applications, 3rd ed., CRC, Boca Raton, USA, 2004
[46] R.S. Stampella, R.P.M. Proctor, V. Ashworth, Corros. Sci., 1984, vol. 24, pp. 325-341
[47] D.G. Chakrapani, E.N. Pugh, Corrosion, 1975, vol. 31, pp. 247-252
[48] W.R. Wearmouth, G.P. Dean, R.N. Parkins, Corrosion, 1973, vol. 29, pp. 251-258
[49] A. Krozer, B. Kasemo, J. Less-Common Met., 1990, vol. 160, pp. 323-342
[50] A. Krozer, B. Kasemo, J. Phys.: Condens. Matter, 1989, vol. 1, pp. 1533-1538
[51] V.P. Zhdanov, A. Krozer, B. Kasemo, Phys. Rev. B, 1993, vol. 47, pp. 11044-11048
[52] P. Hjort, A. Krozer, B. Kasemo, J. Alloy Compd., 1996, vol. 237, pp. 74-80
[53] P. Hjort, A. Krozer, B. Kasemo, J. Alloy Compd., 1996, vol. 234, pp. L11-L15

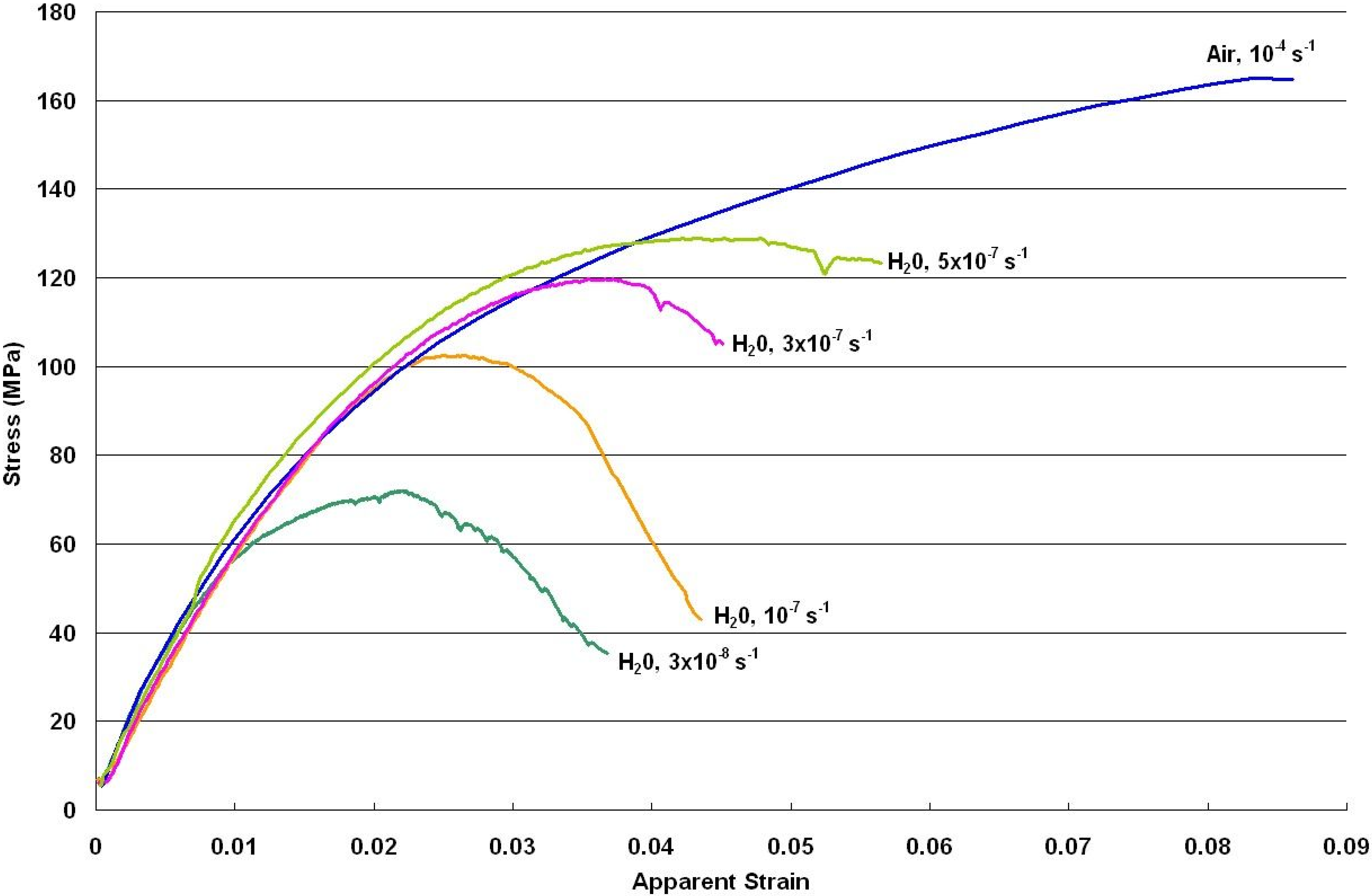
Stress (MPa)
180
160
140
120
100
80
60
40
20
0
0
0.01
0.02
0.03
0.04
0.05
0.06
0.07
0.08
0.09
Apparent Strain
Air, 10^{-4} s^{-1}
H_20, $5x10^{-7}$ s^{-1}
H_20, $3x10^{-7}$ s^{-1}
H_20, 10^{-7} s^{-1}
H_20, $3x10^{-8}$ s^{-1}

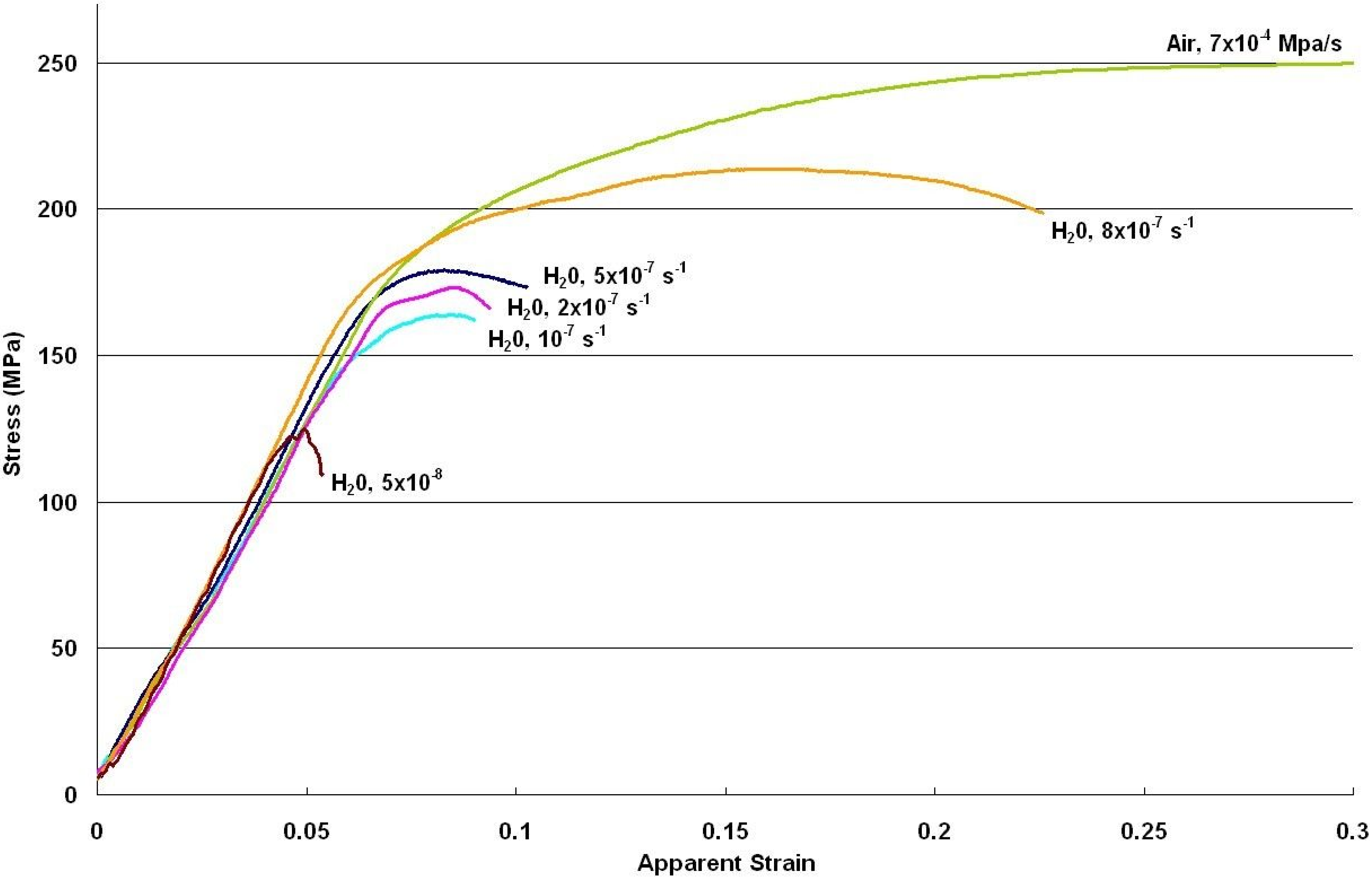
Air, $7x10^{-4}$ Mpa/s
H_20, $8x10^{-7}$ s^{-1}
H_20, $5x10^{-7}$ s^{-1}
H_20, $2x10^{-7}$ s^{-1}
H_20, 10^{-7} s^{-1}
H_20, $5x10^{-8}$
Stress (MPa)
0
50
100
150
200
250
0
0.05
0.1
0.15
0.2
0.25
0.3
Apparent Strain

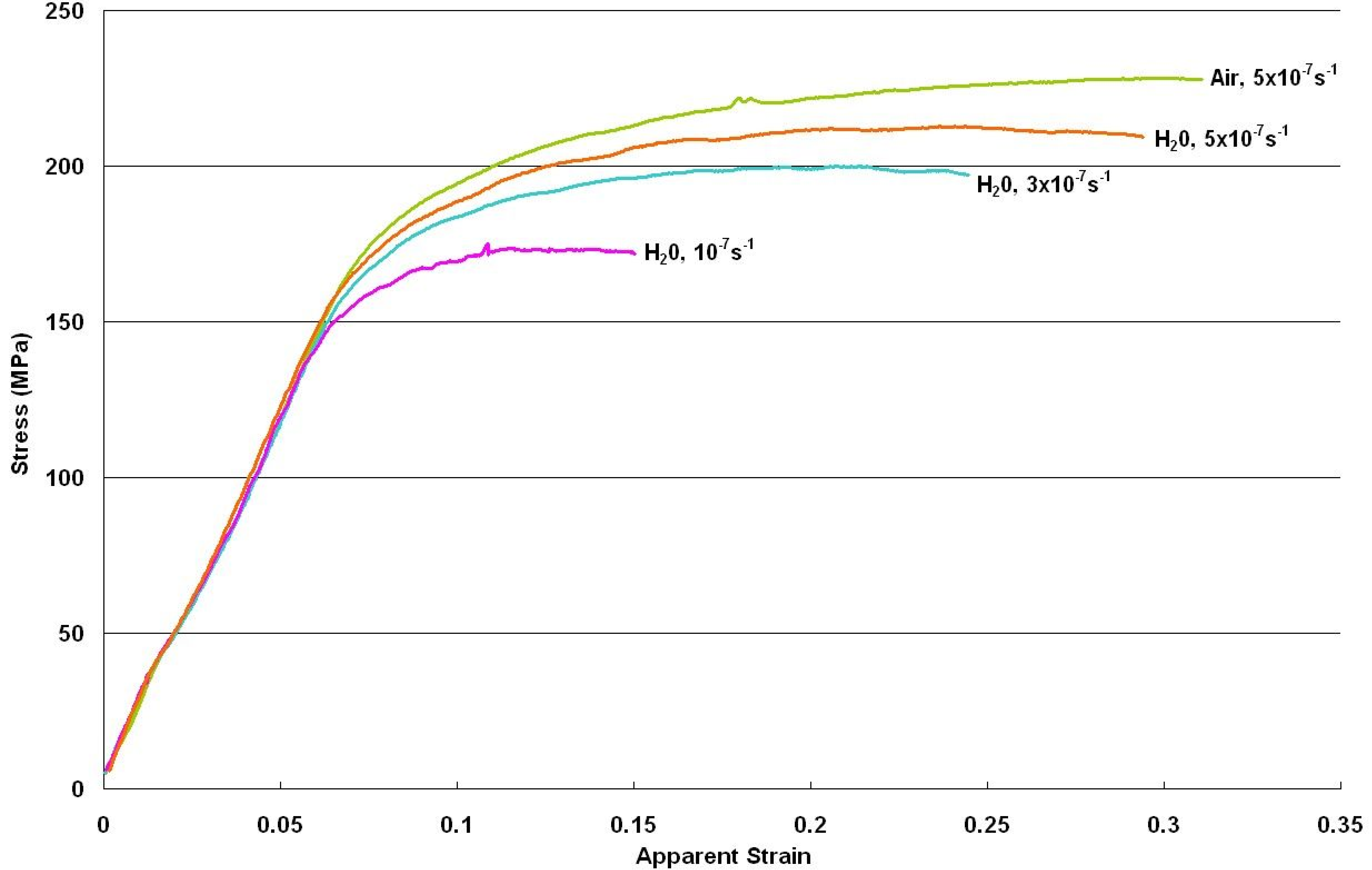
250
200
150
100
50
0
Stress (MPa)
0
0.05
0.1
0.15
0.2
0.25
0.3
0.35
Apparent Strain
Air, $5x10^{-7}s^{-1}$
H_20, $5x10^{-7}s^{-1}$
H_20, $3x10^{-7}s^{-1}$
H_20, $10^{-7}s^{-1}$

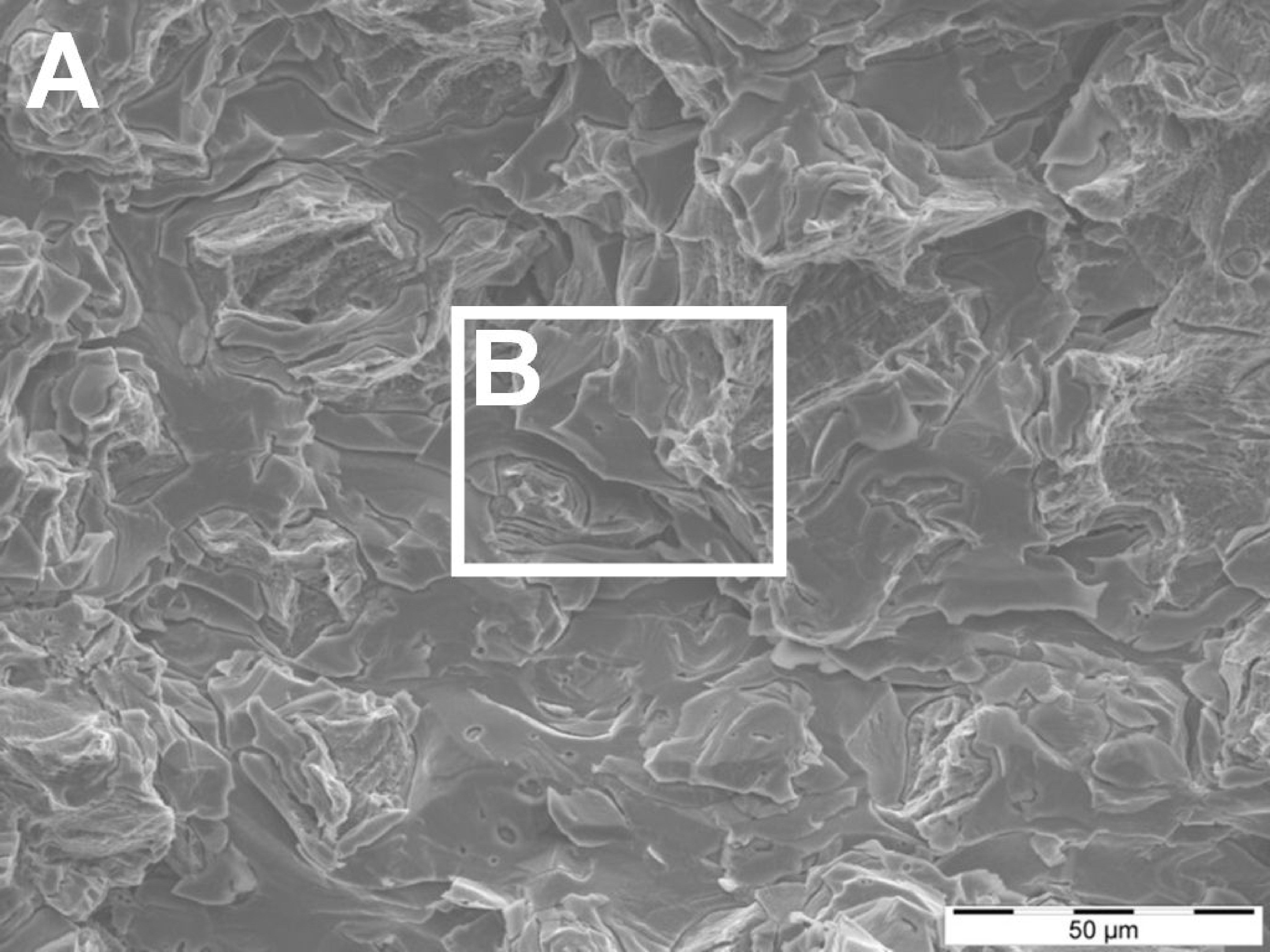
A
B
50 µm

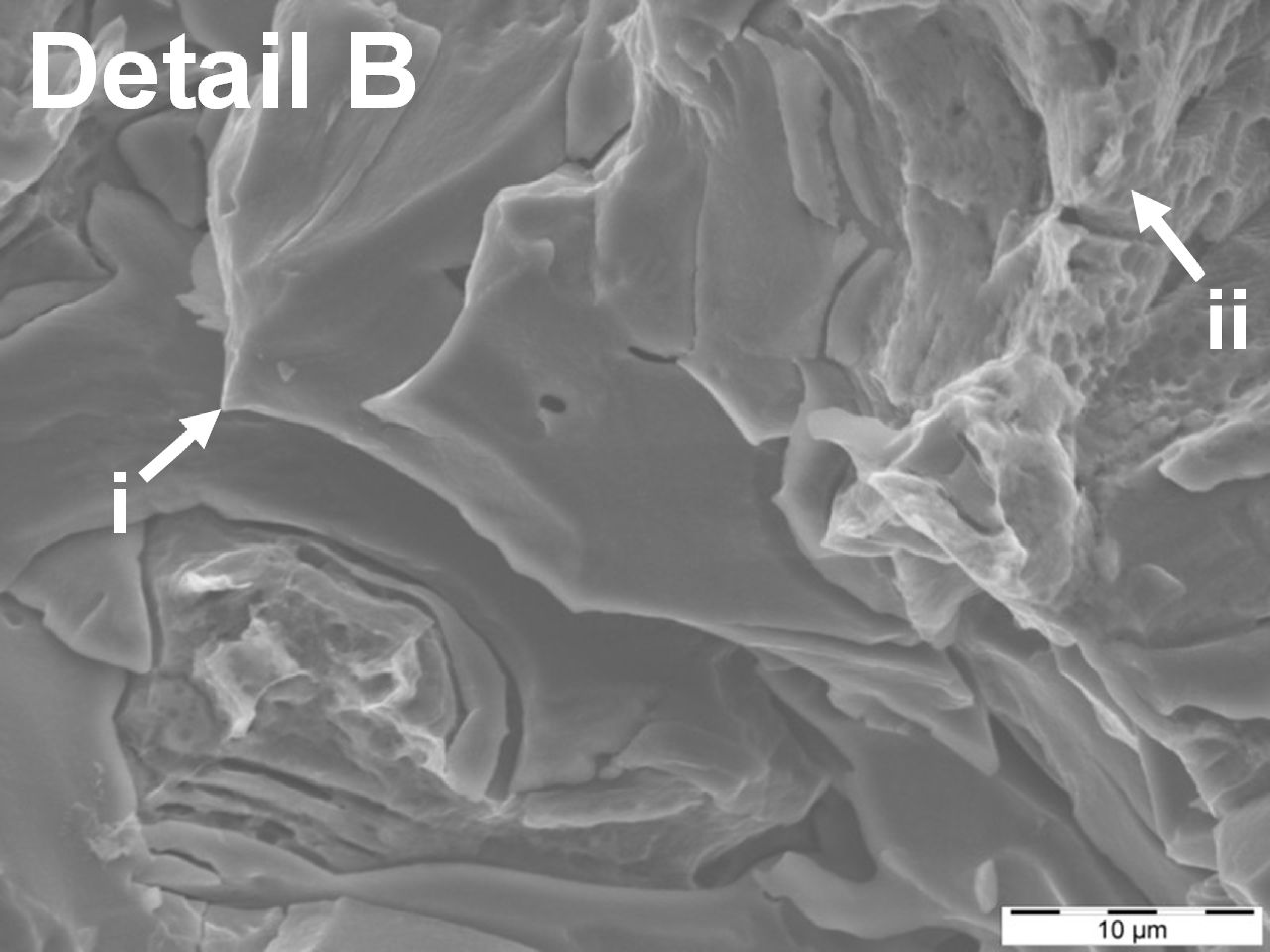
Detail B
ii
i
10 µm

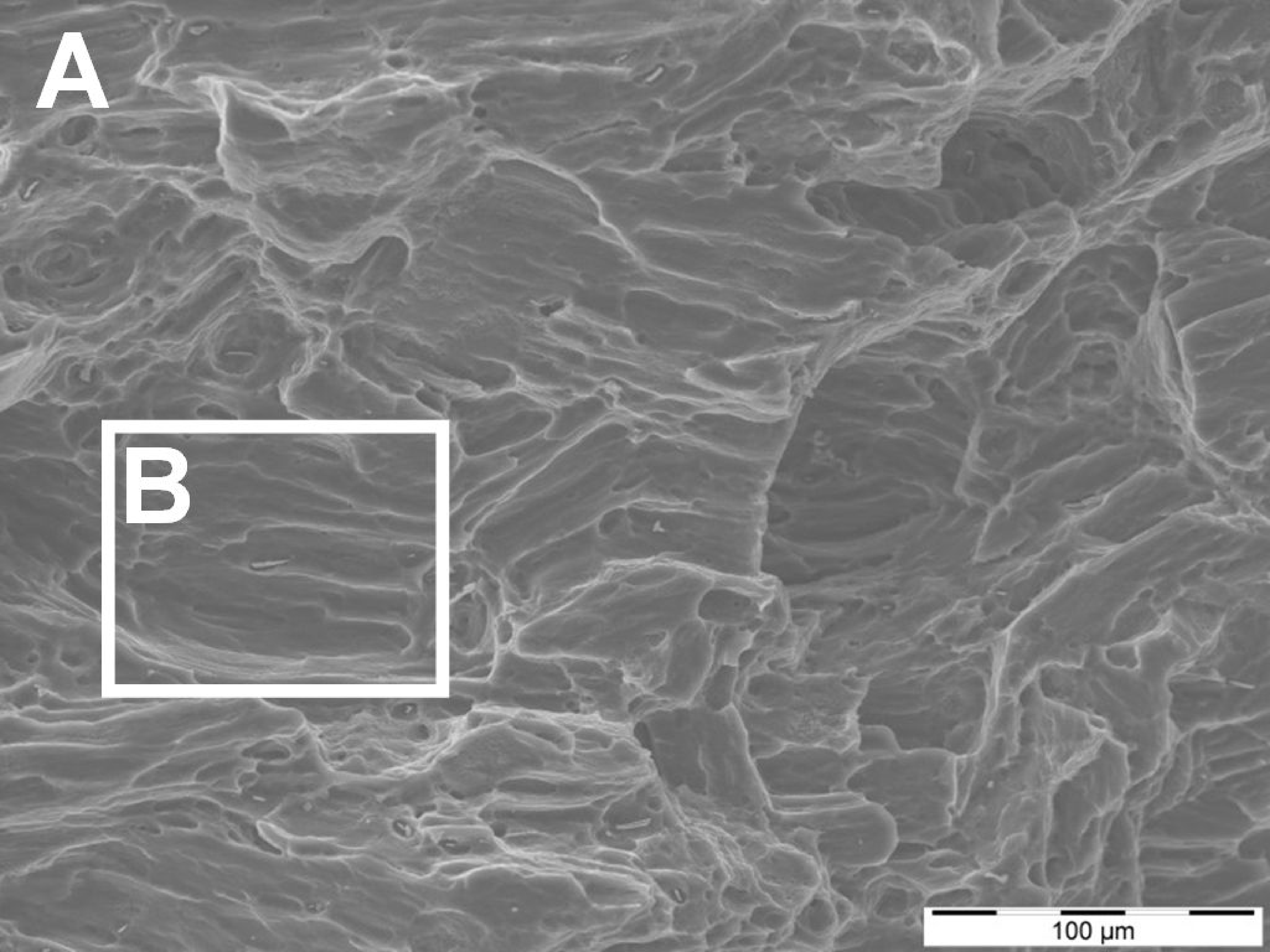
A
B
100 µm

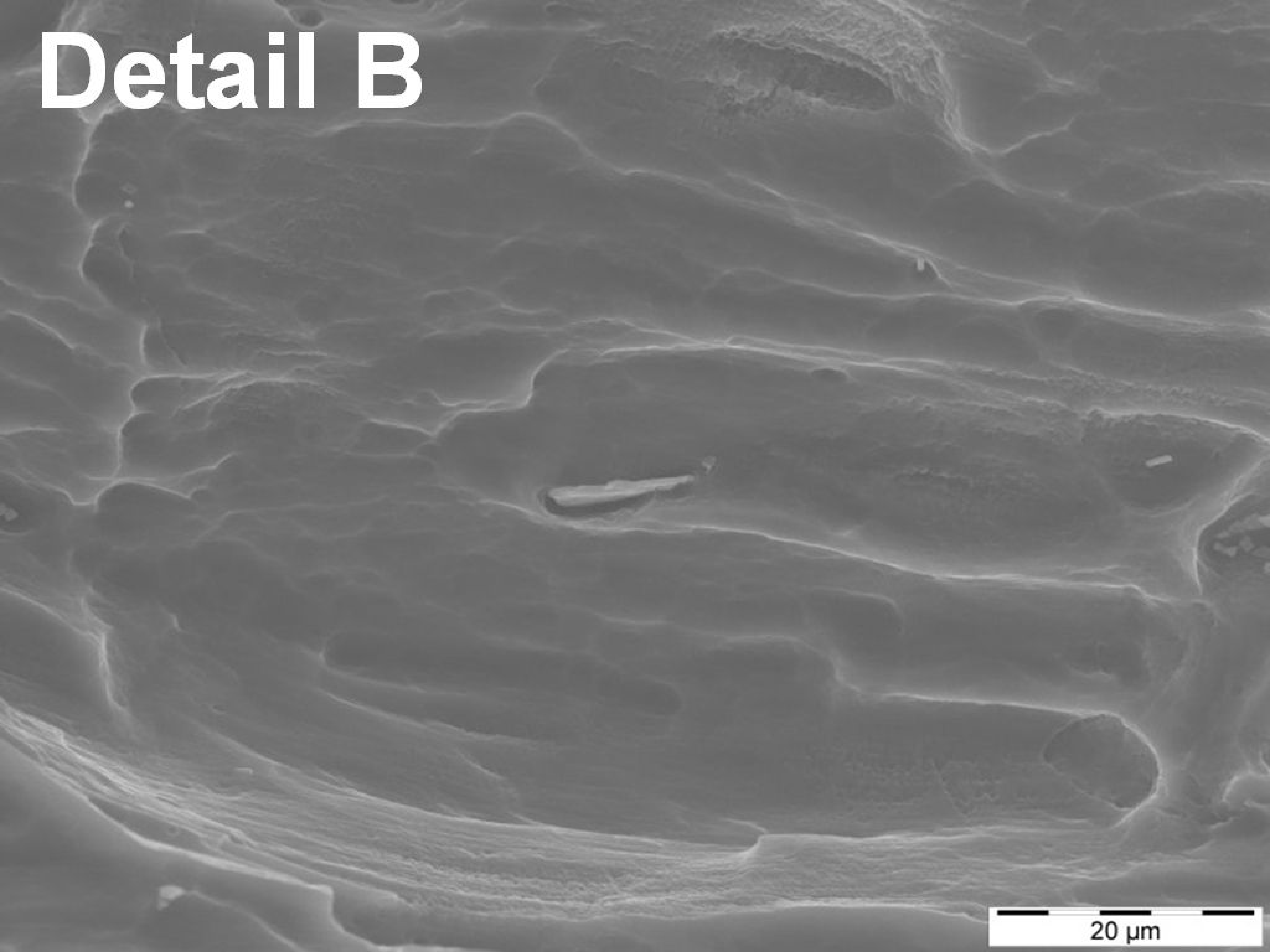
Detail B
20 µm

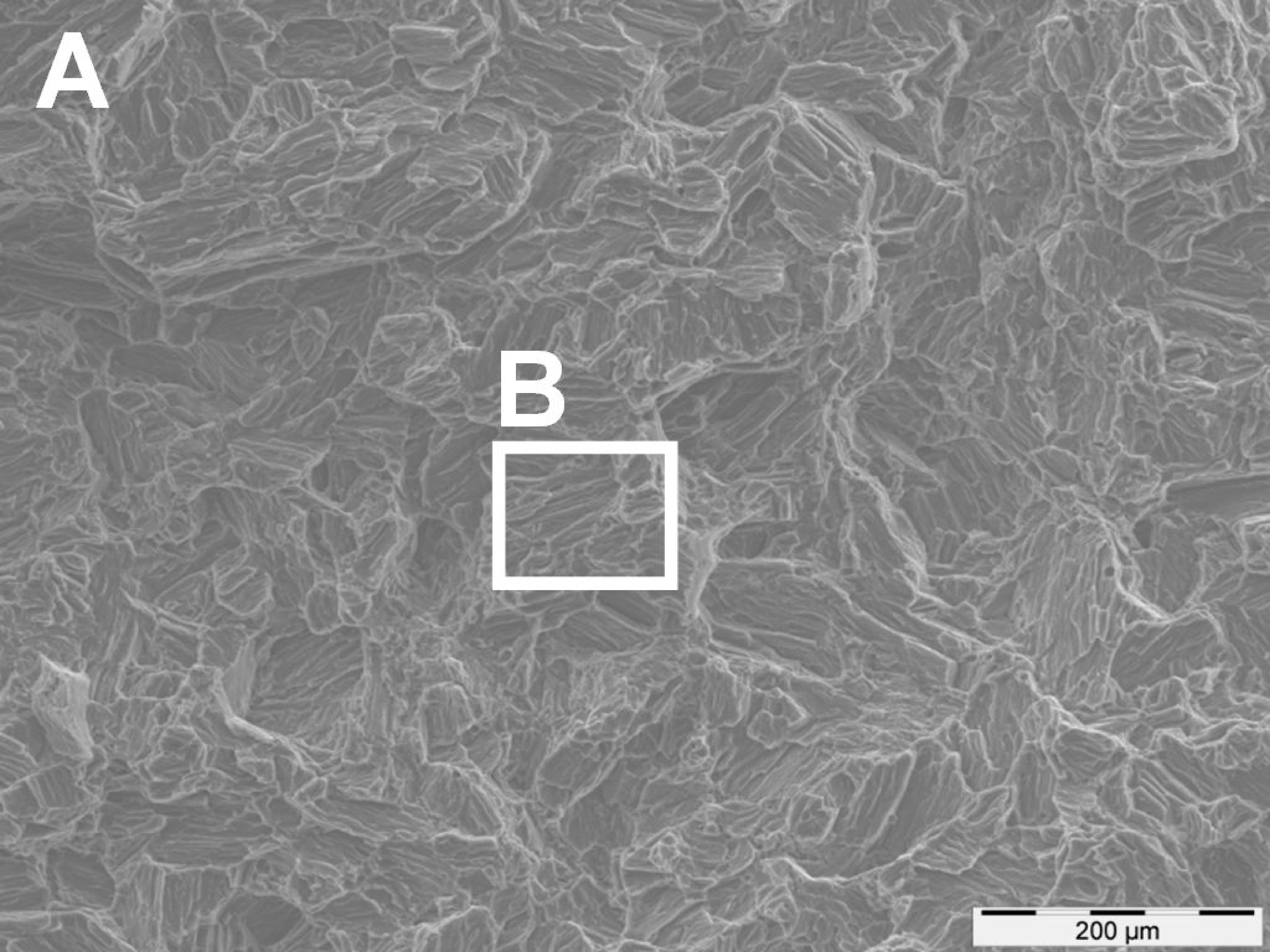
A
B
200 µm

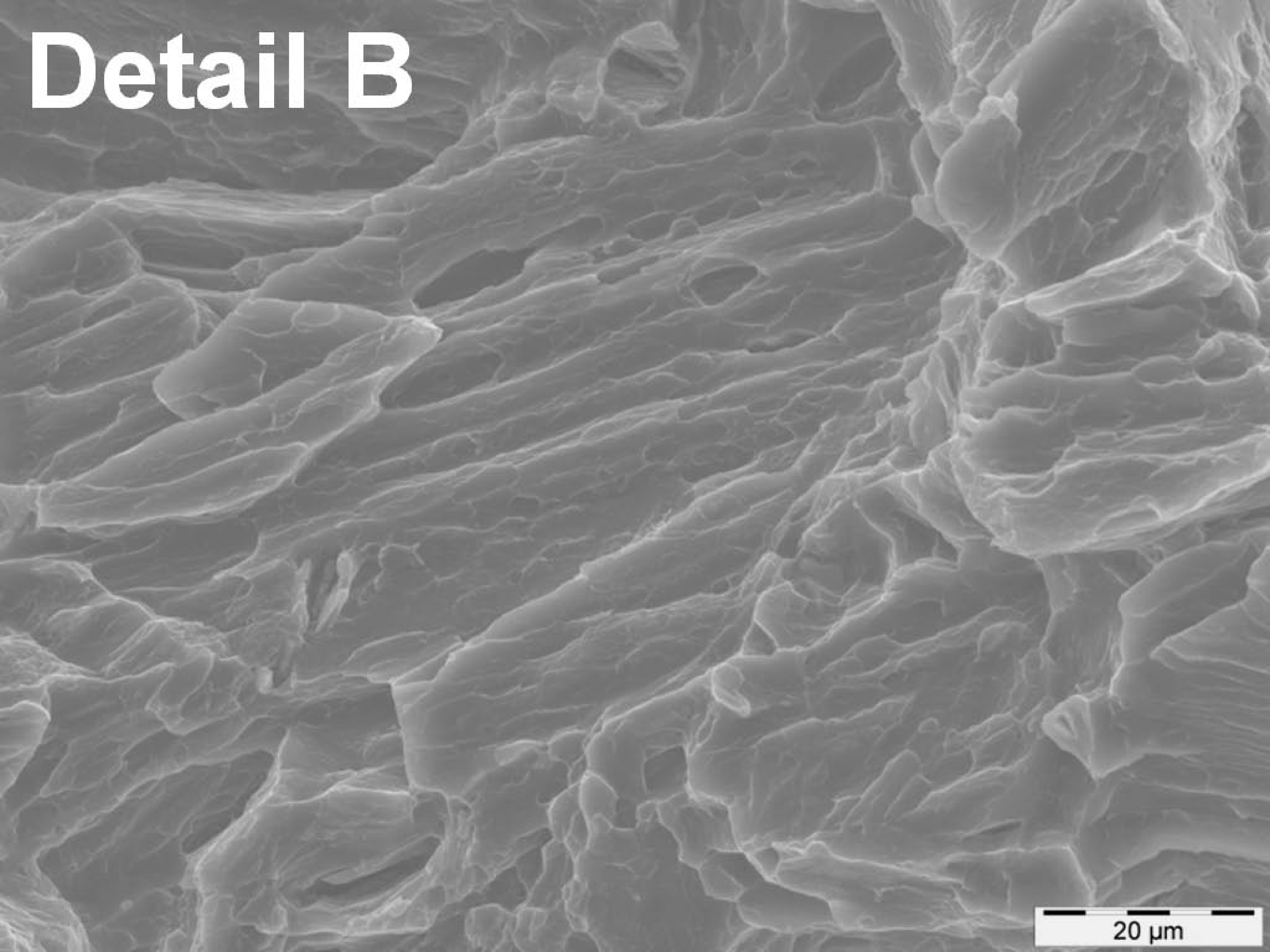
Detail B
20 µm

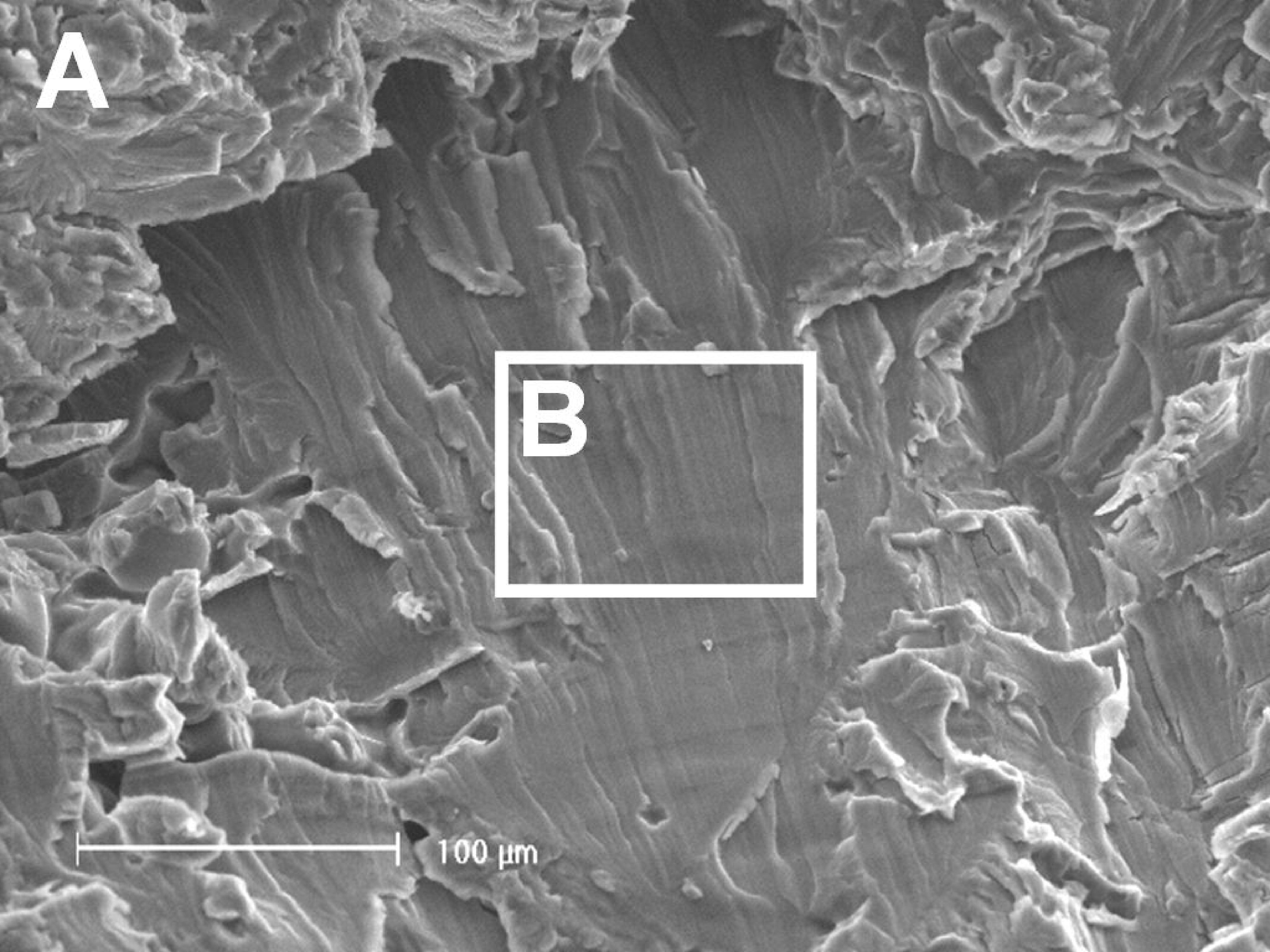
A
B
100 µm

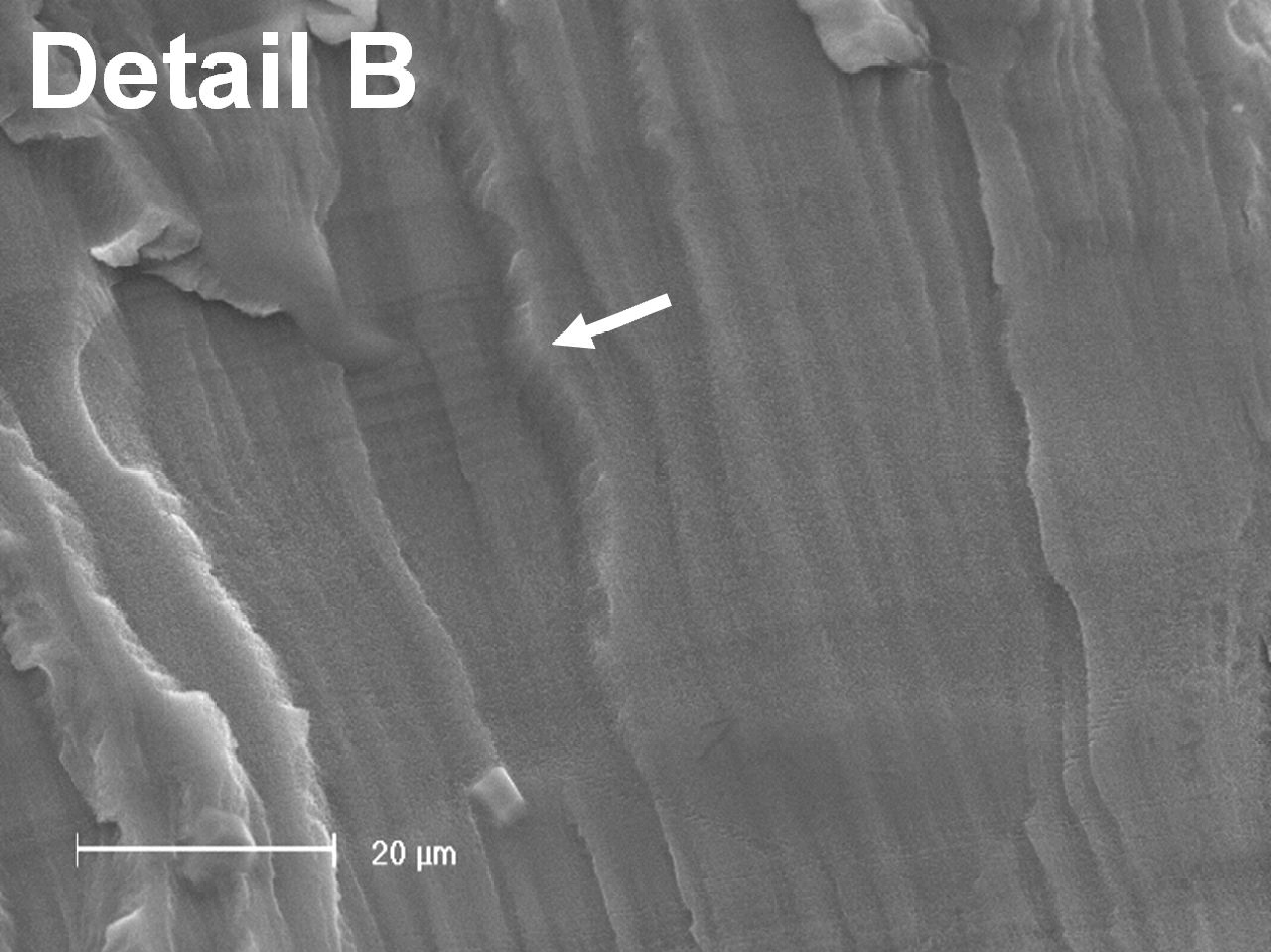
Detail B
20 µm

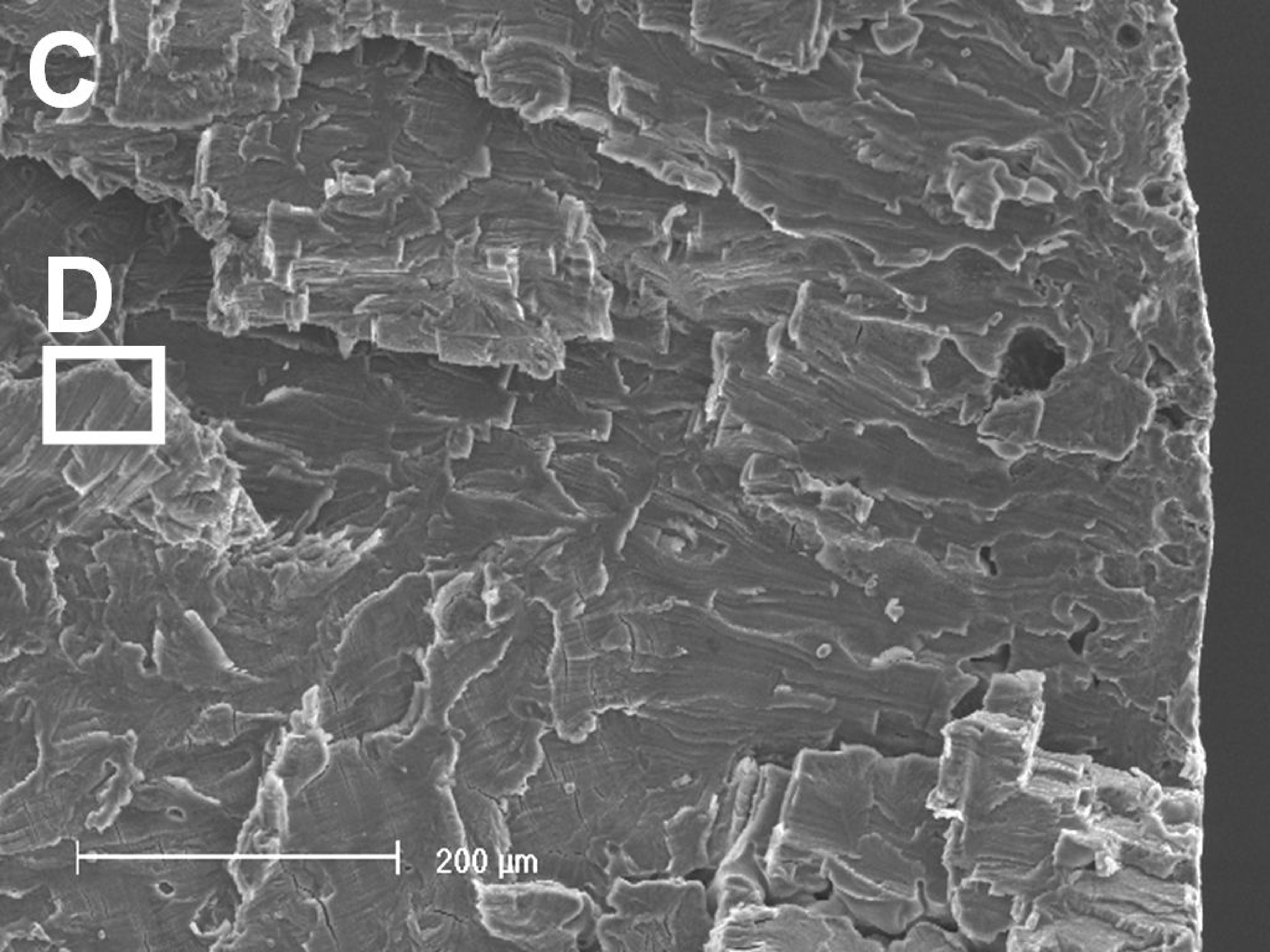
C
D
200 µm

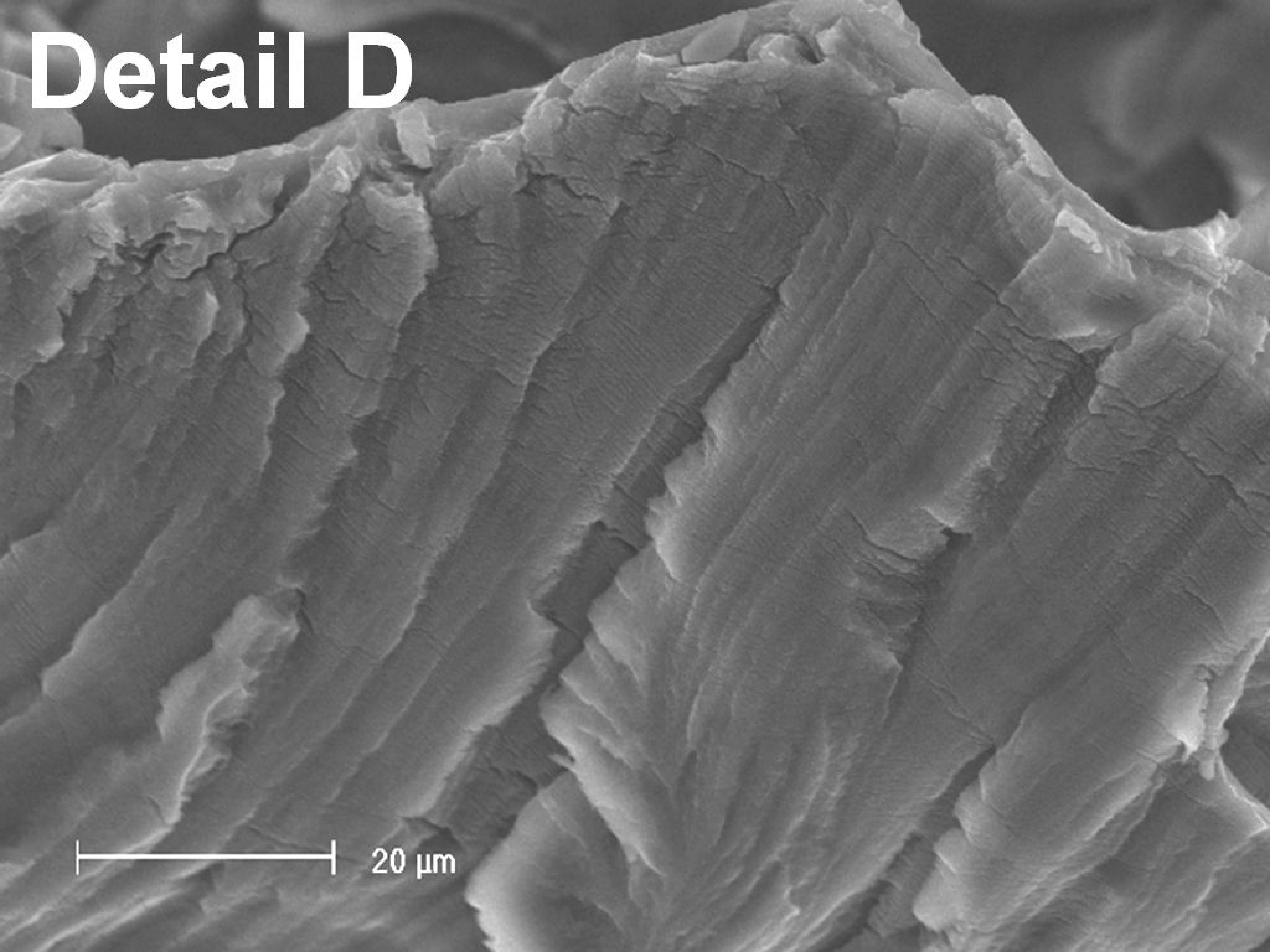

Detail D

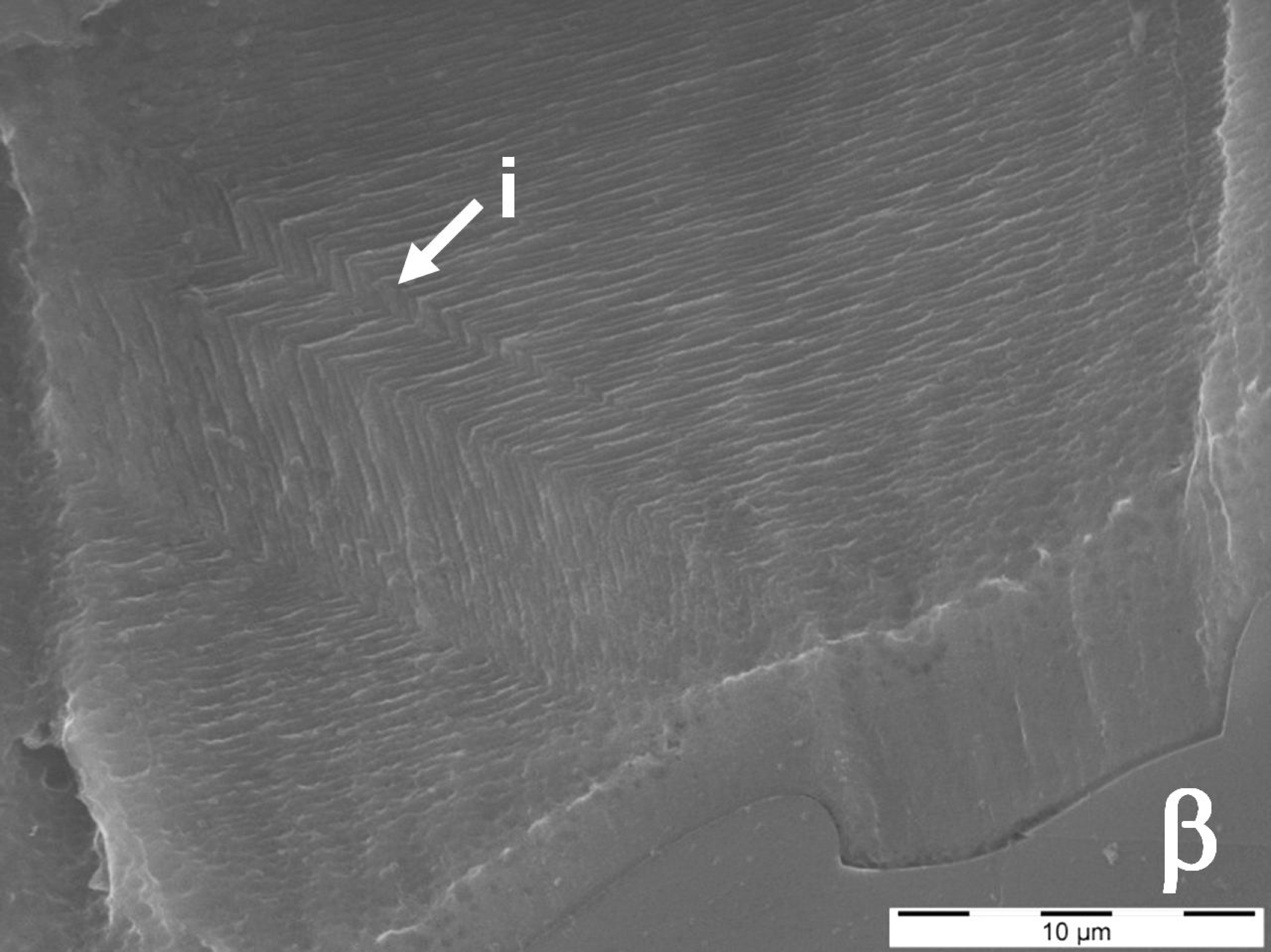
i
β
10 µm

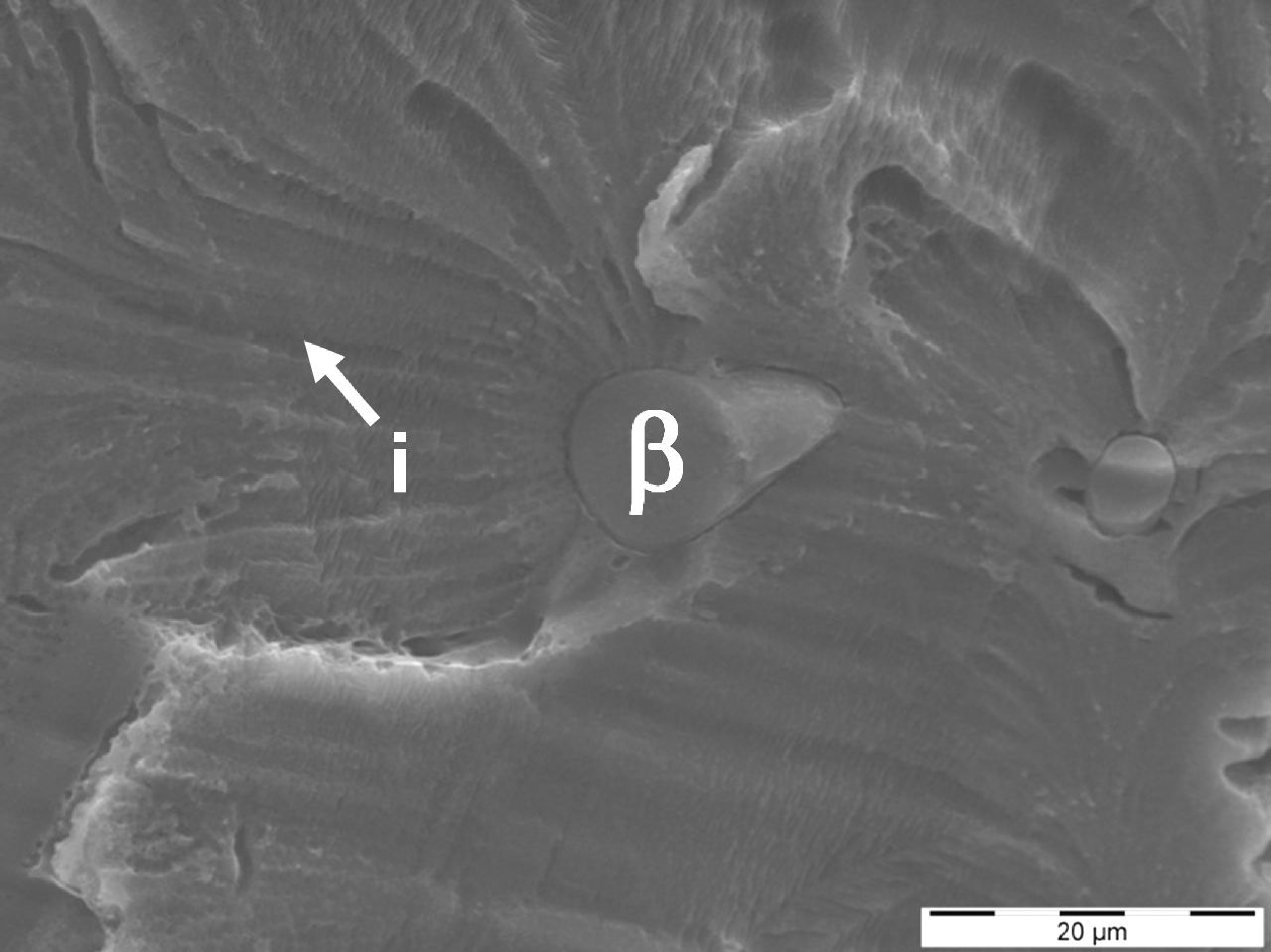
i
β
20 µm

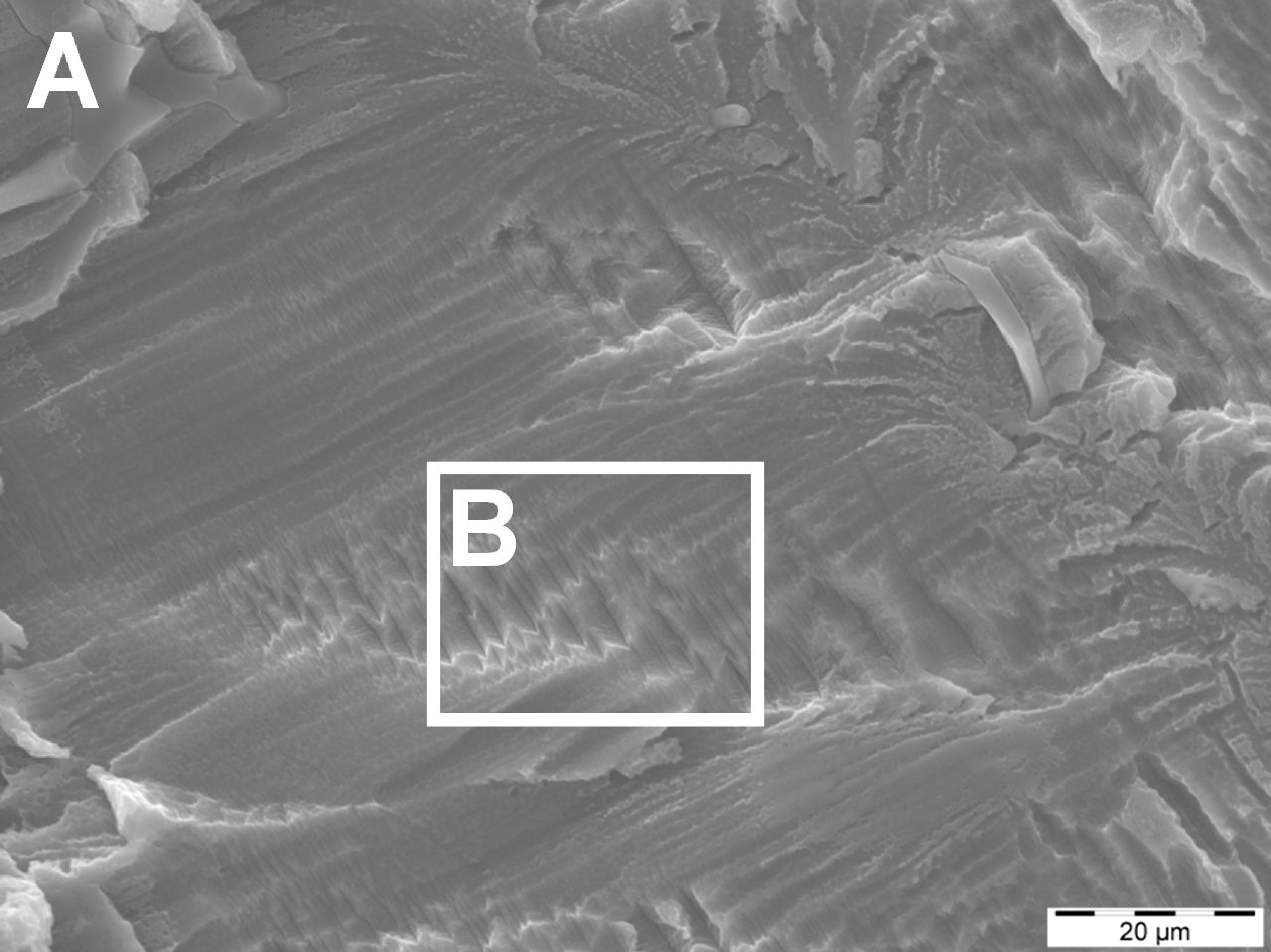
A
B
20 µm

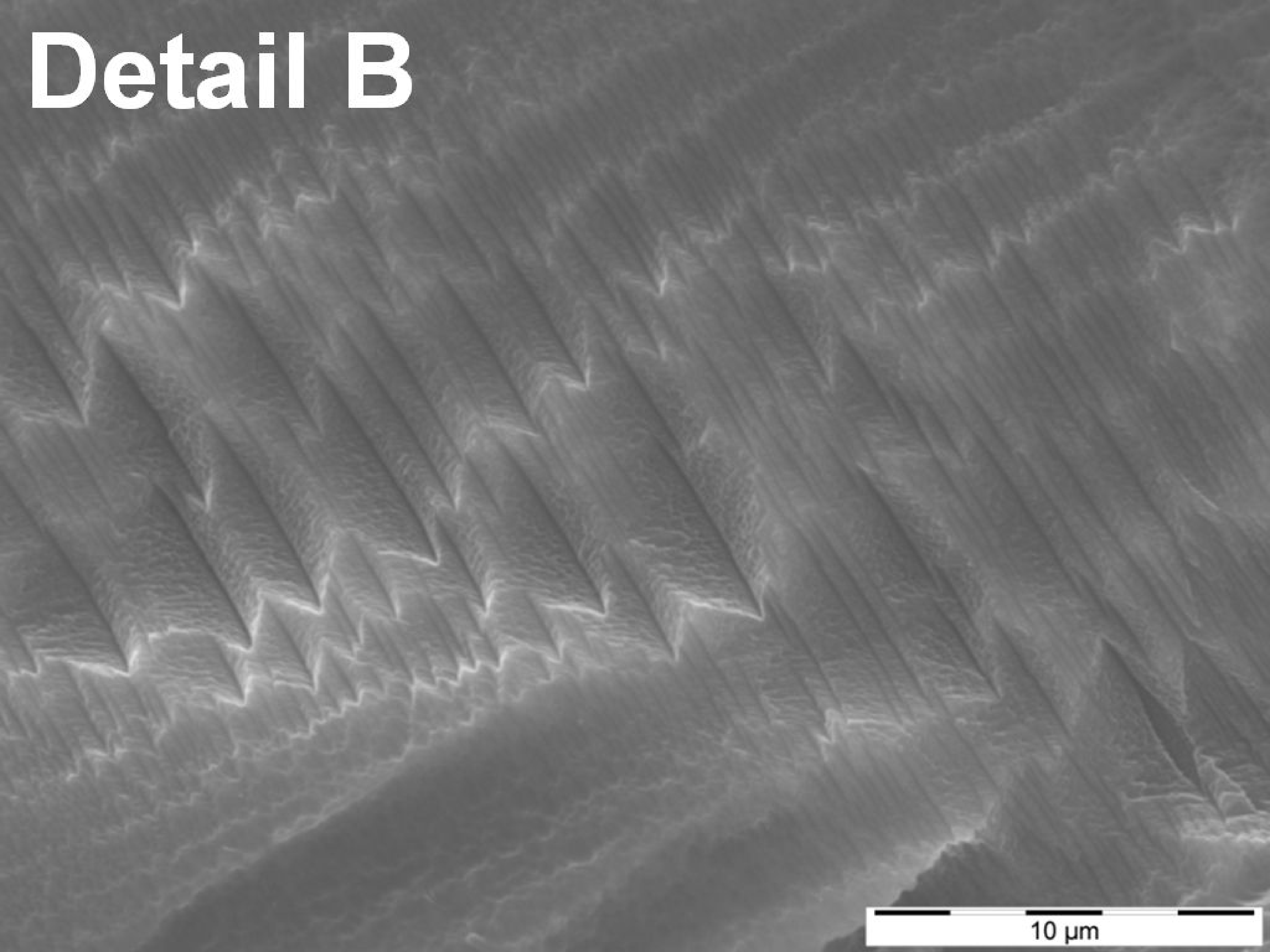
Detail B
10 µm

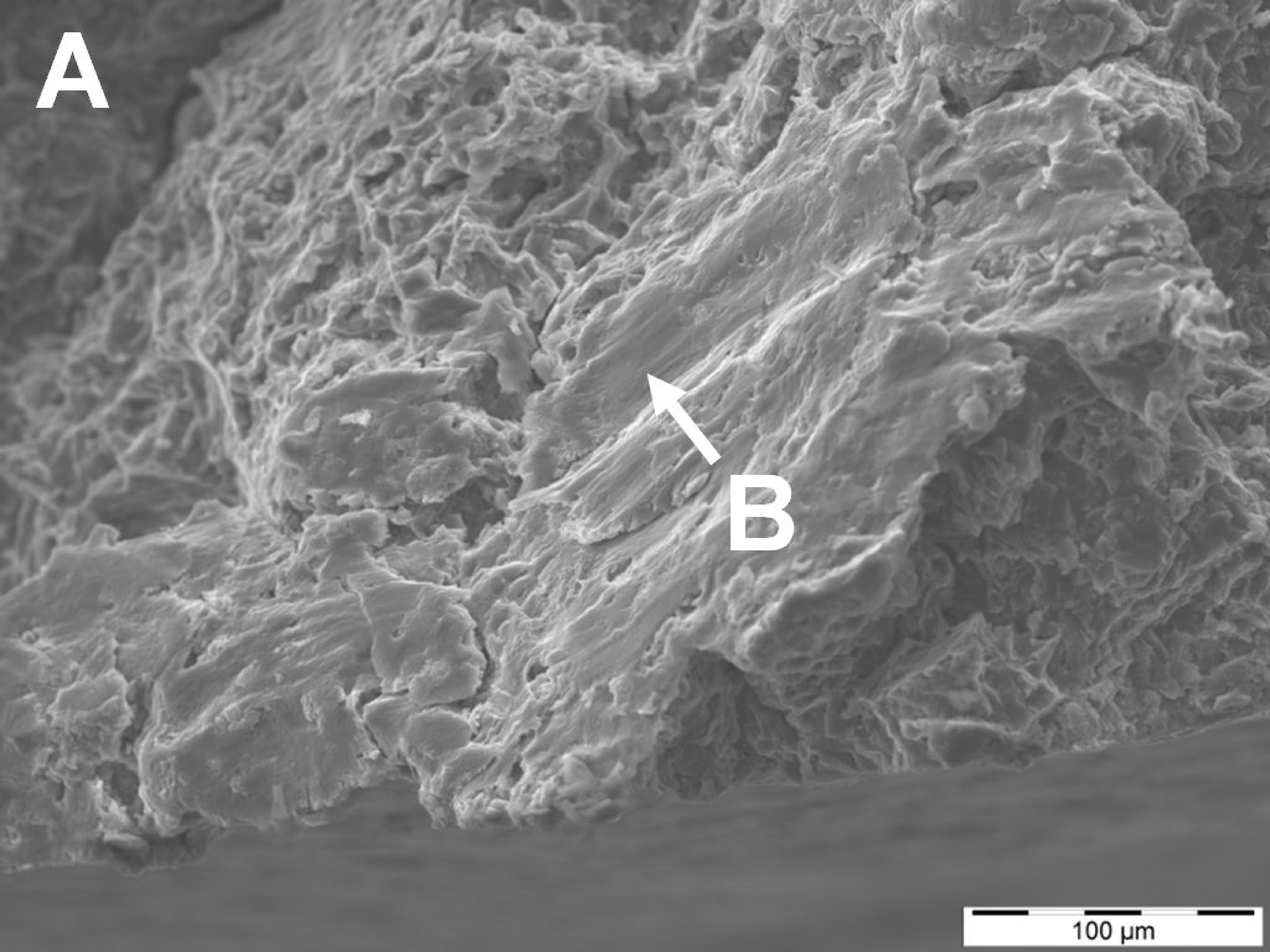
A
B
100 µm

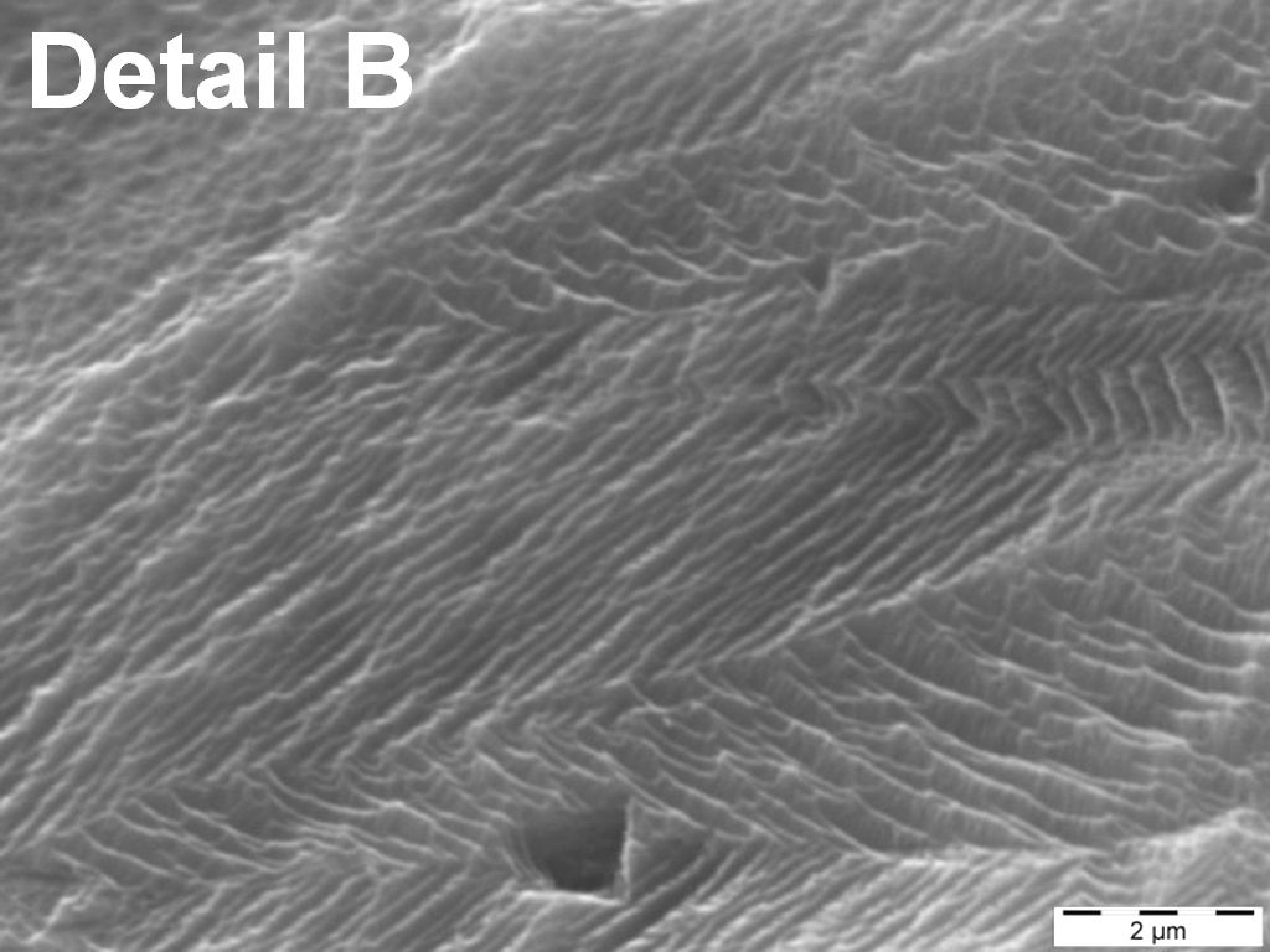
Detail B
2 µm

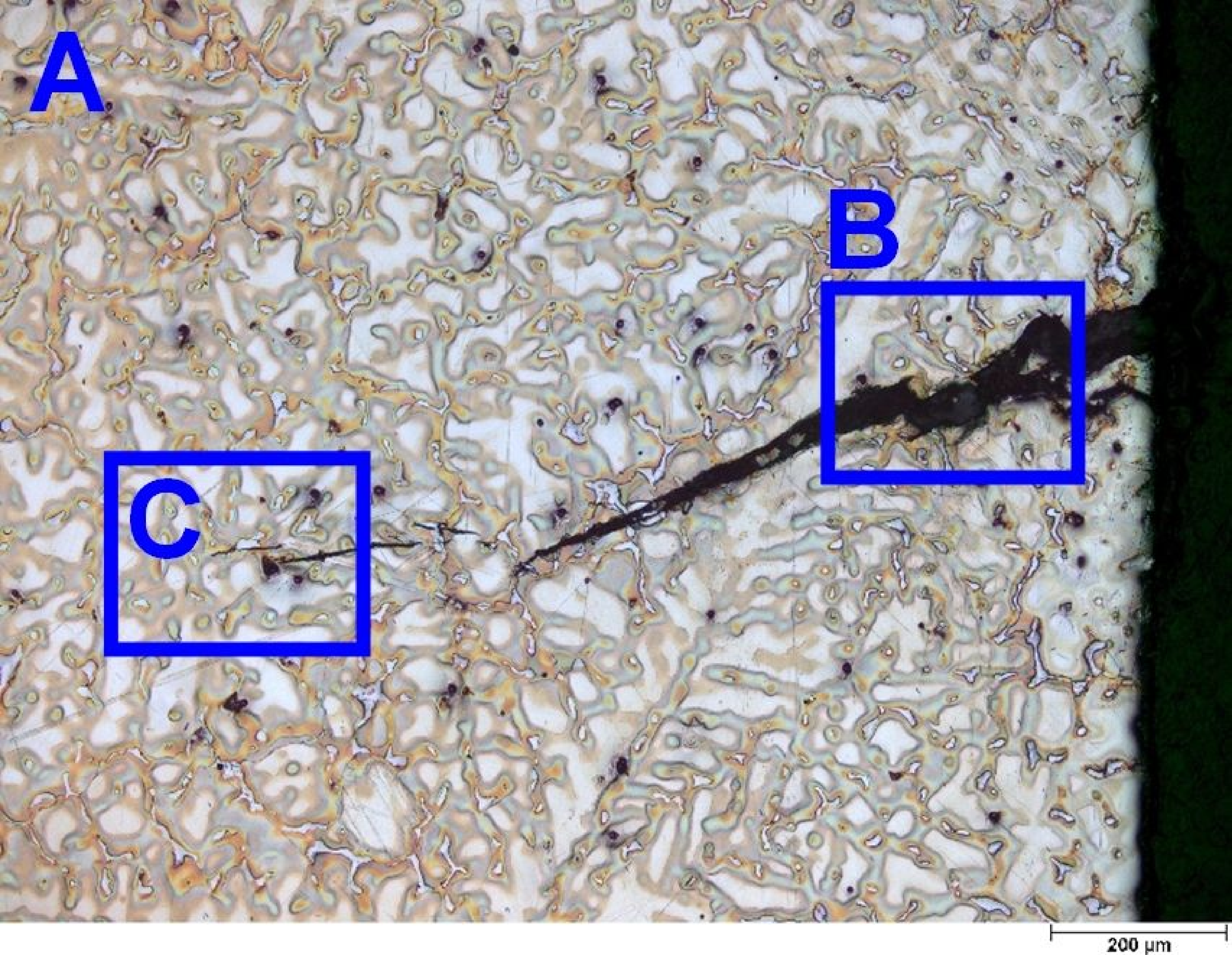
A
B
C
200 µm

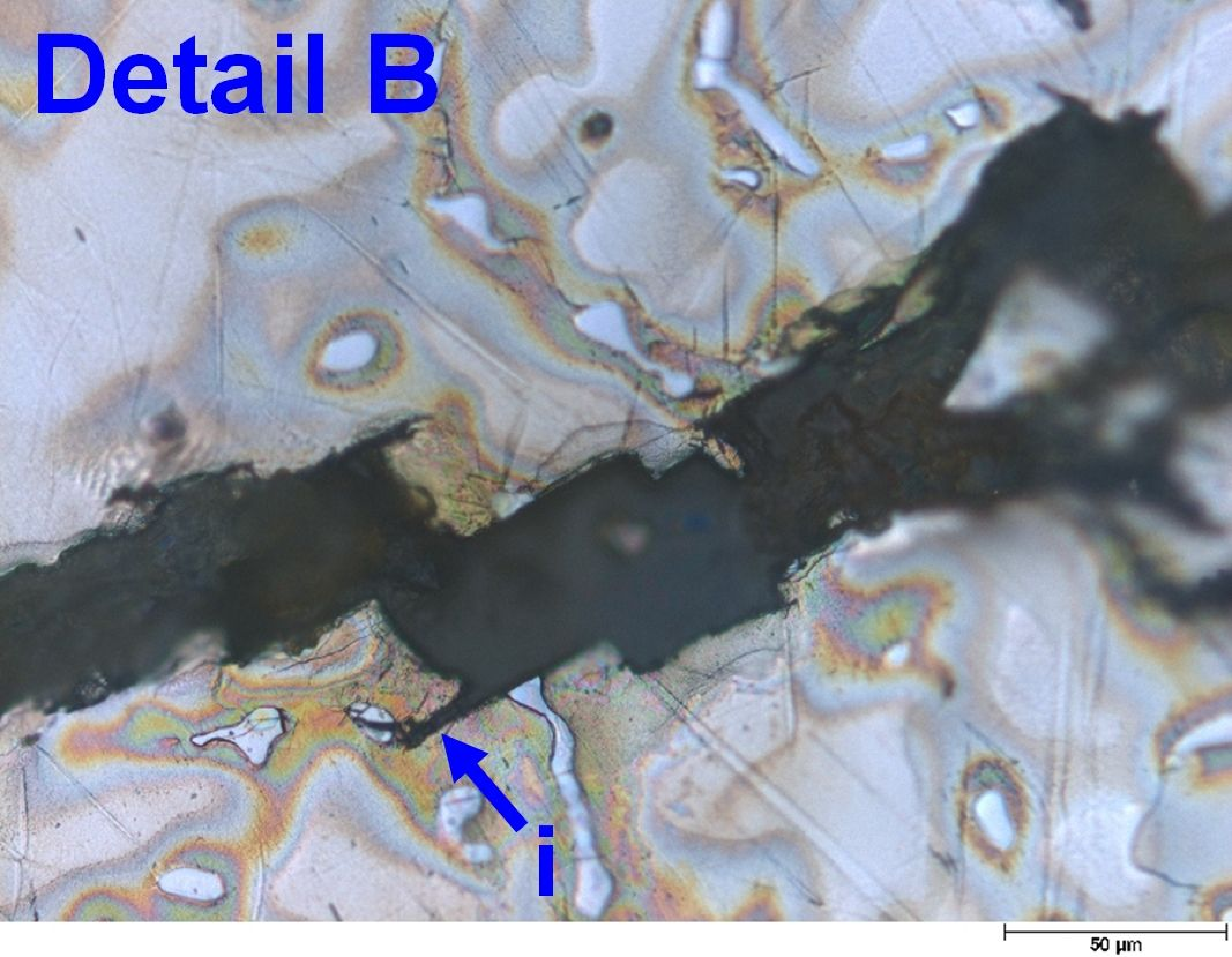
Detail B
i
50 µm

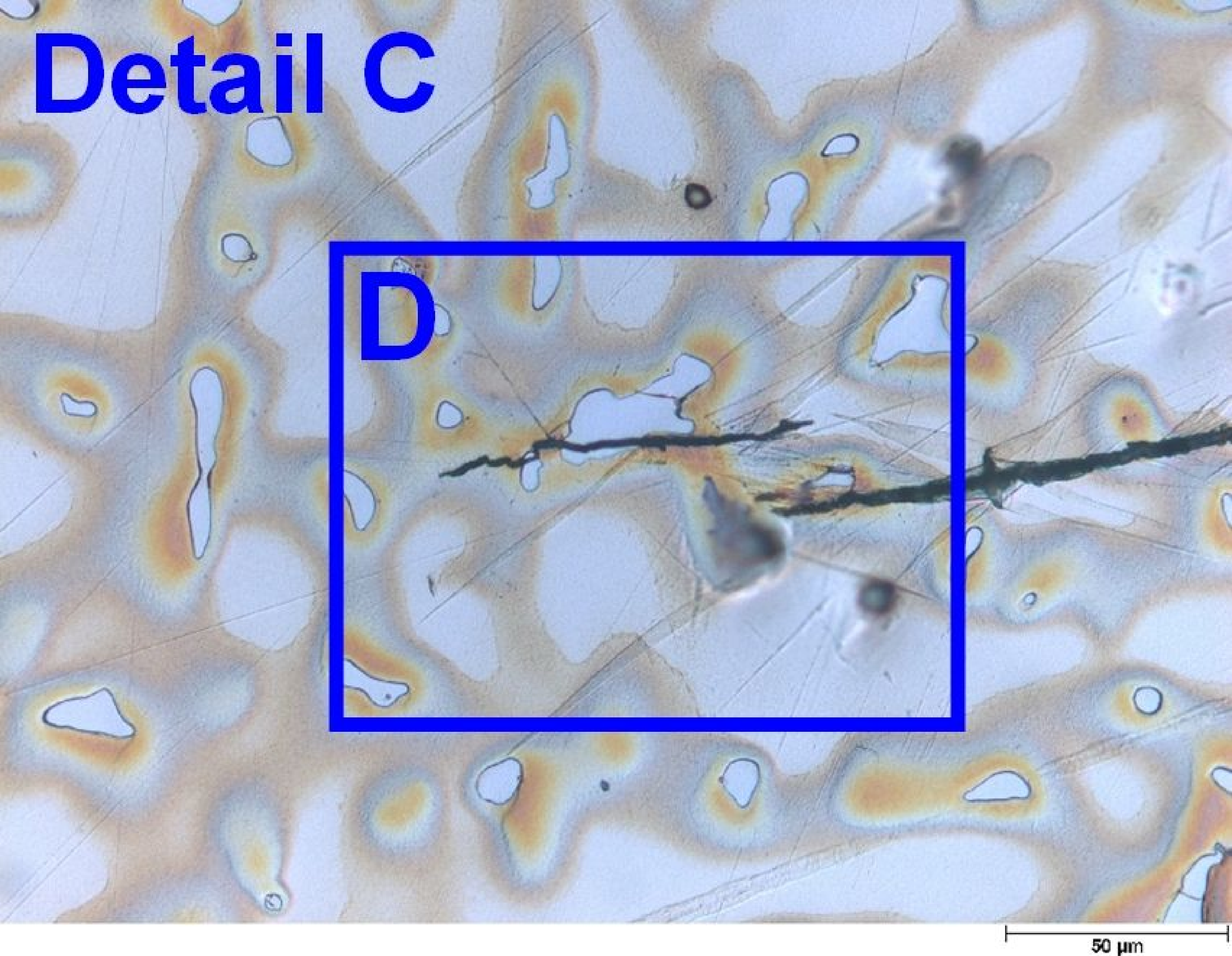
Detail C
D
50 µm

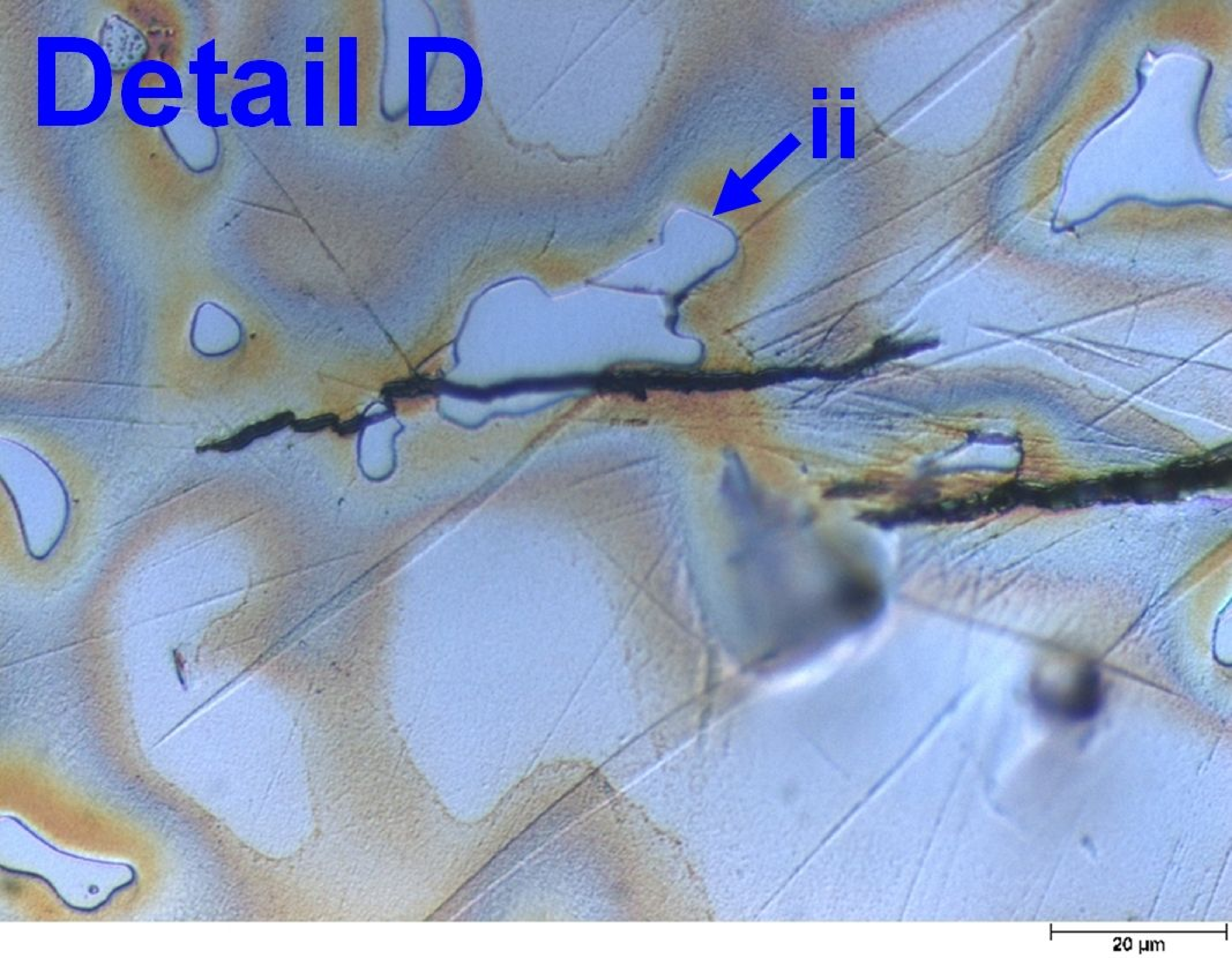
Detail D
ii
20 µm

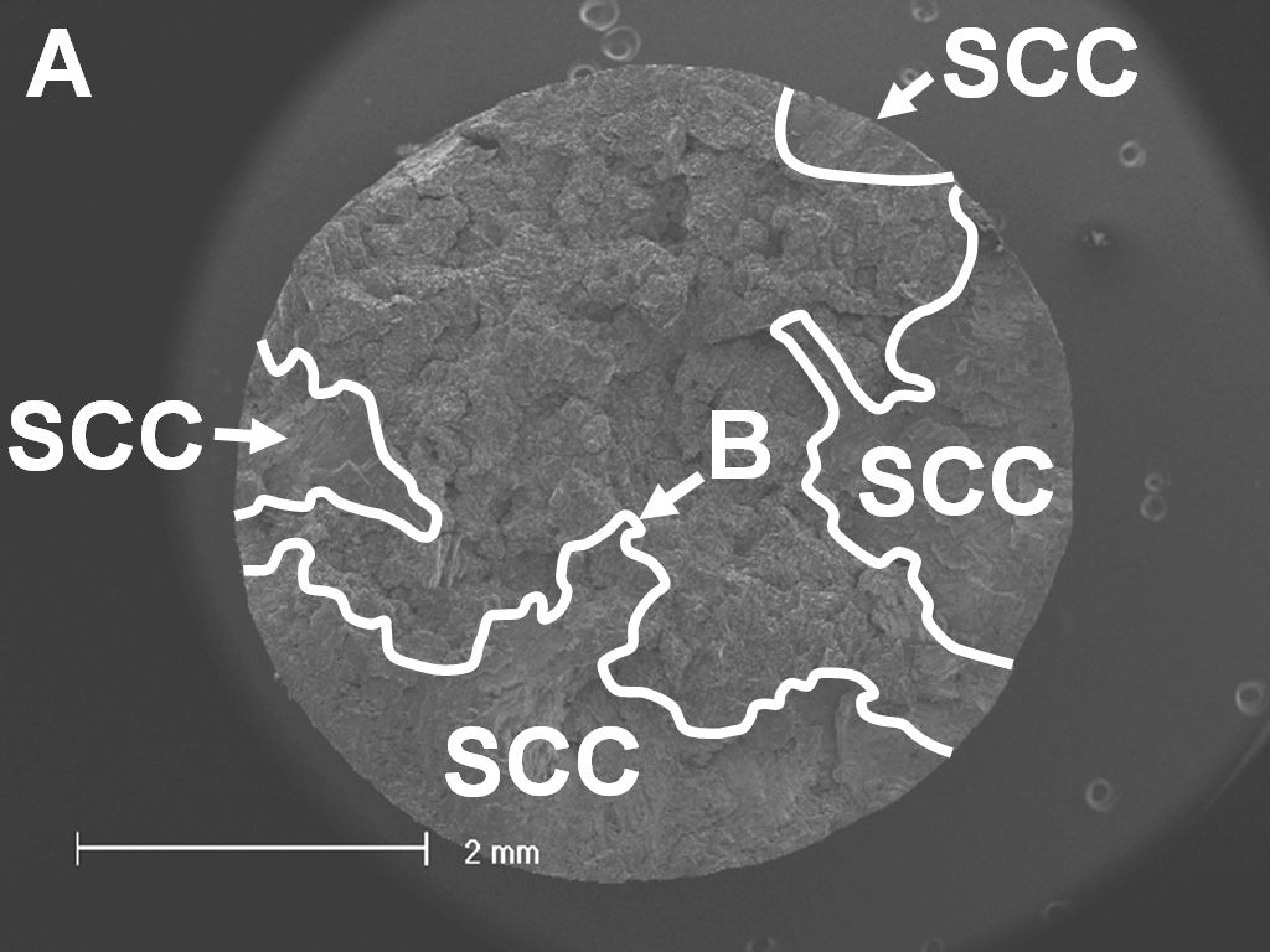
A
SCC
SCC
B
SCC
SCC
2 mm

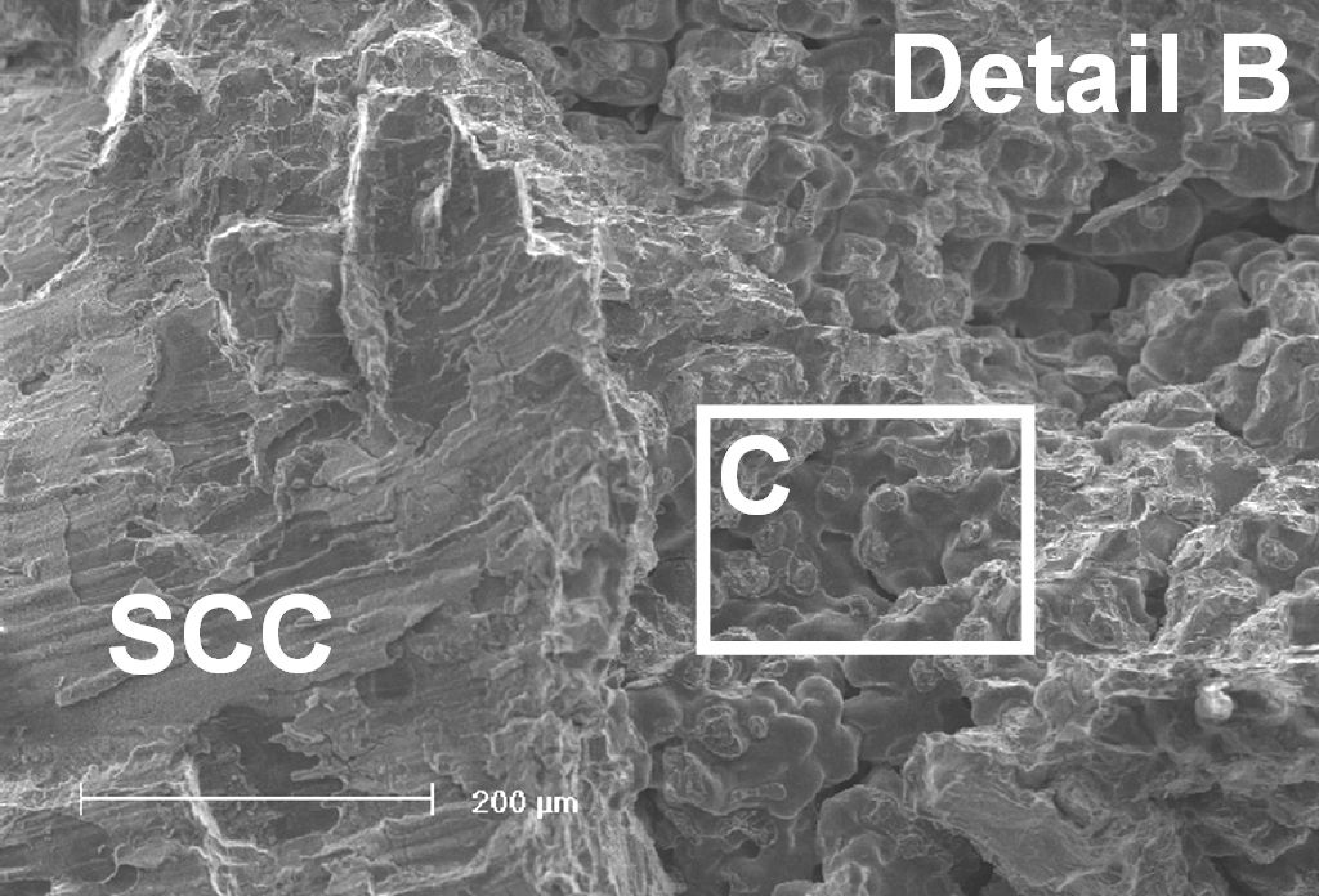
Detail B
C
SCC
200 µm

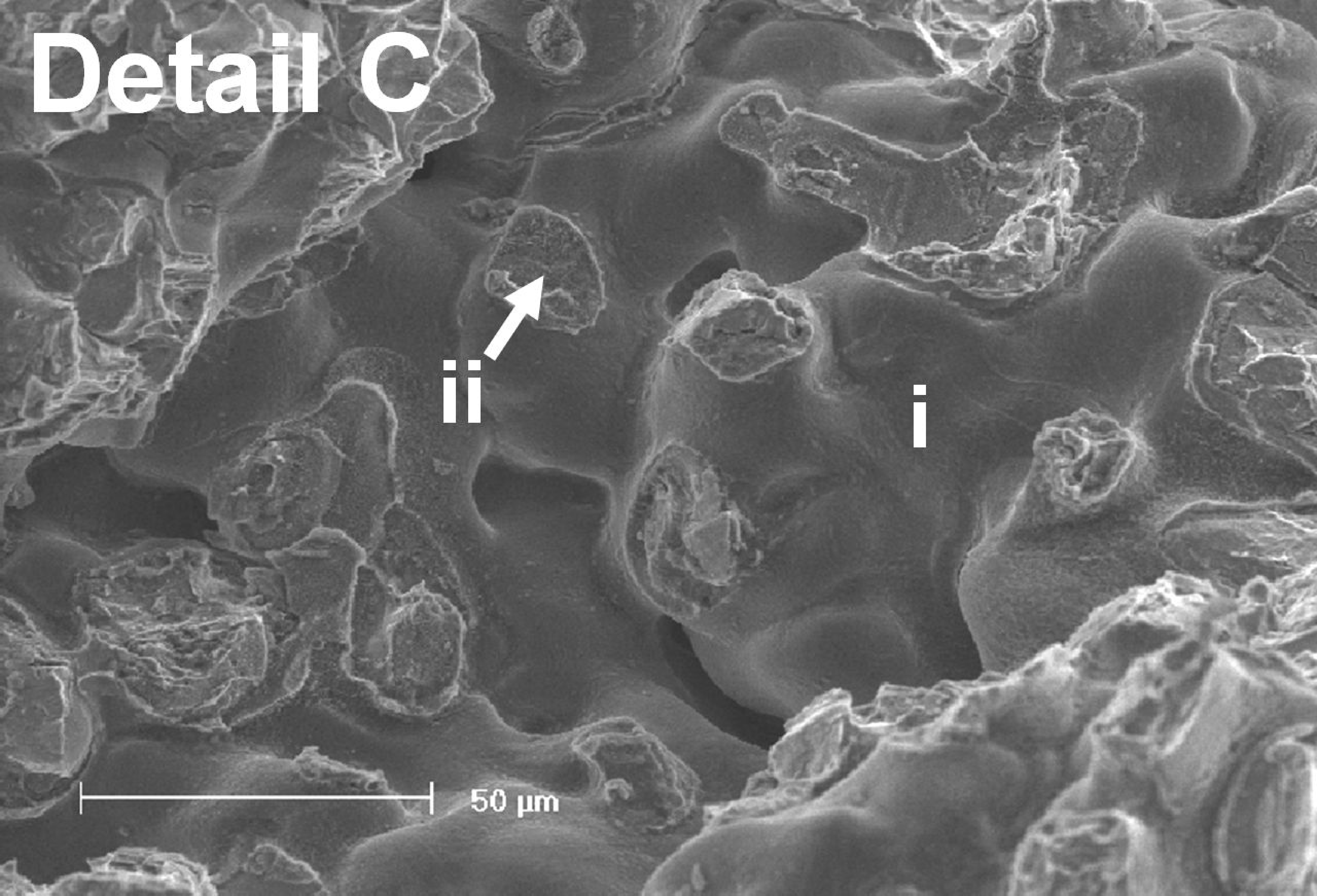
Detail C
ii
i
50 µm

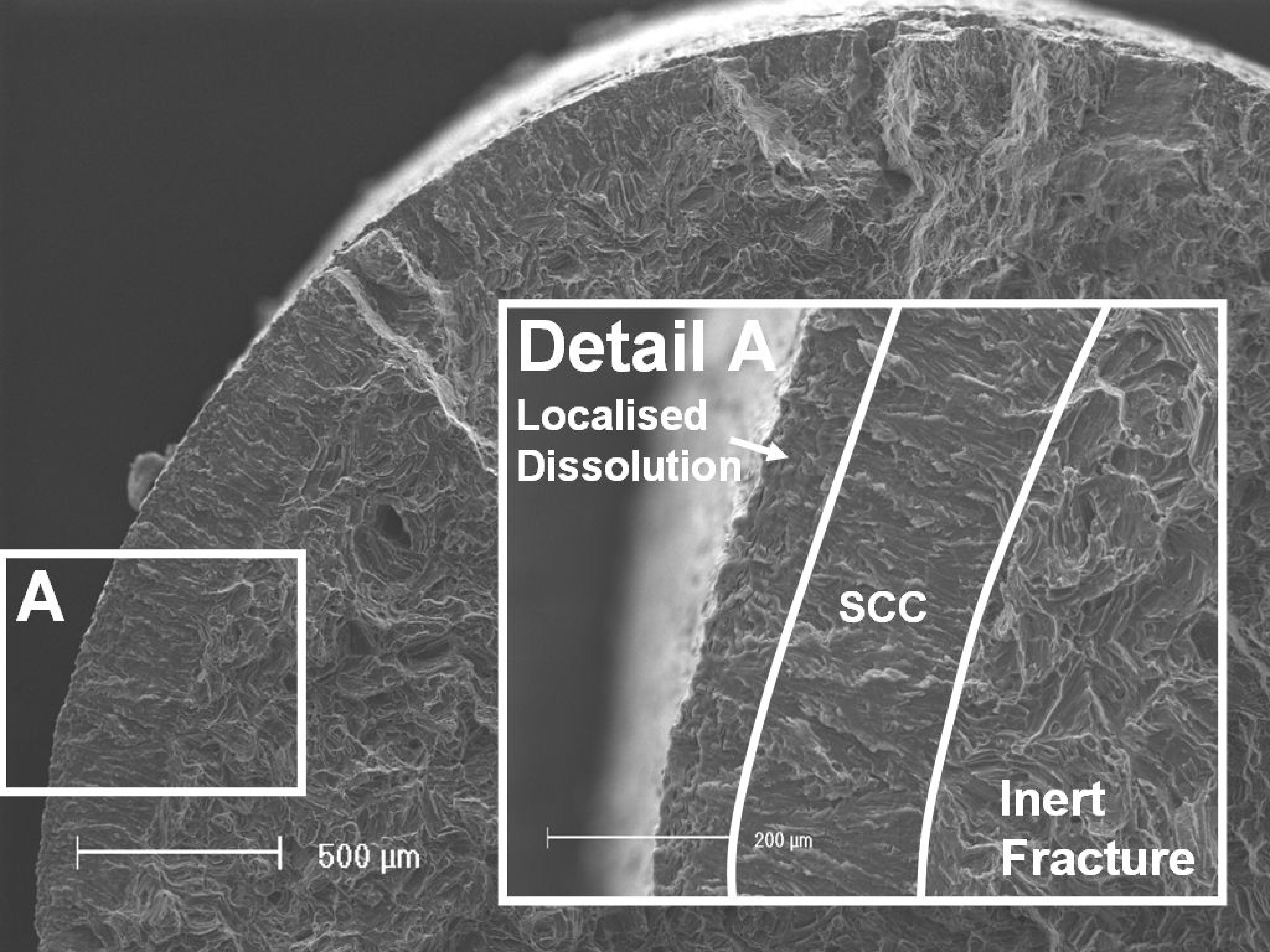
Detail A
Localised Dissolution
SCC
Inert Fracture
200 µm
A
500 µm

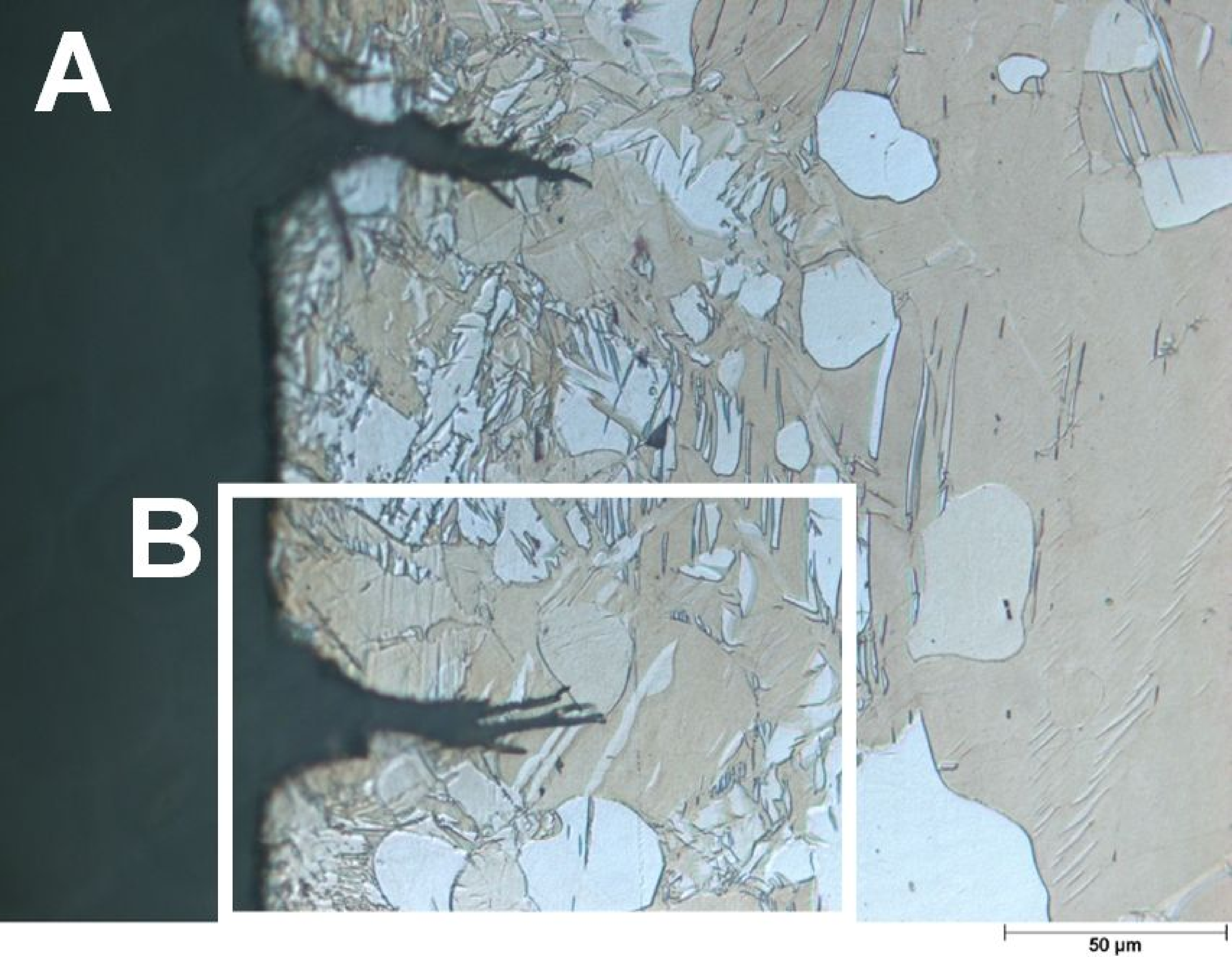
A
B
50 µm

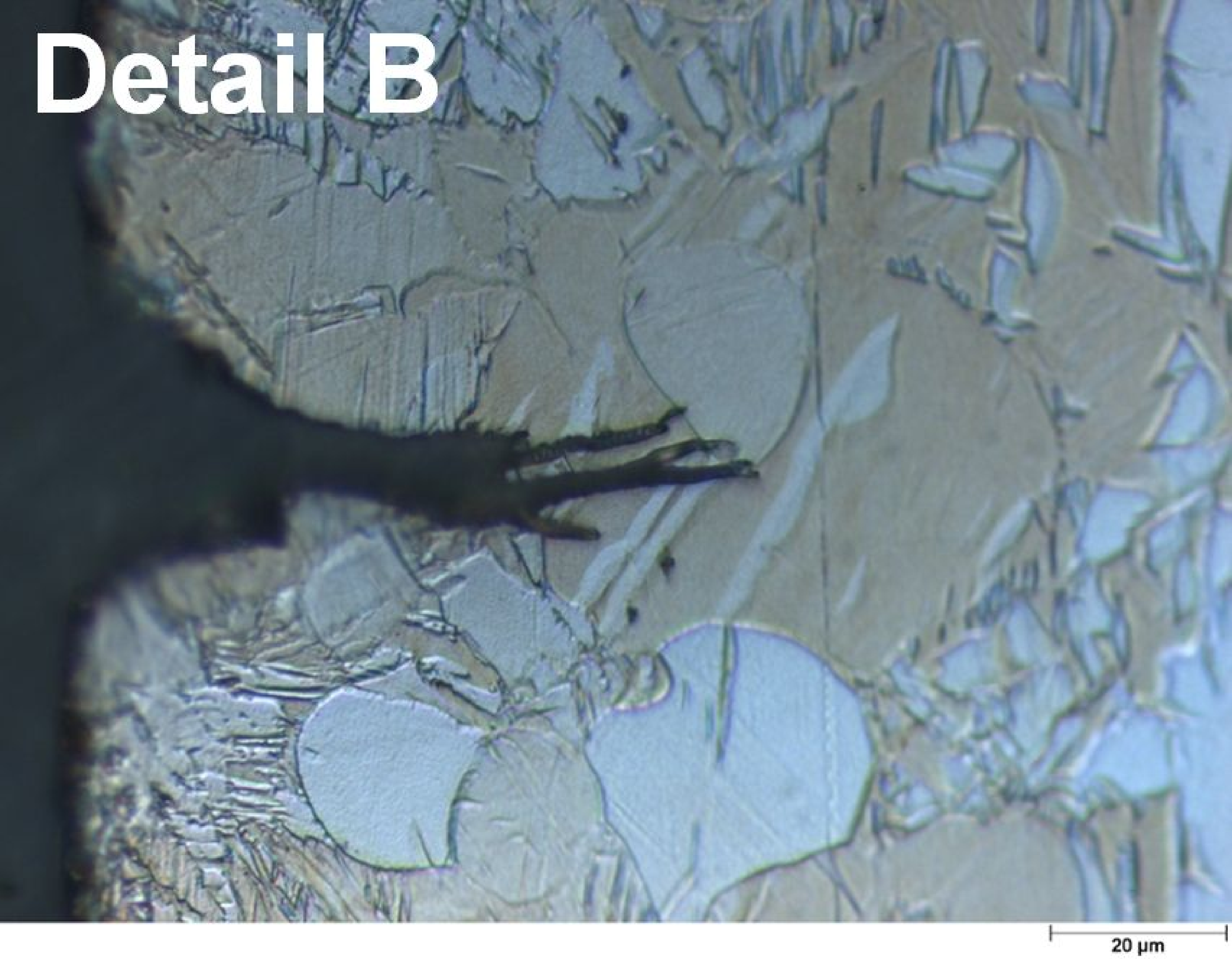
Detail B
20 µm

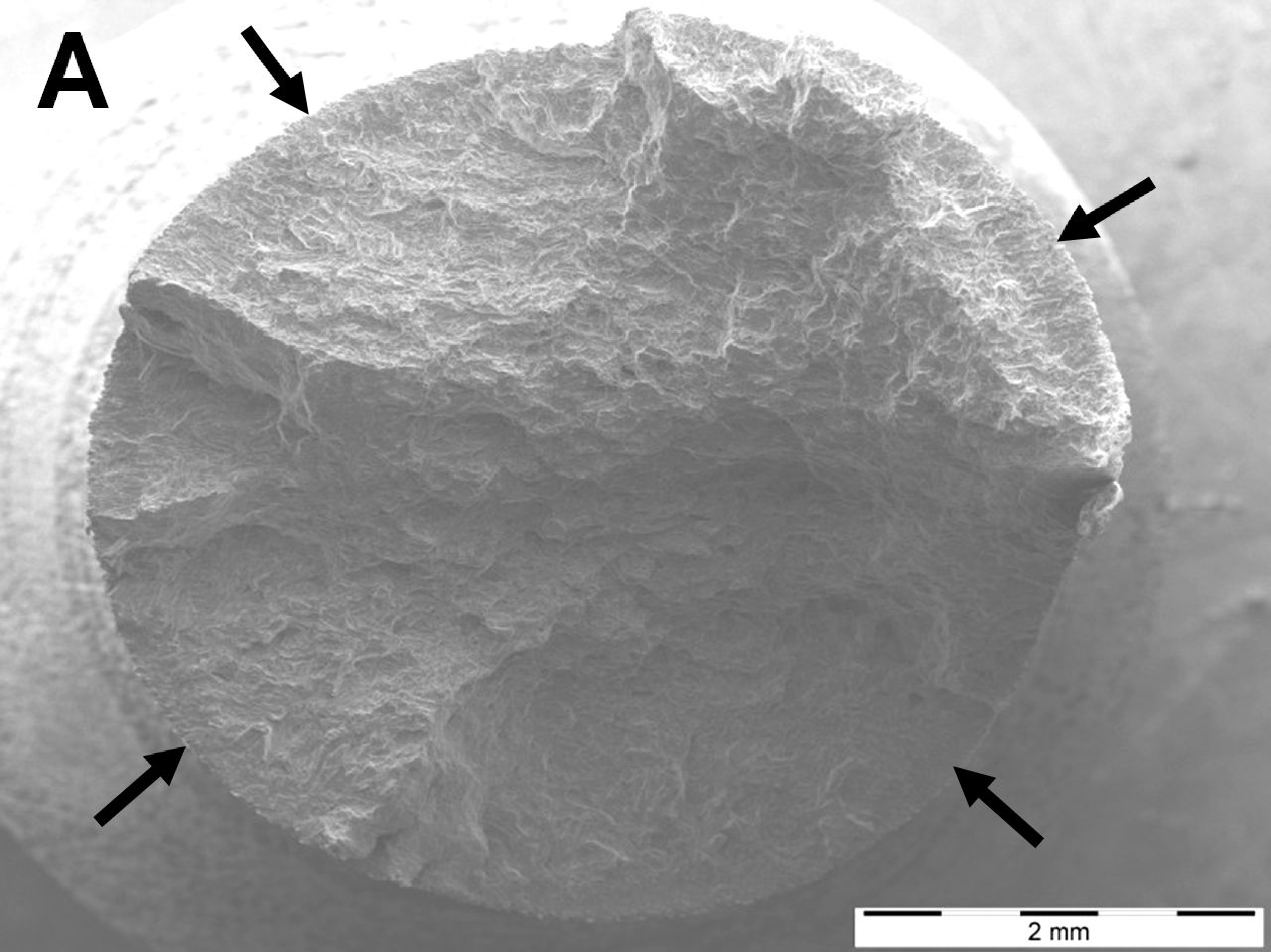
A
2 mm

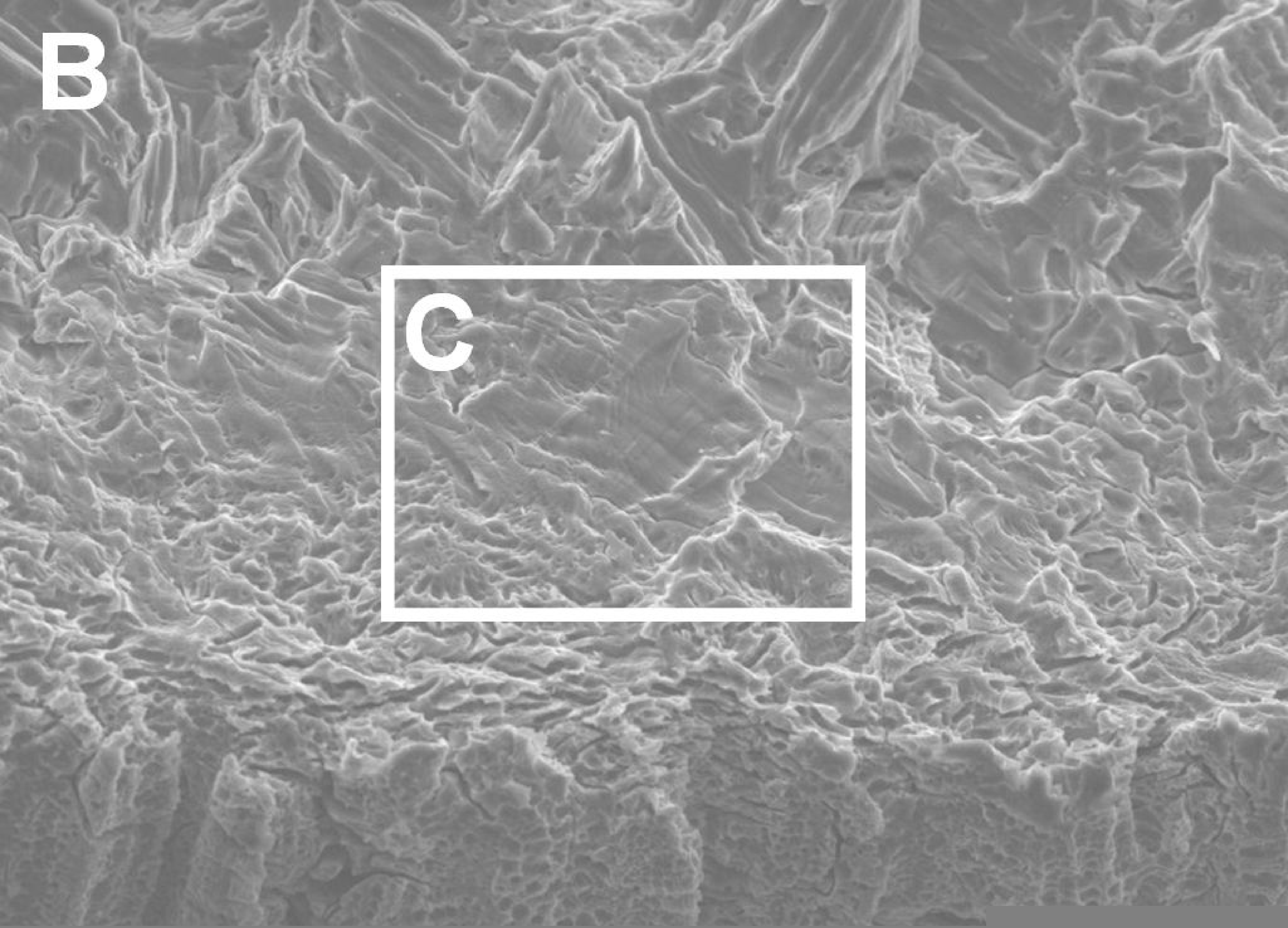
B
C

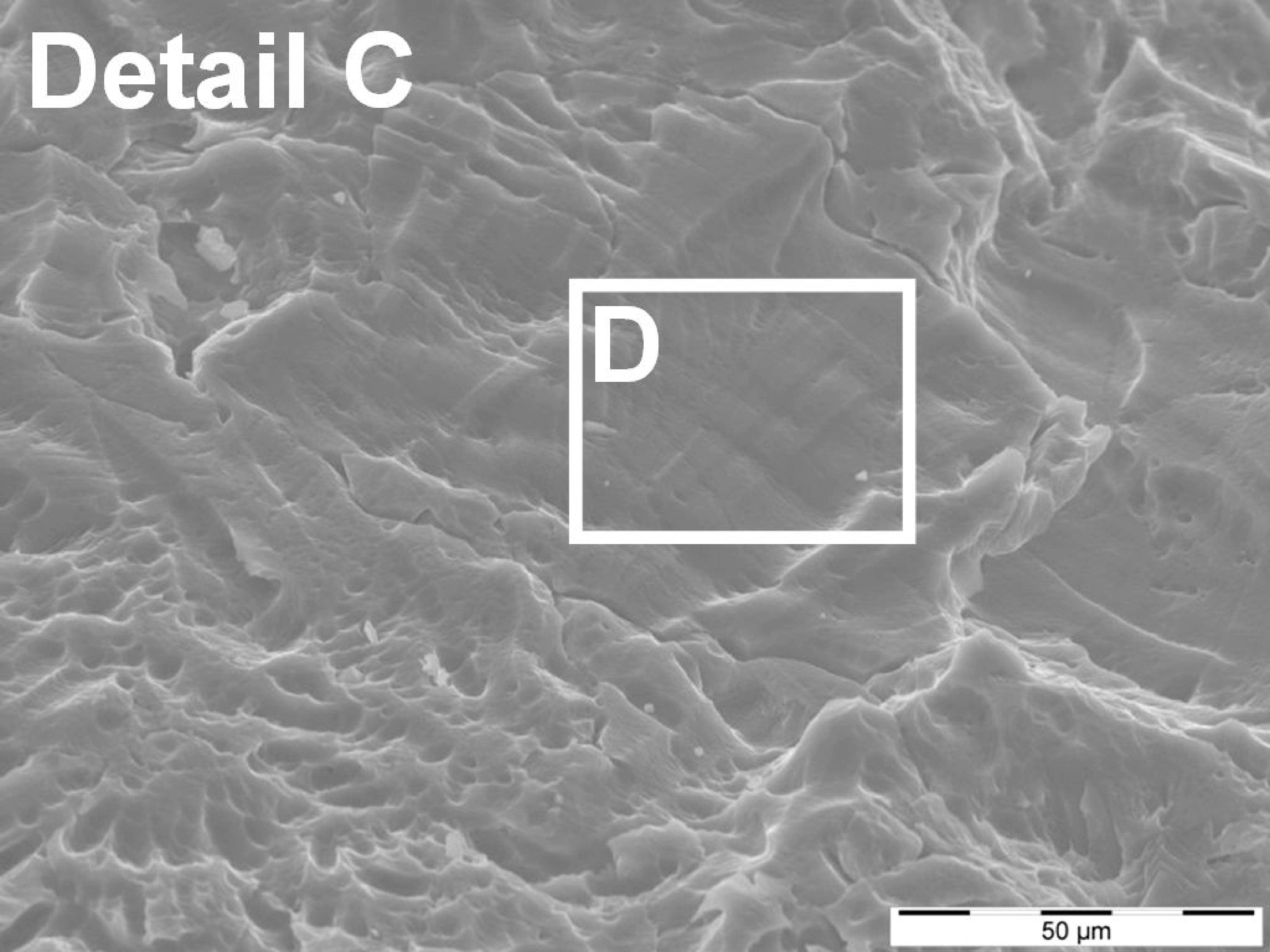
Detail C
D
50 µm

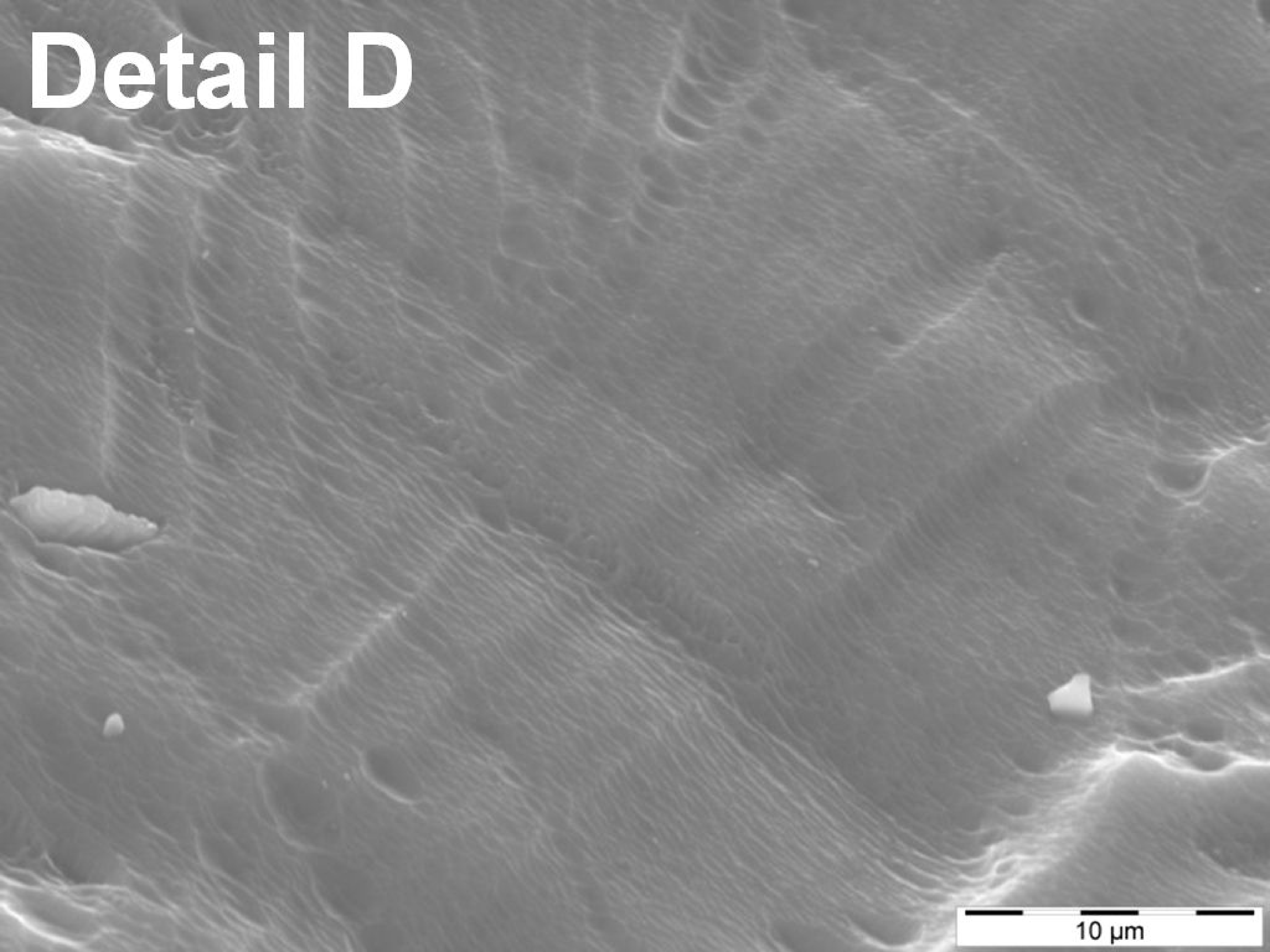
Detail D
10 µm

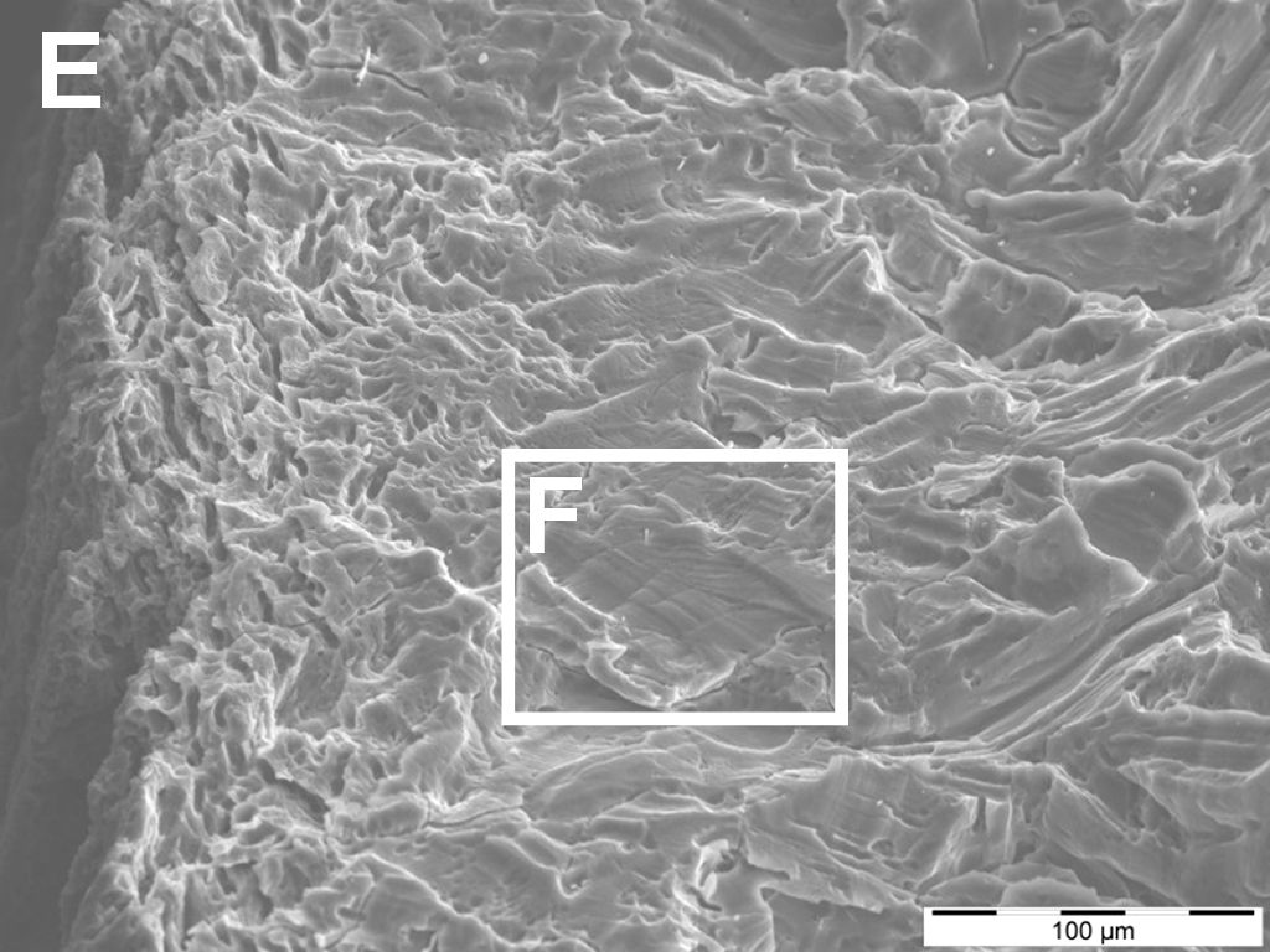
E
F
100 µm

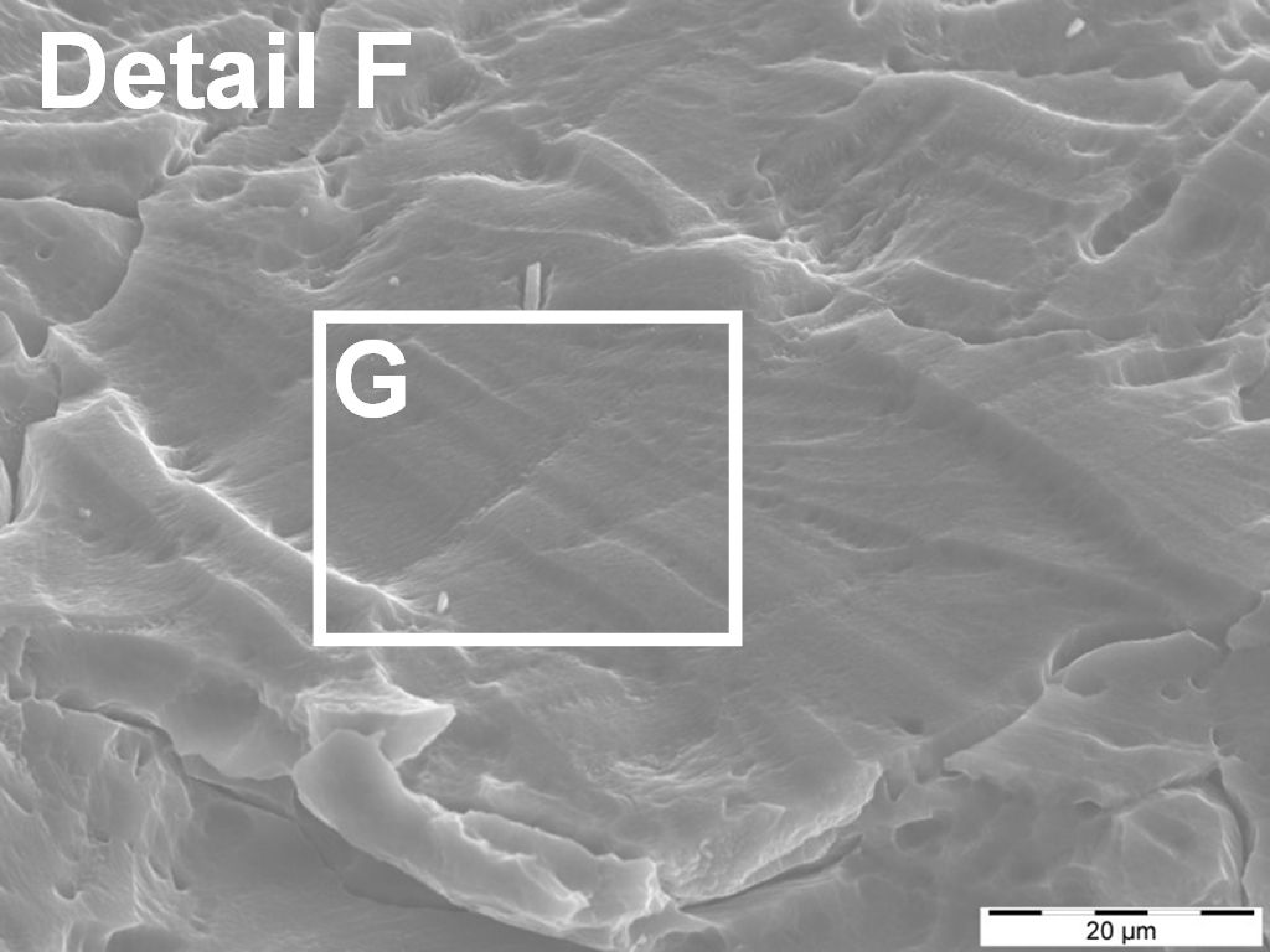
Detail F
G
20 µm

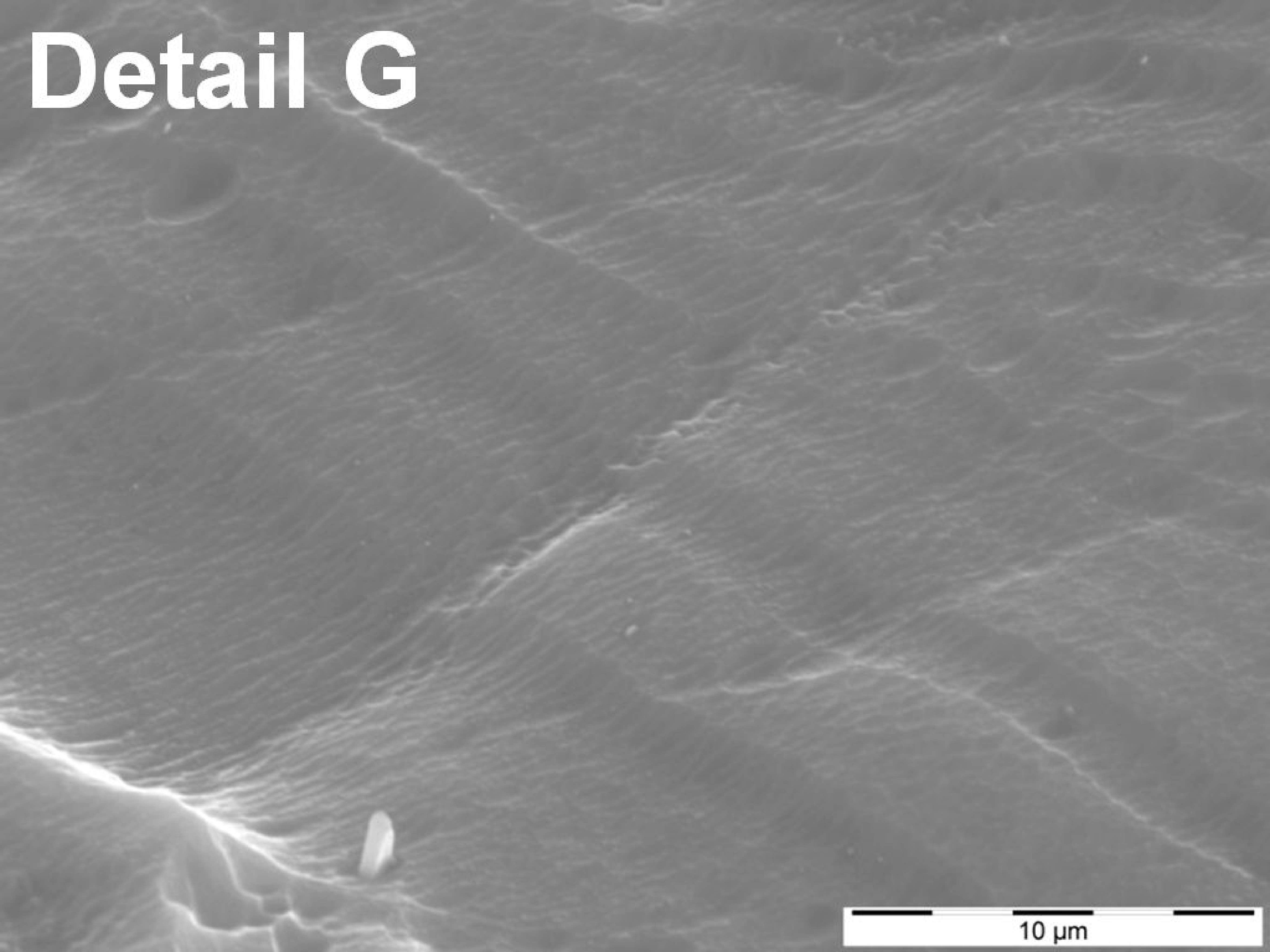
Detail G
10 µm

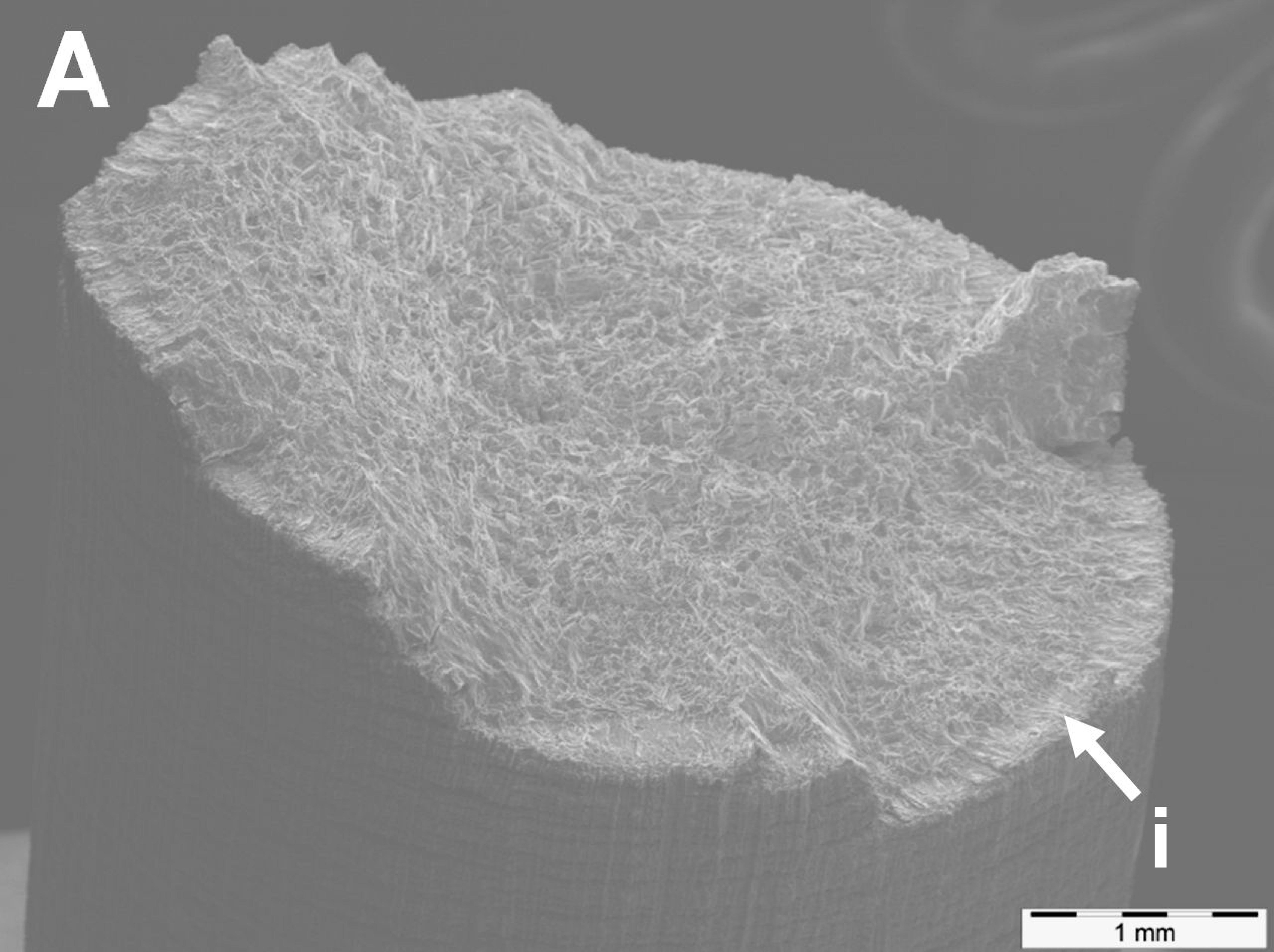
A
i
1 mm

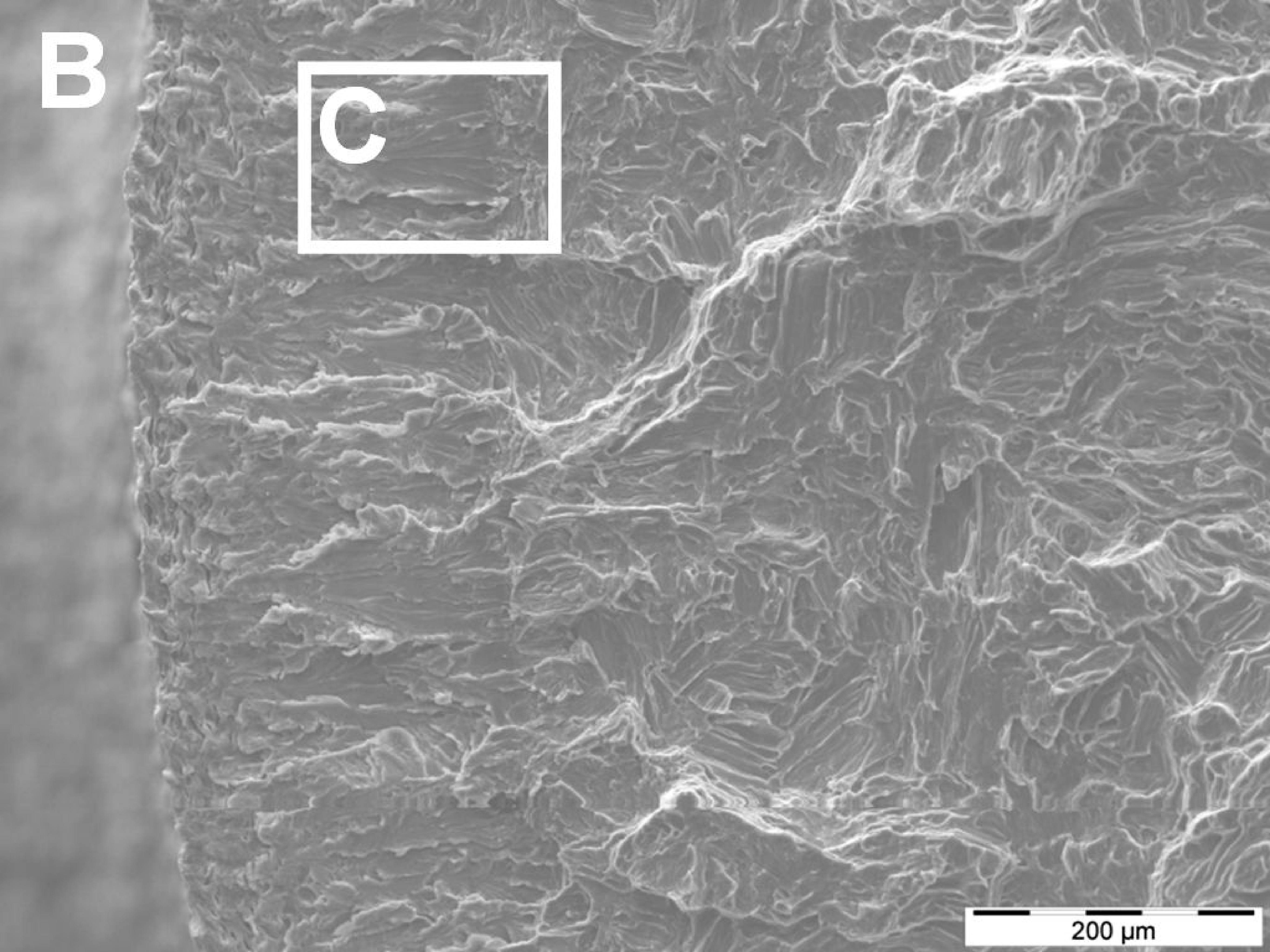
B
C
200 µm

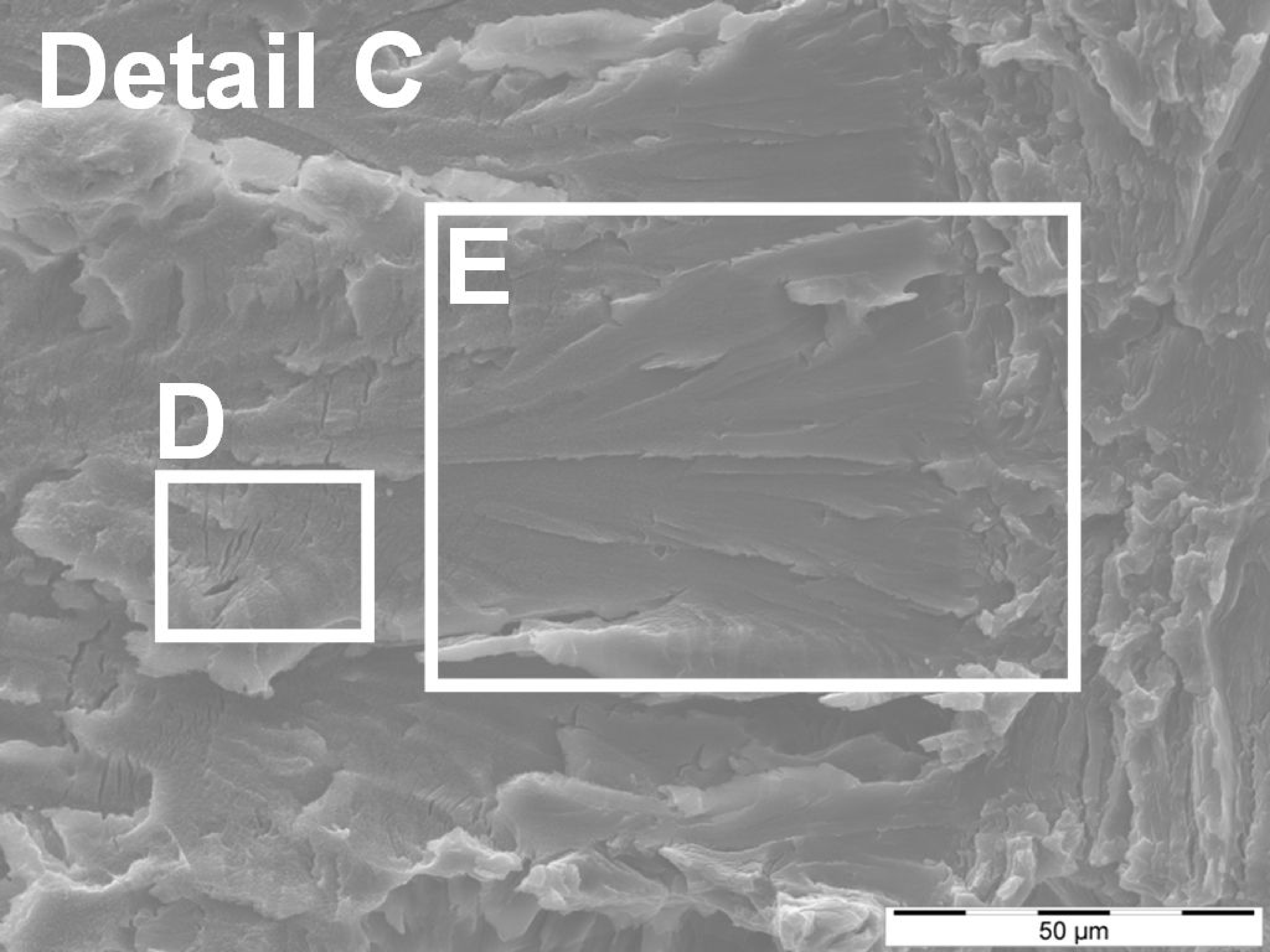
Detail C
E
D
50 µm

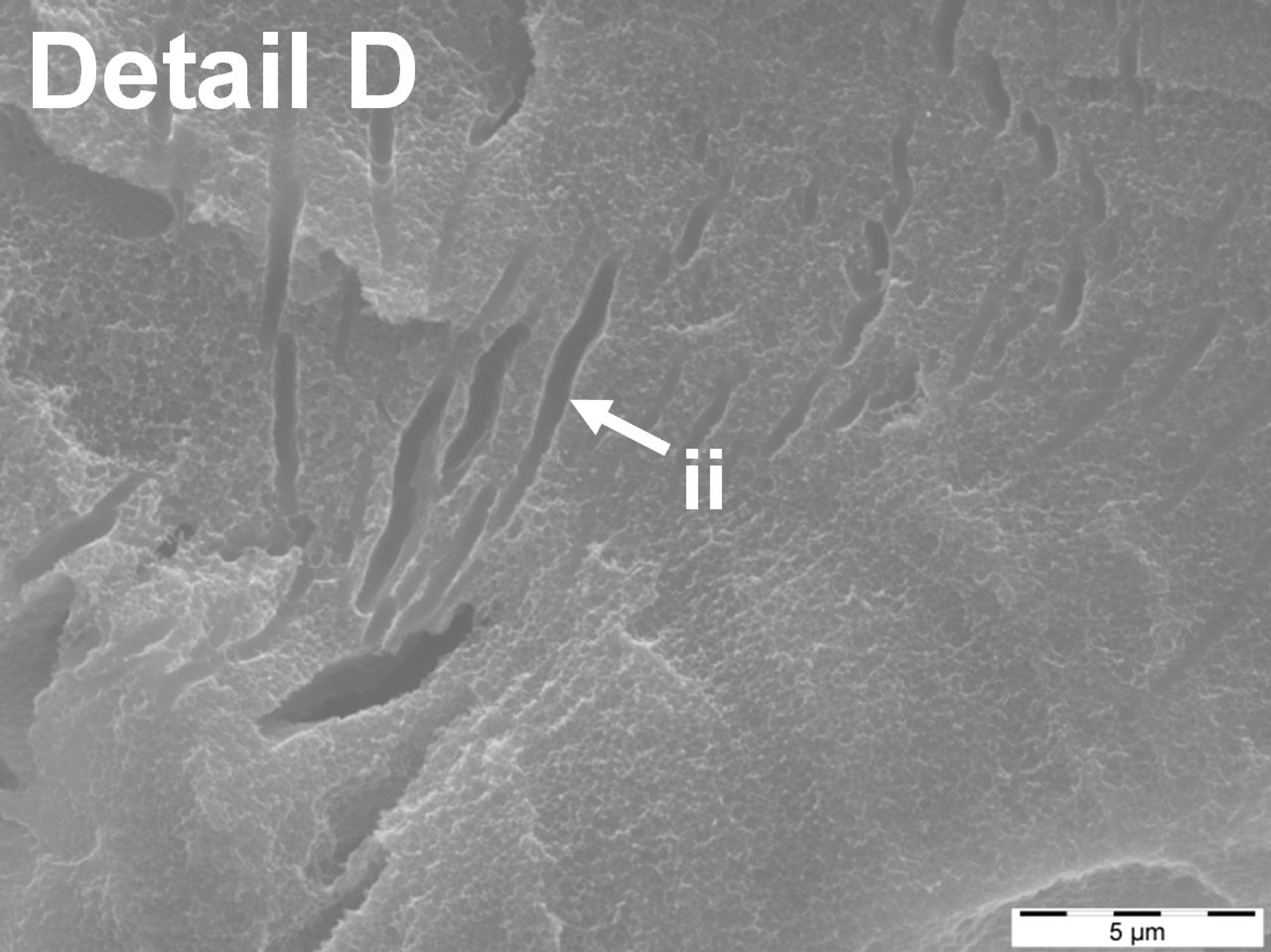
Detail D
ii
5 µm

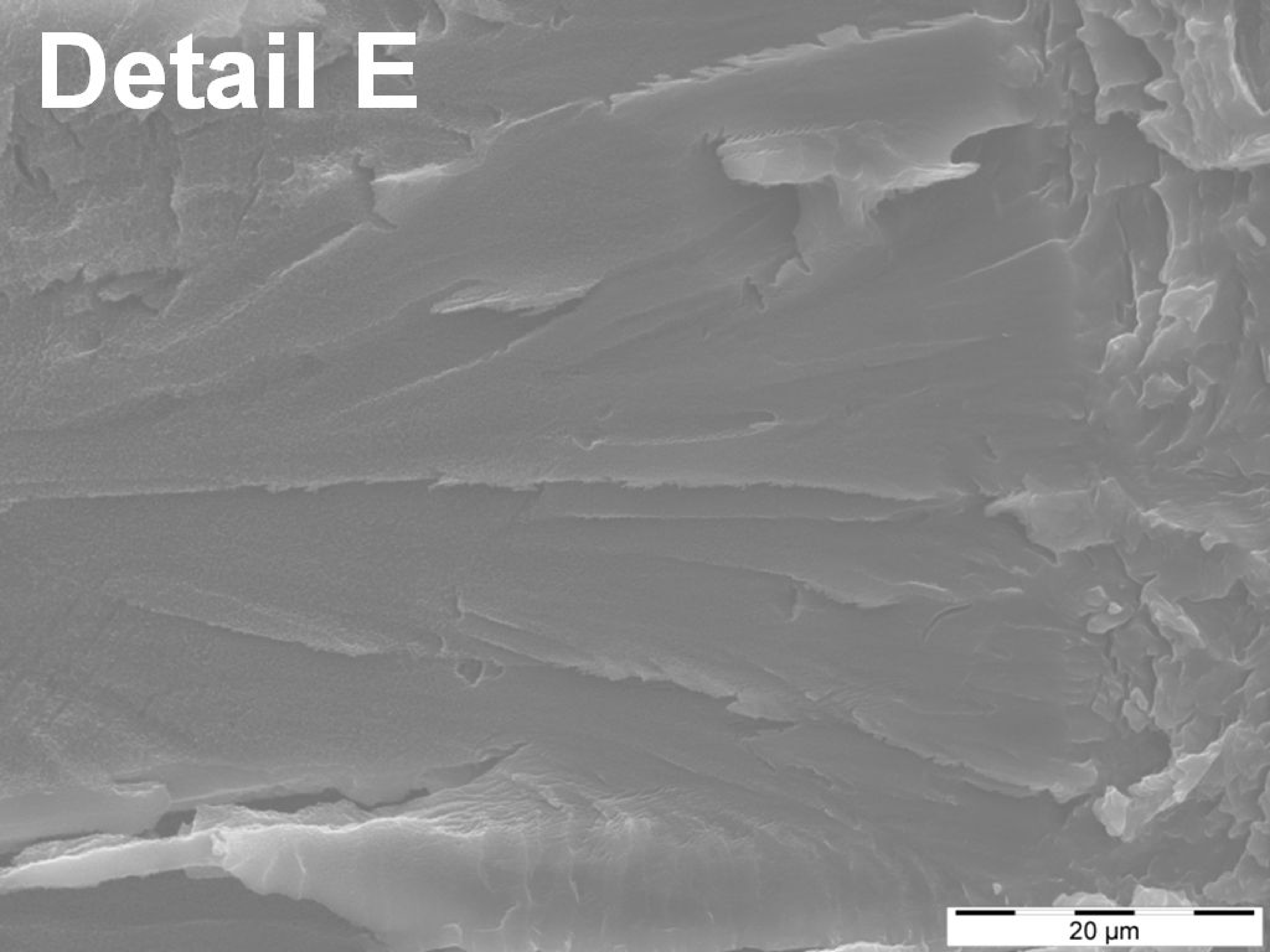
Detail E
20 µm

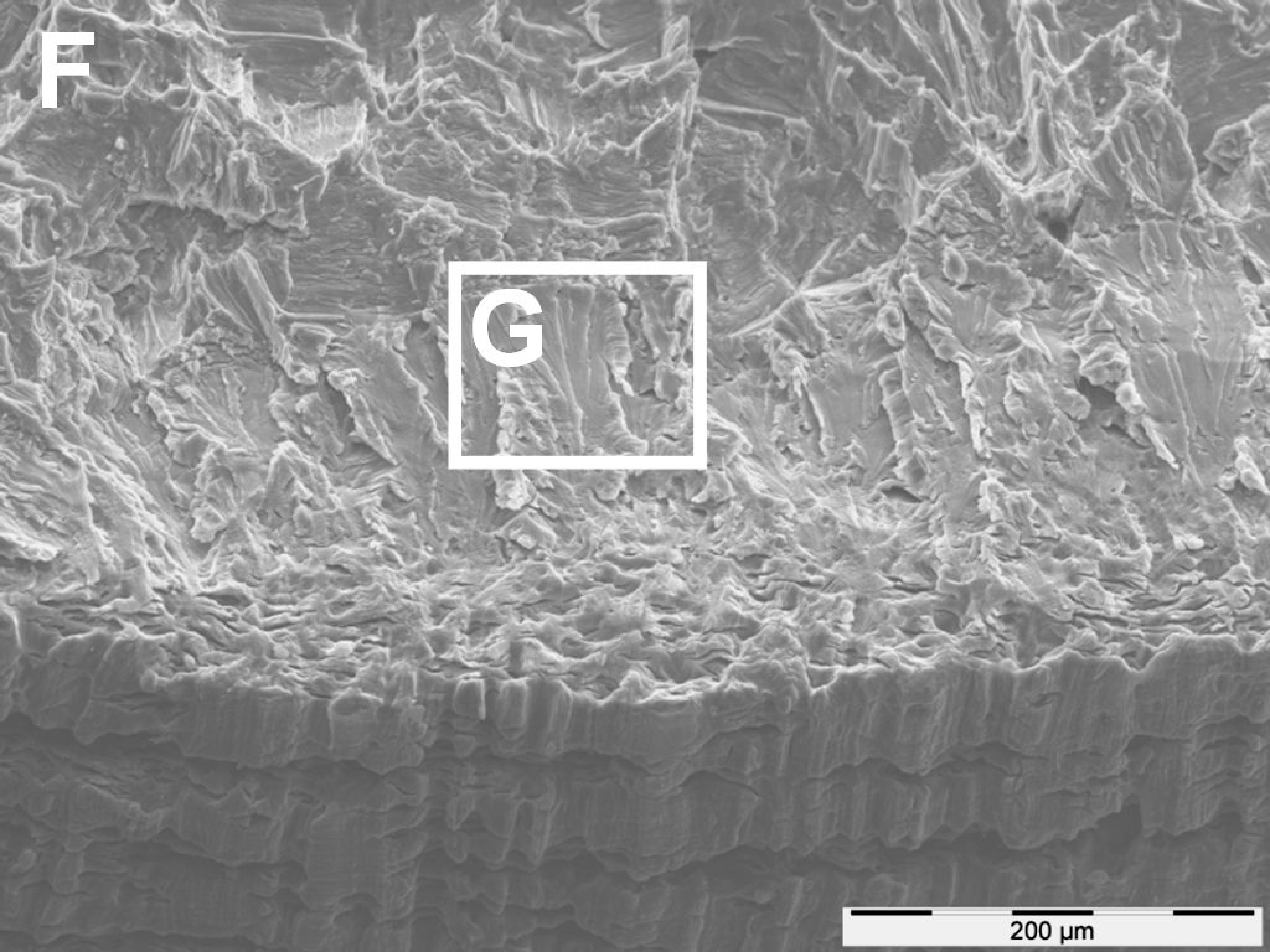

F
G
200 µm

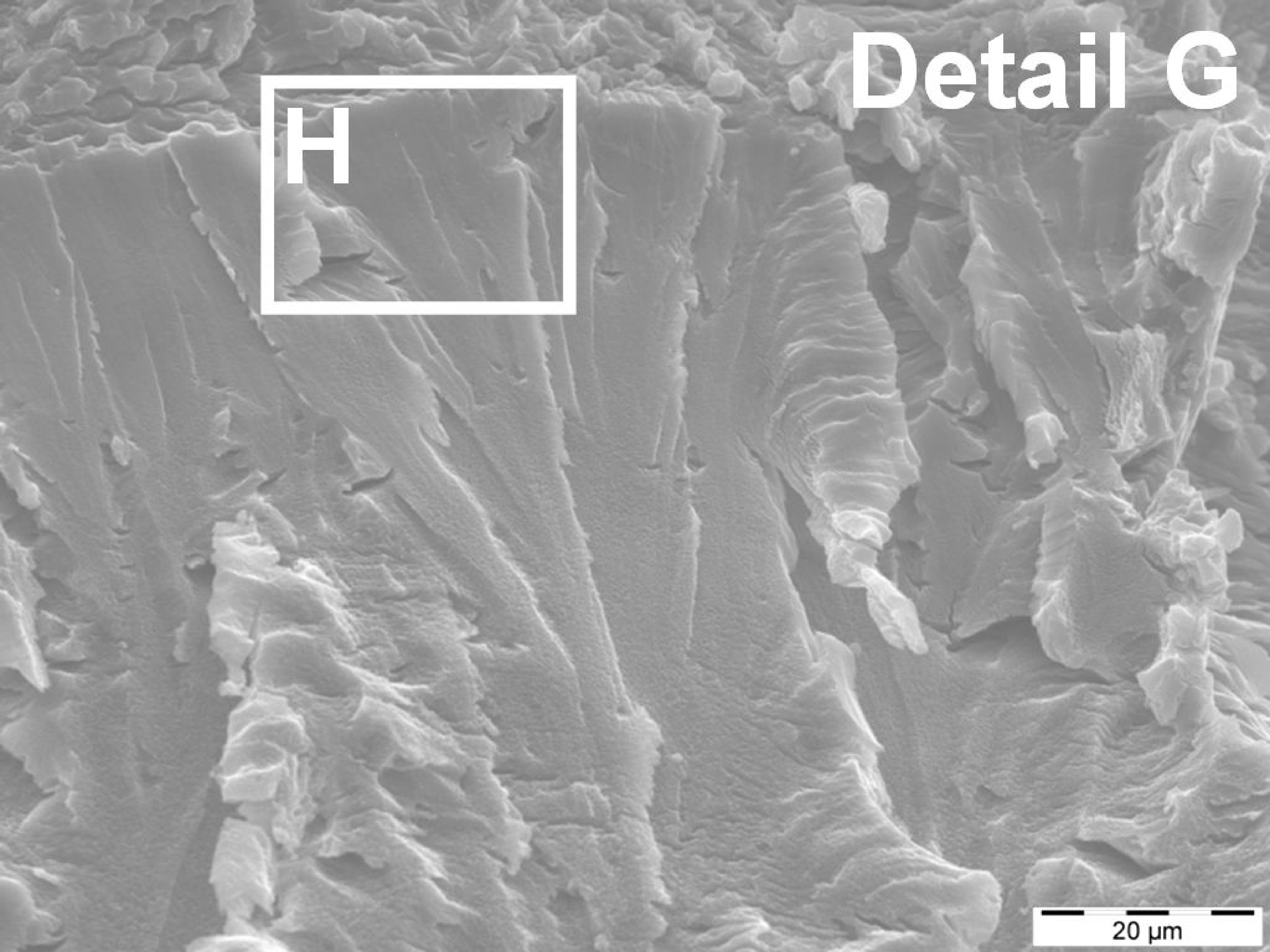
Detail G
H
20 µm

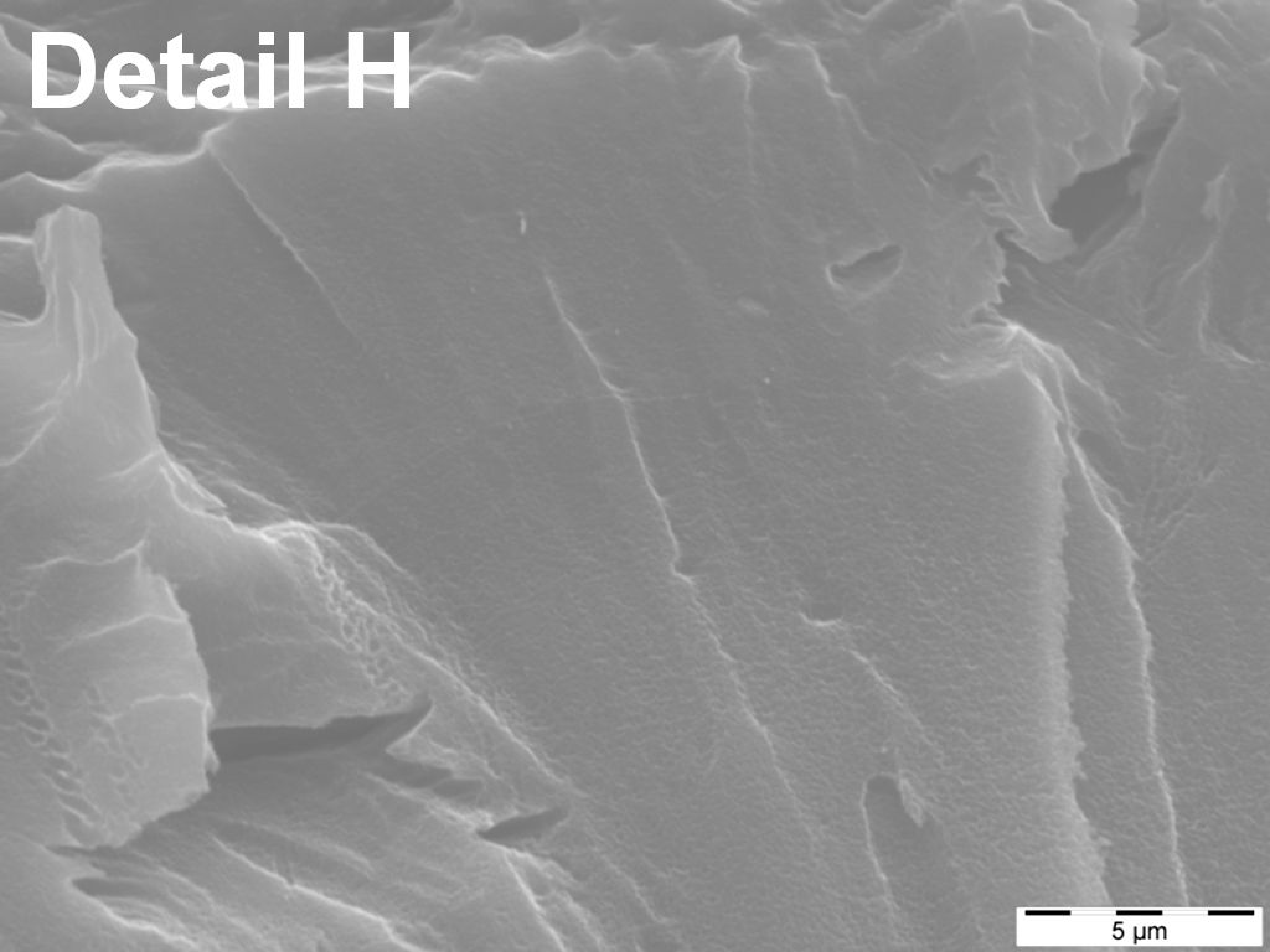

Detail H

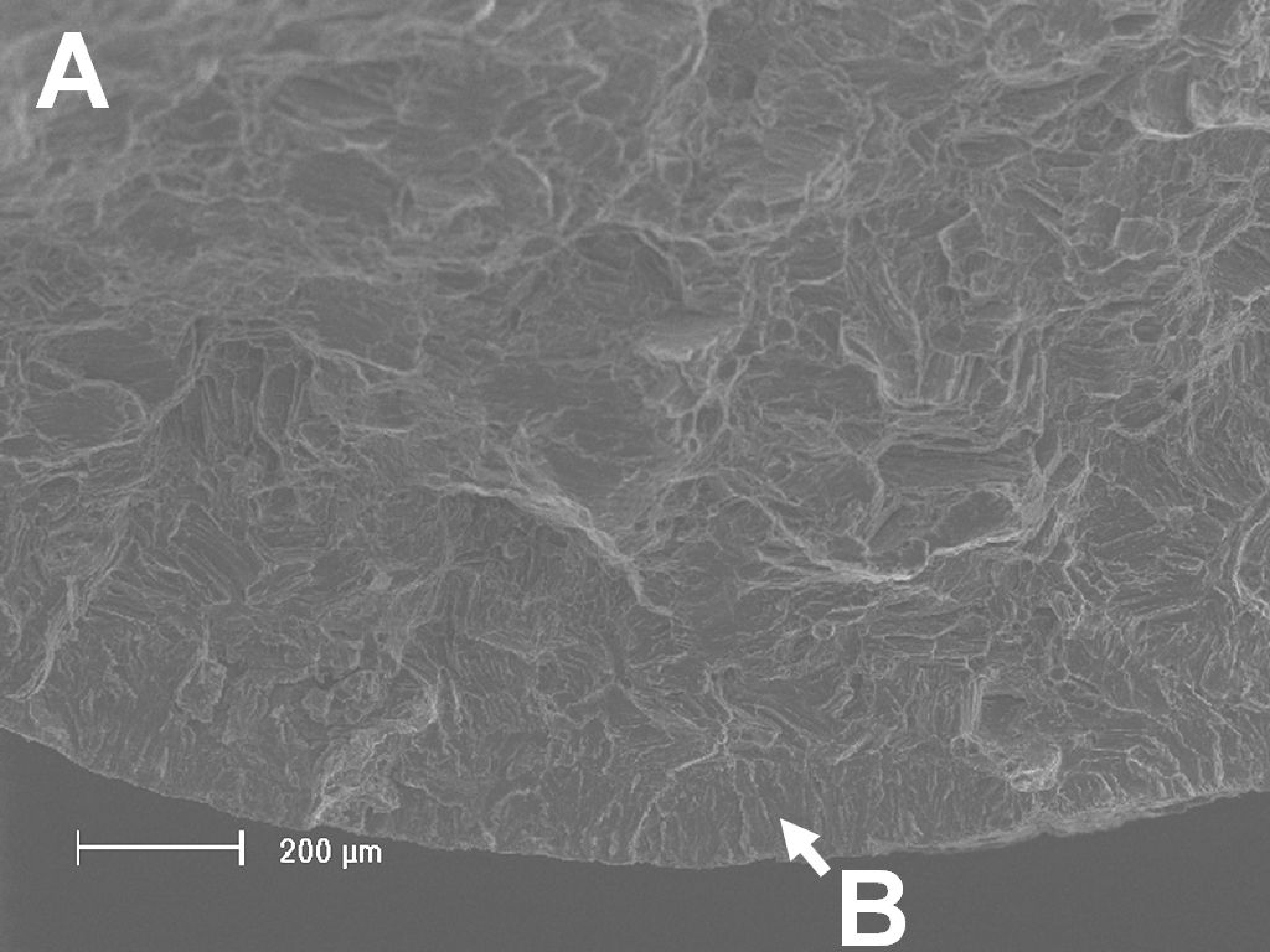
A
200 µm
B

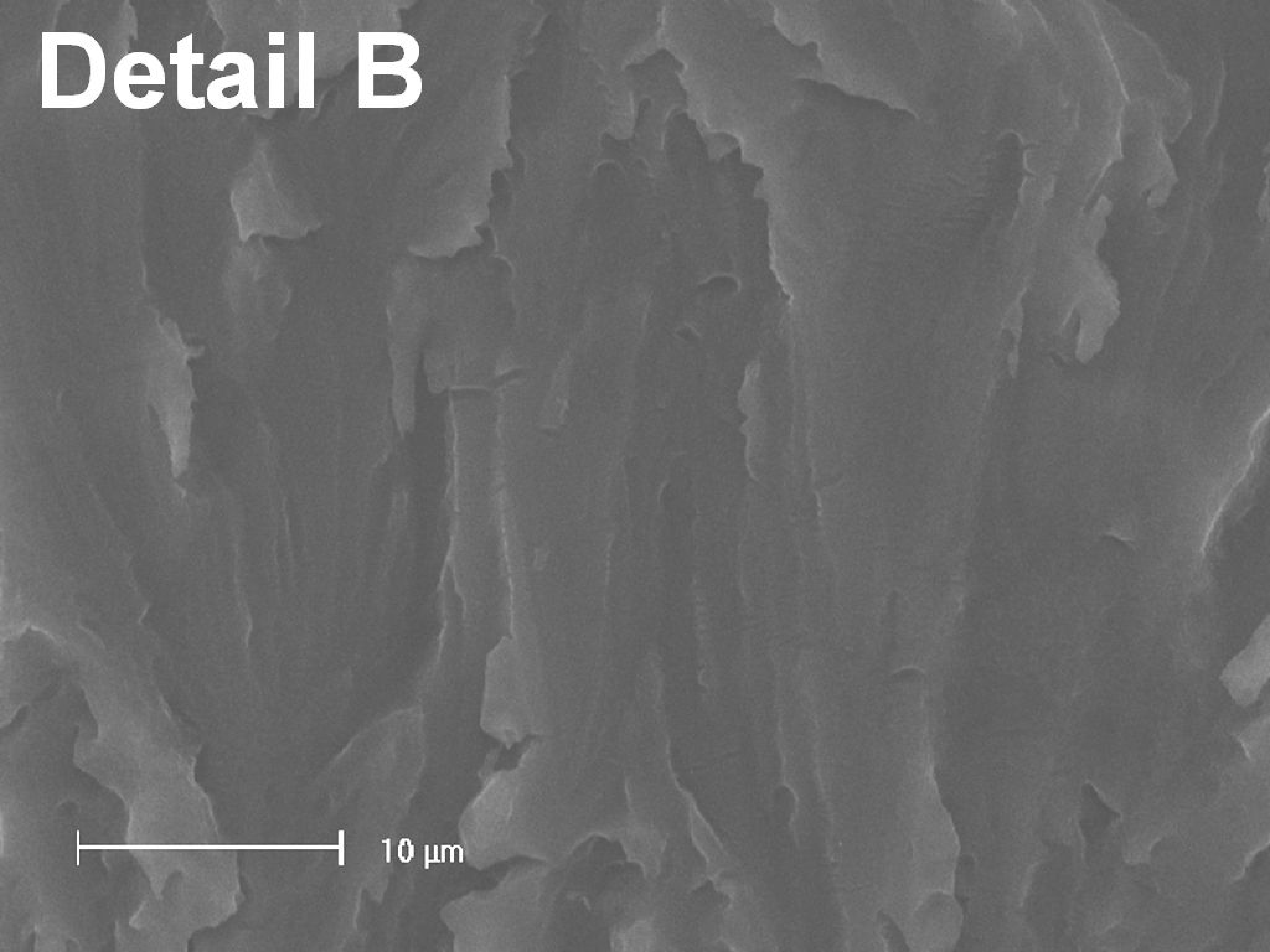
Detail B
10 µm

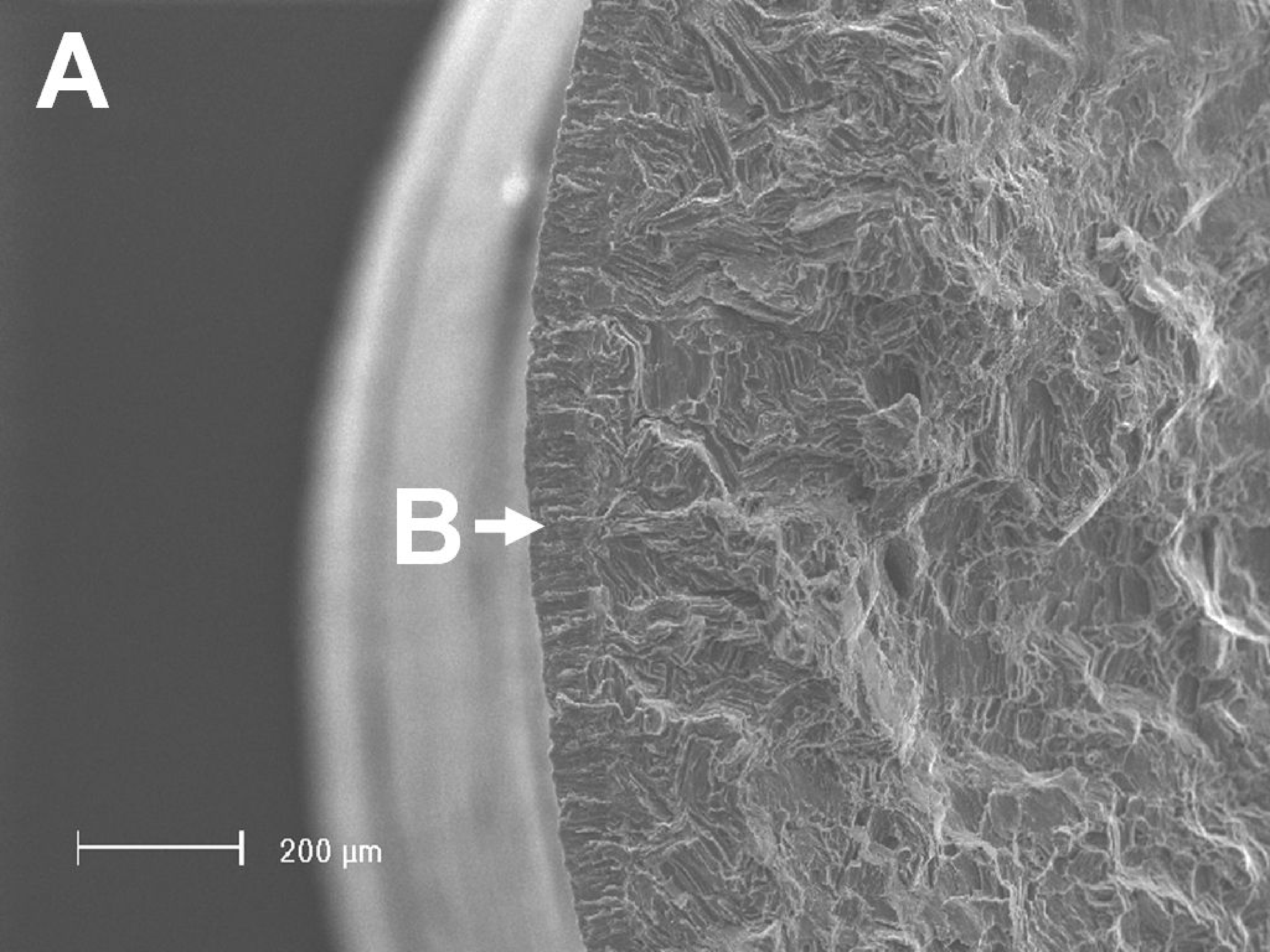
A
B
200 µm

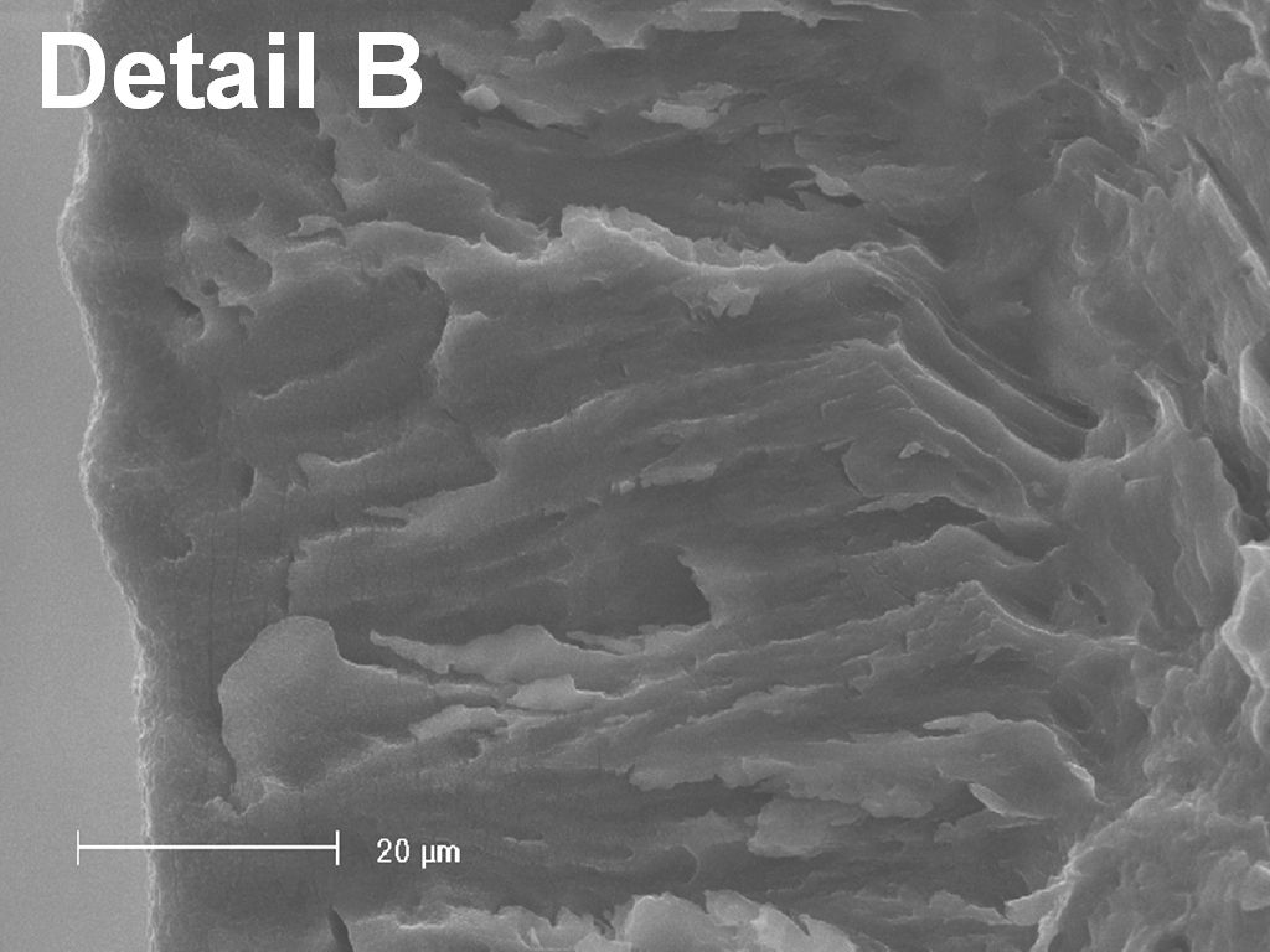
Detail B
20 µm

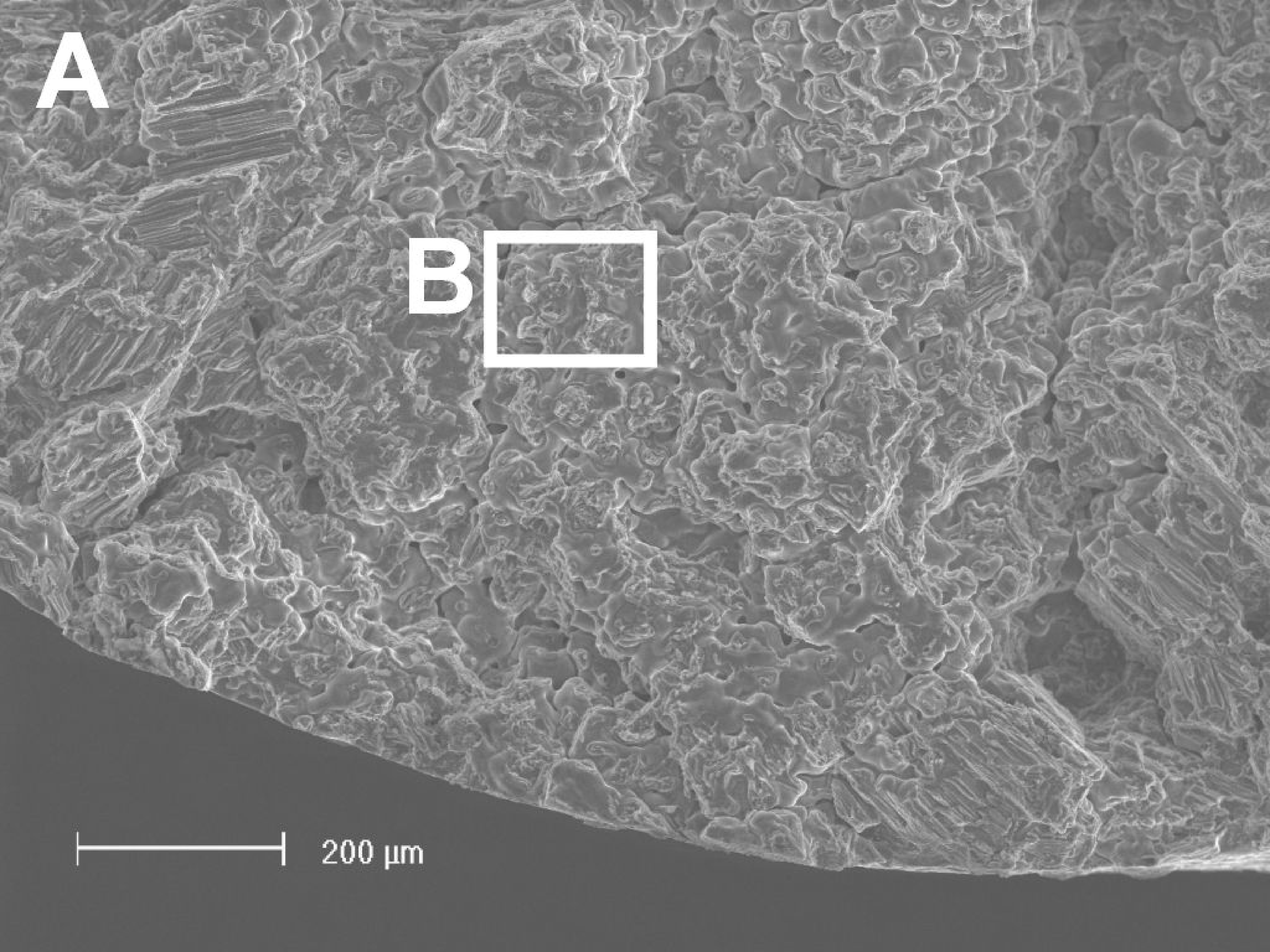
A
B
200 µm

Detail B

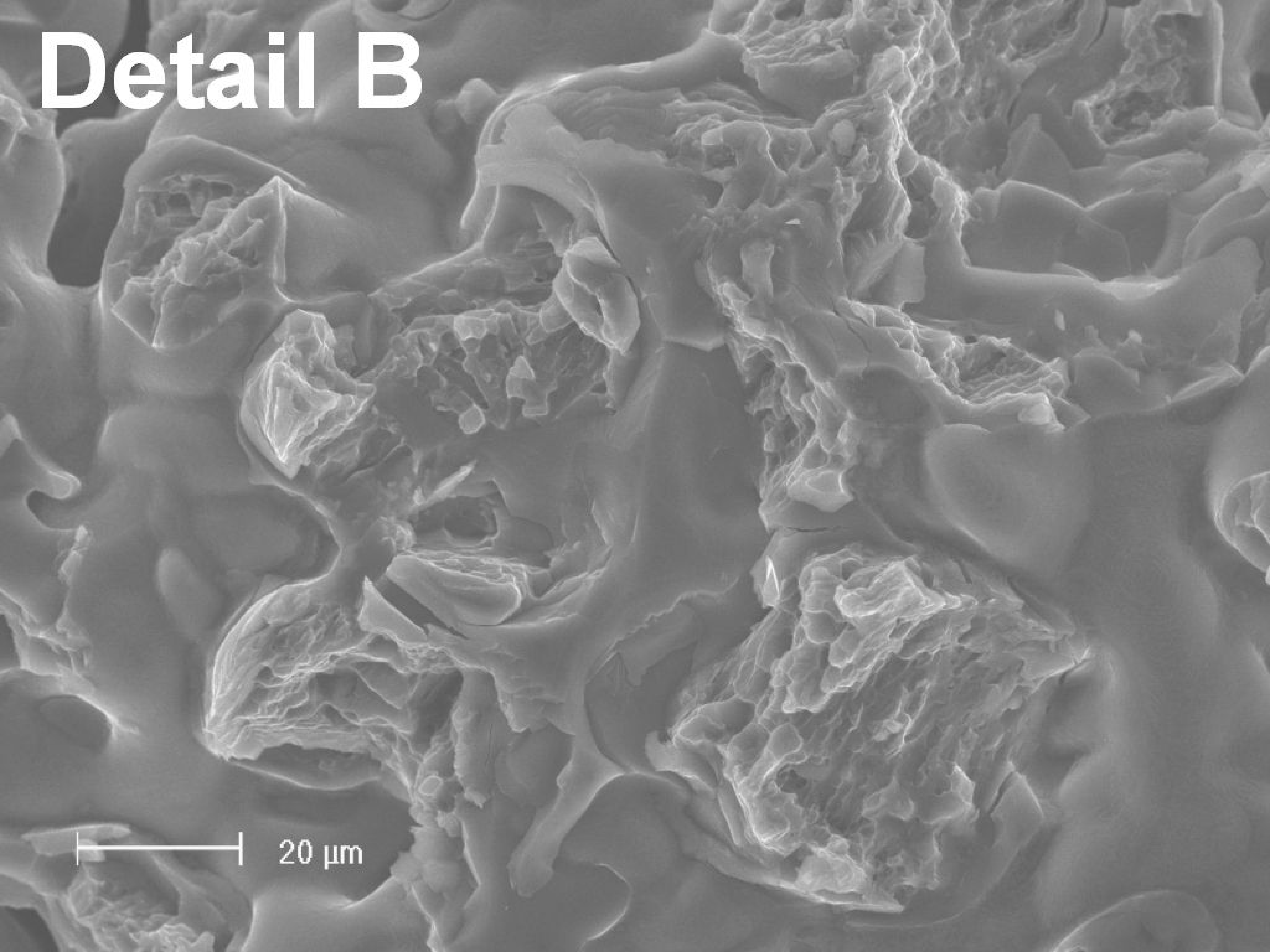

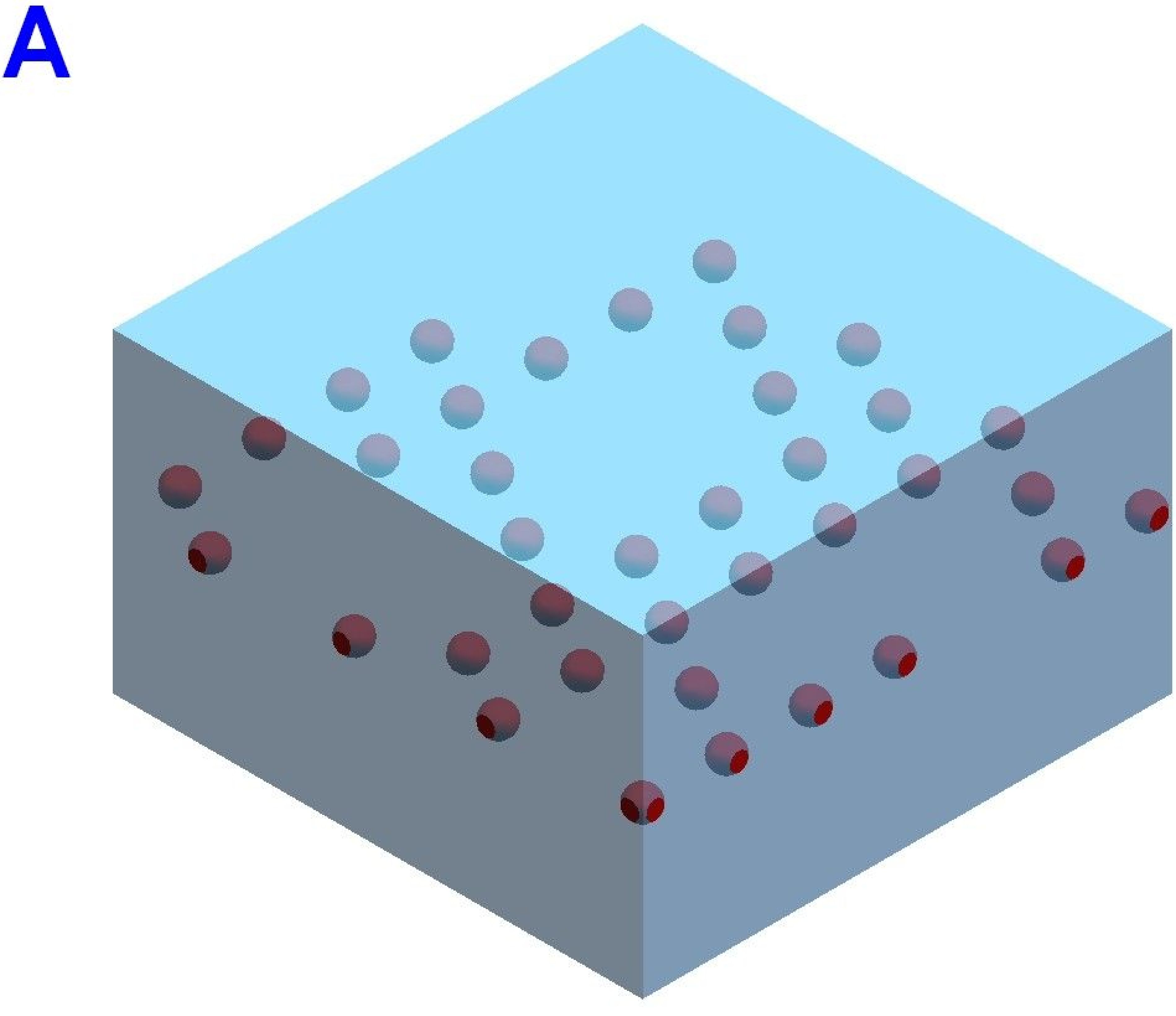
A

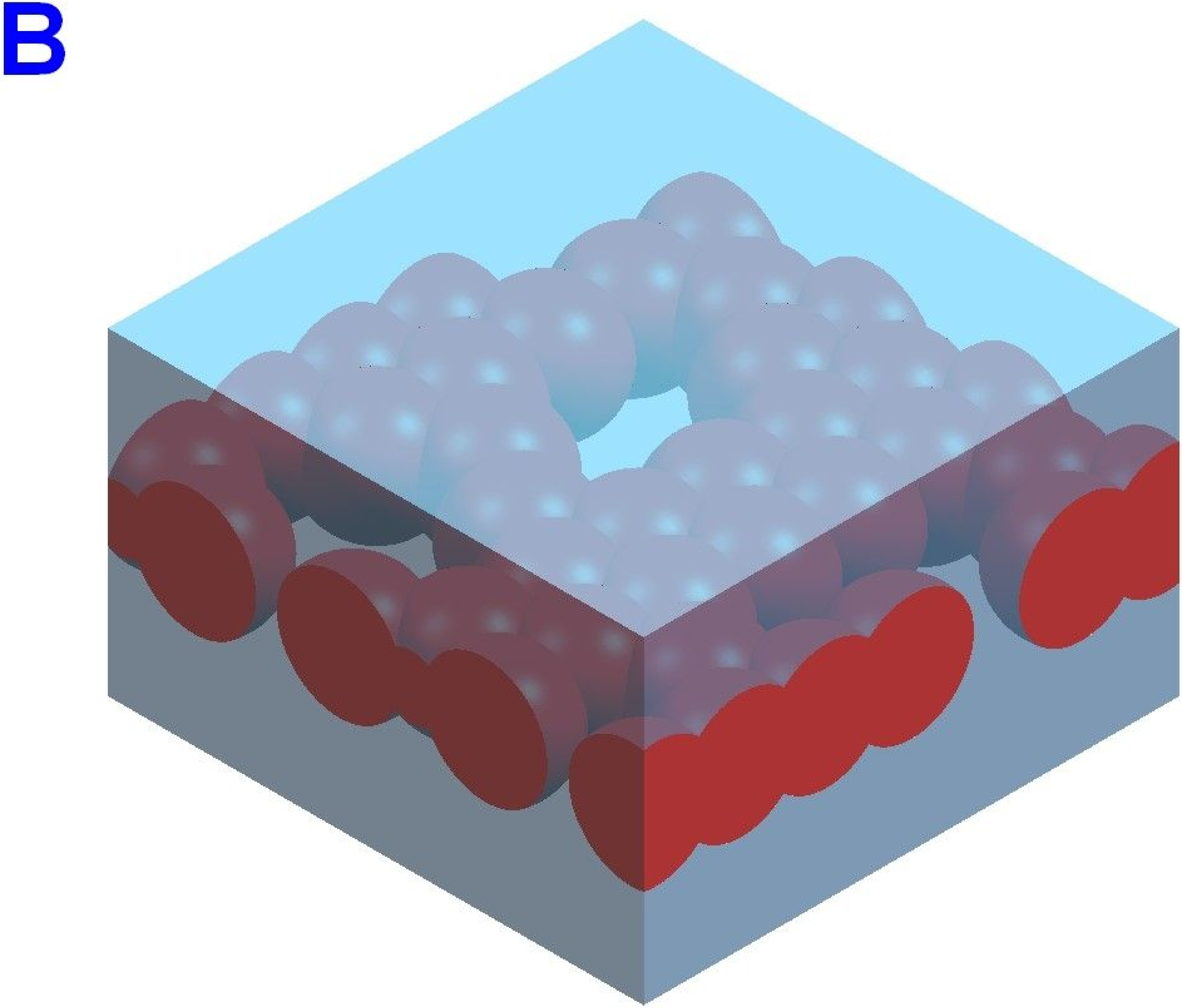
B

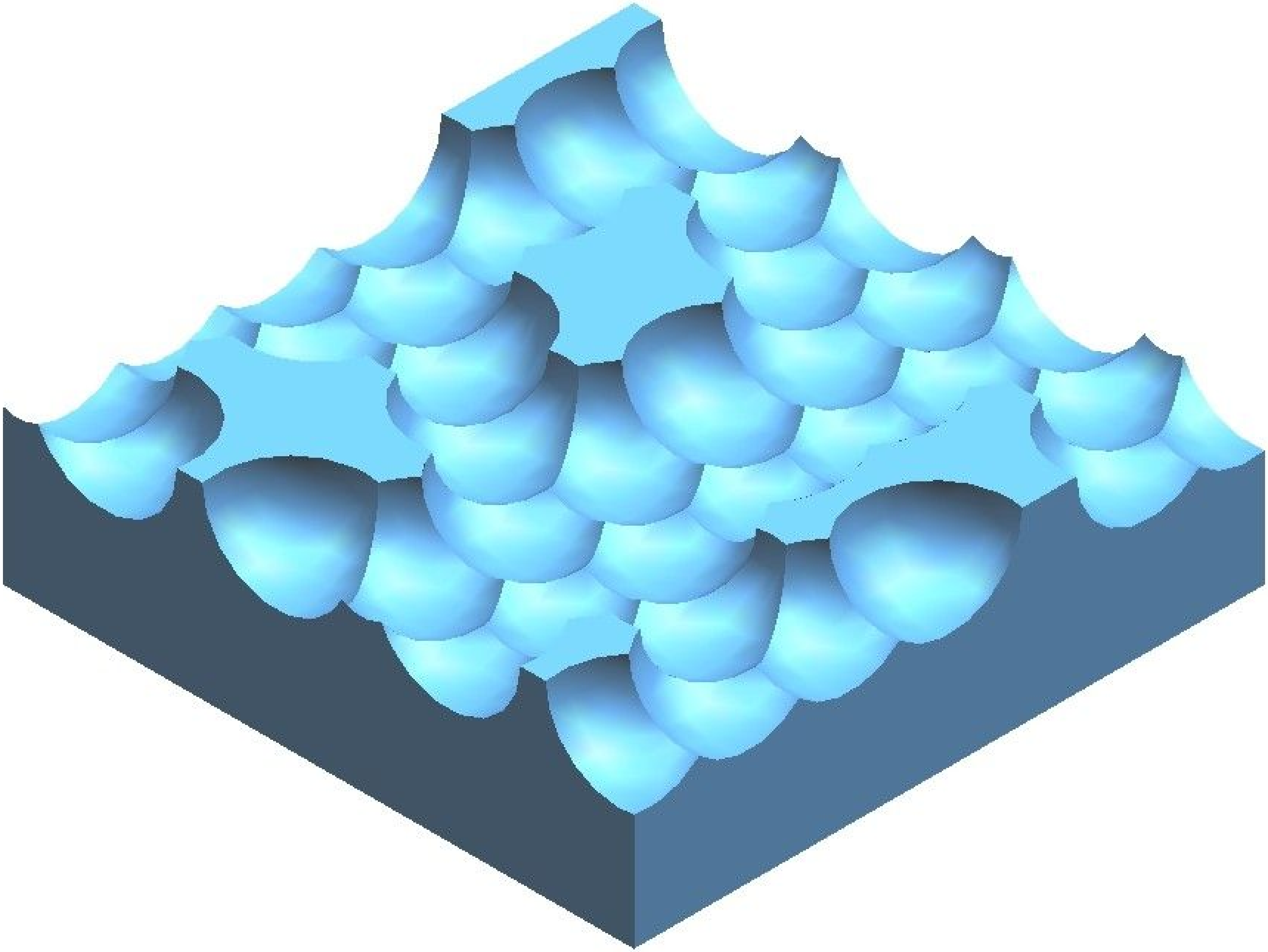C